

2001

Intelligent assist device

Kok-Leong Tan
Iowa State University

Follow this and additional works at: <https://lib.dr.iastate.edu/rtd>

 Part of the [Mechanical Engineering Commons](#)

Recommended Citation

Tan, Kok-Leong, "Intelligent assist device " (2001). *Retrospective Theses and Dissertations*. 678.
<https://lib.dr.iastate.edu/rtd/678>

This Dissertation is brought to you for free and open access by the Iowa State University Capstones, Theses and Dissertations at Iowa State University Digital Repository. It has been accepted for inclusion in Retrospective Theses and Dissertations by an authorized administrator of Iowa State University Digital Repository. For more information, please contact digirep@iastate.edu.

INFORMATION TO USERS

This manuscript has been reproduced from the microfilm master. UMI films the text directly from the original or copy submitted. Thus, some thesis and dissertation copies are in typewriter face, while others may be from any type of computer printer.

The quality of this reproduction is dependent upon the quality of the copy submitted. Broken or indistinct print, colored or poor quality illustrations and photographs, print bleedthrough, substandard margins, and improper alignment can adversely affect reproduction.

In the unlikely event that the author did not send UMI a complete manuscript and there are missing pages, these will be noted. Also, if unauthorized copyright material had to be removed, a note will indicate the deletion.

Oversize materials (e.g., maps, drawings, charts) are reproduced by sectioning the original, beginning at the upper left-hand corner and continuing from left to right in equal sections with small overlaps.

Photographs included in the original manuscript have been reproduced xerographically in this copy. Higher quality 6" x 9" black and white photographic prints are available for any photographs or illustrations appearing in this copy for an additional charge. Contact UMI directly to order.

ProQuest Information and Learning
300 North Zeeb Road, Ann Arbor, MI 48106-1346 USA
800-521-0600

UMI[®]

Intelligent assist device

By

Kok-Leong Tan

**A dissertation submitted to the graduate faculty
in partial fulfillment of the requirements for the degree of**

DOCTOR OF PHILOSOPHY

Major: Mechanical Engineering

**Program of Study Committee:
Greg R. Luecke, Major Professor
J. Adin Mann, III
Robert Gregorac
James E. Bernard
Donald R. Flugrad**

Iowa State University

Ames, Iowa

2001

Copyright © Kok-Leong Tan, 2001. All rights reserved.

UMI Number: 3034225

Copyright 2001 by
Tan, Kok-Leong

All rights reserved.

UMI[®]

UMI Microform 3034225

Copyright 2002 by ProQuest Information and Learning Company.
All rights reserved. This microform edition is protected against
unauthorized copying under Title 17, United States Code.

ProQuest Information and Learning Company
300 North Zeeb Road
P.O. Box 1346
Ann Arbor, MI 48106-1346

**Graduate College
Iowa State University**

**This is to certify that the Doctoral dissertation of
Kok-Leong Tan
has met the dissertation requirements of Iowa State University**

Signature was redacted for privacy.

Committee Member

Signature was redacted for privacy.

Major Professor

Signature was redacted for privacy.

For the Major Program

Signature was redacted for privacy.

For the Graduate College

TABLE OF CONTENTS

LIST OF FIGURES	v
LIST OF TABLES	ix
ACKNOWLEDGEMENTS.....	x
CHAPTER 1 INTRODUCTION AND LITERATURE REVIEW	1
Introduction.....	1
Hardware.....	5
Literature Review.....	9
CHAPTER 2 DYNAMIC MODELING	22
Solid Modeling & Assembly	22
Kinematics	23
Dynamic Formulation of the SAM	29
Lagrange's Equations	31
Mass Moment of Inertia.....	31
Constraint Equation	37
Mapping from Joint Space to Actuator Space	40
Amplifier + Servomotor Dynamics Modeling.....	44
Controller Design.....	50
Experimental Results	55
External Inertia and Damping Effects.....	57
Structural Flexibility	61
CHAPTER 3 CONTROL APPROACH	66
State Controller	66
Repulsive Field for Collision Avoidance.....	69
Interaction of the Human Applied Force with the Repulsive Force Field.....	71
Stability Proof of Repulsive Force Field Implemented by a PD Controller	72
Stability Proof of Repulsive Field Implemented by a Lead Controller	74

Implementation of Repulsive Wall: PD Controller	77
Experimental Result: Repulsive Wall with PD Controller	80
Implementation of Repulsive Wall: Lead Controller.....	84
Experimental Result.....	86
Attractive Force Field Formulation	89
Stability Analysis of Attractive Force Field: PD Controller.....	90
Simulation Results	94
CHAPTER 4 EXPERIMENTAL RESULTS.....	97
Experimental Result I	97
Experimental Result II	105
Experimental Result III.....	109
Experimental Result IV.....	111
Experimental Result V.....	119
CHAPTER 5 CONCLUSIONS AND FUTURE WORK.....	123
REFERENCES.....	125

LIST OF FIGURES

Figure 1.1: A simple air manipulator.	6
Figure 1.2: A pneumatic actuator.	6
Figure 1.3: Base joint.	7
Figure 1.4: Elbow joint.....	7
Figure 1.5: Wrist joint.	8
Figure 1.6: Handle and force transducers.....	8
Figure 2.1: Assembly view of the SAM.....	24
Figure 2.2: Schematic diagram of the SAM.....	24
Figure 2.3: Standard robotic representation of the SAM.	25
Figure 2.4: Coordinate frames assignment for the SAM.	26
Figure 2.5: Comparison of kinematics and dynamics.	30
Figure 2.6: Dynamic representation of the SAM.	30
Figure 2.7: Mass moment of inertia of Link 1.	32
Figure 2.8: Constrained end effector motion.	38
Figure 2.9: Moment of inertia of the base joint for different payloads.....	43
Figure 2.10: Effective mass on the linear actuator for different payloads.	43
Figure 2.11: PWM voltage output [42].....	46
Figure 2.12: Circuit diagram of current mode. [43].....	46
Figure 2.13: Equivalent block diagram of a PWM amplifier in current mode.	46
Figure 2.14: Experiment for identifying amplifier dynamics.	47
Figure 2.15: Velocity response of an amplifier-servomotor system to a step voltage command.	48

Figure 2.16: Simplified servomotor + amplifier system block diagram.	49
Figure 2.17: Amplifier gains of base, linear and wrist joints.	49
Figure 2.18: Controller design for a double pole system.	50
Figure 2.19: Comparison of FRF of a PD and a lead controller.	53
Figure 2.20: A lead controller design.	53
Figure 2.21: Representation of a lead controller in continuous and discrete time domain.	54
Figure 2.22: Pole zero location of a lead controller.	55
Figure 2.23: Close loop system with a lead controller.	56
Figure 2.24: Simulation and experimental result of a amplifier-servomotor system response to a step command.	56
Figure 2.25: Dynamics of a servomotor and an external system.	58
Figure 2.26: System with external damping and inertia.	58
Figure 2.27: Effect of external damping on the system root locus.	59
Figure 2.28: Inertia and damping effects on the system root locus.	59
Figure 2.29: Inertia effects on the control gain.	61
Figure 2.30: A restrained SDOF system.	63
Figure 2.31: Base joint model with structural flexibility.	64
Figure 2.32: Root locus of base joint with structural flexibility.	65
Figure 2.33: Base joint dynamics and controller.	65
Figure 3.1: A PD controller for implementing repulsive force field.	73
Figure 3.2: Lead controller for implementing repulsive field.	75
Figure 3.3: Linearized repulsive force field dynamic model.	76
Figure 3.4: Comparison of classical and modified repulsive force field.	80
Figure 3.5: Experimental setup.	81
Figure 3.6: System natural frequency & damping ratio.	82

Figure 3.7: System response to the original & modified repulsive wall formulations.....	83
Figure 3.8: System response to different user-applied torques.	84
Figure 3.9: Roots of CE.....	85
Figure 3.10: Magnitude of complex solutions	86
Figure 3.11: Original repulsive wall formulation: lead controller	87
Figure 3.12: Modified repulsive wall: lead controller.....	88
Figure 3.13: Comparison of the original and modified repulsive wall formulation	88
Figure 3.14: A typical attractive force field.	89
Figure 3.15: Damping coefficient.	92
Figure 3.16: Spring force and damping force of an attractive force field.....	92
Figure 3.17: Effect of attractive well on the velocity response.....	93
Figure 3.18: System response to an attractive well when $\theta=-2.0$, $\dot{\theta} =1.0$	95
Figure 3.19: System response when the initial velocity is large	96
Figure 4.1: Home configuration of the SAM	99
Figure 4.2: User-applied force and actuation force in X direction.....	99
Figure 4.3: User-applied force and actuation force in Y direction.....	101
Figure 4.4: User-applied moment and actuation moment	101
Figure 4.5: User-applied force and system response in Y direction.	102
Figure 4.6: Machine with a 100 lbm payload.....	103
Figure 4.7: User applied force and actuation force in X direction with a 100 lb payload. ...	104
Figure 4.8: User applied force and actuation force in Y direction with a 100 lb payload. ...	104
Figure 4.9: User-applied force & actuation force	106
Figure 4.10: User-applied force & end effector position in Y.	107
Figure 4.11: User-applied force & actuation force when the handle was at 90 degree.	108

Figure 4.12: User-applied force & end effector position in Y direction.....	109
Figure 4.13: A simple repulsive wall.	110
Figure 4.14: A simple repulsive wall at 90°.....	111
Figure 4.15: A composite repulsive wall.	113
Figure 4.16: Modeling of a sharp corner.....	113
Figure 4.17: A circular segment corner.....	114
Figure 4.18: End effector trajectory.	115
Figure 4.19: Actuation force & repulsive force on the payload.....	116
Figure 4.20: End effector trajectory of payload.	118
Figure 4.21: Forward path motion of payload.....	118
Figure 4.22: Actuation force, repulsive force and user-applied force.....	119
Figure 4.23: Cancellation of repulsive forces from different walls	120
Figure 4.24: Attractive moment	122
Figure 4.25: Attractive moment when the payload was inside the tunnel.	122

LIST OF TABLES

Table 2.1: Physical properties of the SAM	23
Table 2.2: DH parameters describing the SAM	26
Table 3.1: Routh Table for TF	77
Table 3.2: Servomotor and amplifier properties	81

ACKNOWLEDGEMENTS

My greatest appreciation goes to my advisor Dr. G. R. Luecke for his guidance in this research. I would also like to thank Dr. Bernard, Dr. Flugrad, Dr. Adin Mann, and Dr. Gregorac for being my POS committee members. I would like to express my gratitude to all of my friends and family members for their encouragement throughout these years. Dr. Wei Wu, Tock Gee, Yong & Lee, Ming Fen, Kok Hong & his family, Sony, Yongjun, Siew Kim & her loving sons, you all play an important part of my life and deserve more than a thank you. Finally, I would like to thank my dad and mom, Mr. Tan Chin Hwa and Mrs. Lee Khim Eng for their endless loves since I was born.

This work was performed at Ames Laboratory under Contract No. W-7405-Eng-82 with the U.S. Department of Energy. The United States government has assigned the DOE Reprot number IS-T 2216 to this thesis.

CHAPTER 1 INTRODUCTION & LITERATURE REVIEW

In this research we present the overall strategy for the actuation and control of an intelligent assist device (IAD). An IAD is a hybrid manipulator that integrates the strength of a machine and the intelligence of a human being to optimize its performance. In this implementation, the human operator using an IAD is assisted by the power of the servo drives as well as intelligence from the IAD itself to avoid collision with the environment by an artificial repulsive force field. An attractive well is also constructed to modify and steer the trajectory of the end effector.

Introduction

The material handling operation is an important process in a modern manufacturing environment. This operation is traditionally done by an operator with the help of mechanical assist devices such a conveyor belt, an overhead hoist or a trolley. One common feature of these devices is that they support the weight of the work piece, relieving the operator of the need to exert energy for lifting. However, the operator still needs to use his or her physical strength to move the work piece to a desired destination. The inertia forces generated by heavy payloads and the mechanical parts of the lift-assist device may still be large enough to pose a danger to the operator. According to a survey by the Bureau of Labor Statistics, U.S. Department of Labor [1], a total of 5.7 million injuries and illnesses were reported in private industry workplaces during 1999. Among goods-producing industries, manufacturing had

the highest incident rate. There were about 372,000 newly reported cases of occupational illnesses in private industry in 1999. Manufacturing accounted for three-fifths of these cases. Disorders associated with repeated trauma made up 66 percent of the 372,000 total illness cases. Seventy percent of the repeated trauma cases were in manufacturing industries due to overexertion and repetitive motion. The total cost to the industries of these injuries and illnesses was significant. An IAD was created to answer these pressing workplace ergonomic concerns in manufacturing industries.

On a production floor, operations such as material handling or assembling process can be handled by three different fashions. They are manual, fully automated and hybrid automated operations. Manual operation is the most flexible among all of them, and it is most suitable for a complex, non-repeated, low volume process. The major drawback of a manual operation is its inability to handle operation with many repetitive motions and with heavy objects involved since this operation simply relies on the physical strength of human being. The performance of a manual operation might degrade simply due to the physical tiredness and mental fatigue of the worker. A fully automated operation, on the hand, handles task that requires many repetitive motions and with heavy objects involved well. However, a fully automated operation is not comparable to a manual operation in term of its adaptability to changes. Therefore, a fully automated operation is only suitable for a high volume production. In certain assembly, numerous operations have resisted automation because the manual dexterity and adaptability of the human cannot be replaced. For instance, in a furniture-manufacturing cell, the operator has to move a wooden tabletop from a cart to a CNC machining center for deburring. Once the deburring process is completed, the operator has to move the work piece to another cart waiting to be transported to the next processing

cell. The locations of the carts carrying the work pieces may not be at the same location every times and therefore it poses a challenge to a fully automated robotic manipulator. This leads to the development of hybrid automation. Hybrid automation fits in between a manual and a fully automated operation. Hybrid automation takes advantages of the powered actuation strength from a fully automated operation and the intelligence of an operator from a manual operation. IAD is considered as a kind of hybrid automated manipulator. An IAD can be further divided into two categories. The first type of IAD provides force amplification to the human operator [2] and the second type purely enforces constraint to avoid collision using actuators [3].

Although the use of servo actuation for control of an IAD is similar to an industrial robot, there are several major differences between a conventional robotic manipulator and an IAD. First, the trajectory of an industrial robotic manipulator is programmed in advance and it does not need the presence of a human operator during execution. On the other hand, the human operator and the machine share the common workspace and determine the final course in an IAD. Second, an industrial robotic manipulator needs to work in a well-defined environment. The position, orientation, weight of the work piece, obstacles in the workspace, coordination with other machines, etc, have to be well understood ahead of time. In comparison, these constrains are not important in IAD, since the human operator continuously guides the trajectory of an IAD. In other words, a human operator remains in complete control of the device at all times. By taking advantage of the path planning capability of the operator, an IAD is more flexible than a conventional robotic manipulator.

An IAD is also different from a remote controlled master-slave type robotic manipulator since the operator has direct and physical interaction with the machine/payload

in shared workspace. However, with all the joints powered by actuators, and the human operator in the working space of the manipulator, safety of the operator is a serious concern when designing the controller for an IAD. In this regard, the stability of the overall system is the single most important requirement for designing the controller. In addition, in the hardware design, the operator can shut down the machine immediately if anything goes wrong. This can be accomplished by an emergency button that has direct control of the power to the servo-amplifiers of the manipulator.

The objectives of this research can be summarized as follows.

(1) Relieving ergonomic concerns of operator using a heavy lift assist device. This is accomplished by controlling motions of the manipulator to minimize the apparent inertia felt by the operator, partially compensating for the damping/friction forces of the system and, amplifying the effort of the operator through the use of power actuators.

(2) Avoiding collision of the manipulator with the environment. This objective is achieved by the use of repulsive force field. However, a modification on the force field formulation is necessary to ensure the system stability.

(3) Simple and intuitive interface. An IAD is designed for the operator. Therefore, it is critical to the success of this research that the operator finds the device simple and easy to use. The design of the interface allows the operator to use the device with a minimum amount of training.

(4) Safety. Putting a human operator inside the workspace of a powered IAD raises concerns about the operator's safety. Stability proof of the overall control system is critical. In addition, several safety features have been built into the machine to protect the operator against unplanned manipulator's motions.

(5) Flexibility of the collision avoidance feature. A composite repulsive wall is able to model a large class of objects. Therefore, it provides a convenient way to build a repulsive wall around the obstacles.

(6) Provide guidance to the user. By using attractive well, the machine trajectory will be modified to move in a preferred path. This feature helps to reduce the amount of training required for a new user.

Hardware

Figure 1.1 shows the heavy lift assist device used in this work for the design and development of the intelligent assist device. The machine is called “Simple Air Manipulator” (SAM). In the original configuration, the machine was powered only in the vertical direction by a pneumatic actuator, as shown in Figure 1.2. The pneumatic actuator and the counter weights were used to compensate for the gravity effect. To reduce the physical labor required of the operator when using the device, we actuated the base (Figure 1.3), elbow (Figure 1.4) and wrist (Figure 1.5) degrees of freedom with DC servomotors. Closed loop control was implemented to position the end effector. The servomotors were controlled by a multi-axis motion-control board (Servo_to_go) in a PC. The base, vertical and elbow joint were primarily responsible for the end effector position, whereas the wrist joint was used for the orientation adjustment of the work piece.

Force transducers were used to provide the ease of interfacing between the human operator and the machine. As shown in Figure 1.6, two force transducers were mounted on the handle of the machine. The force transducers served two purposes. First, they were used

to sense the force inputs from the operator. Second, they were used for transmitting the forces and the moment from the handle to the machine. It will be demonstrated by the experimental results in Chapter 4 that the human operator contributes a significant portion of motive forces/moments to drive the system.

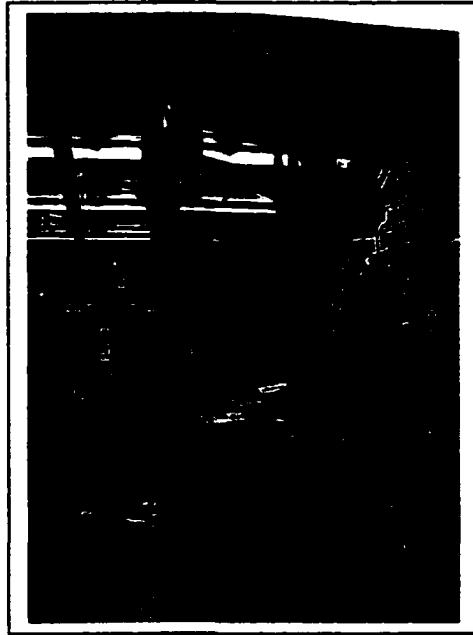


Figure 1.1: A simple air manipulator.

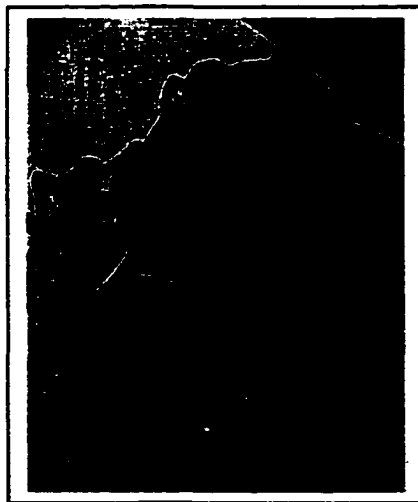


Figure 1.2: A pneumatic actuator.

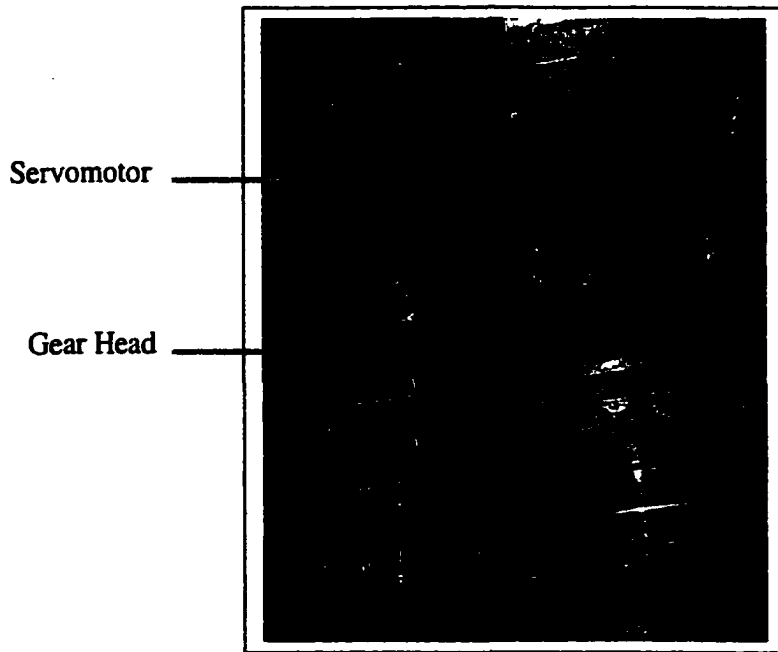


Figure 1.3: Base joint.

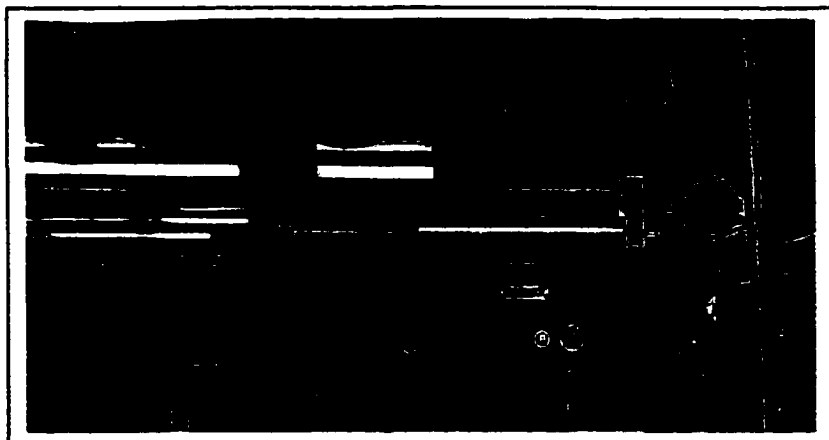


Figure 1.4: Elbow joint.

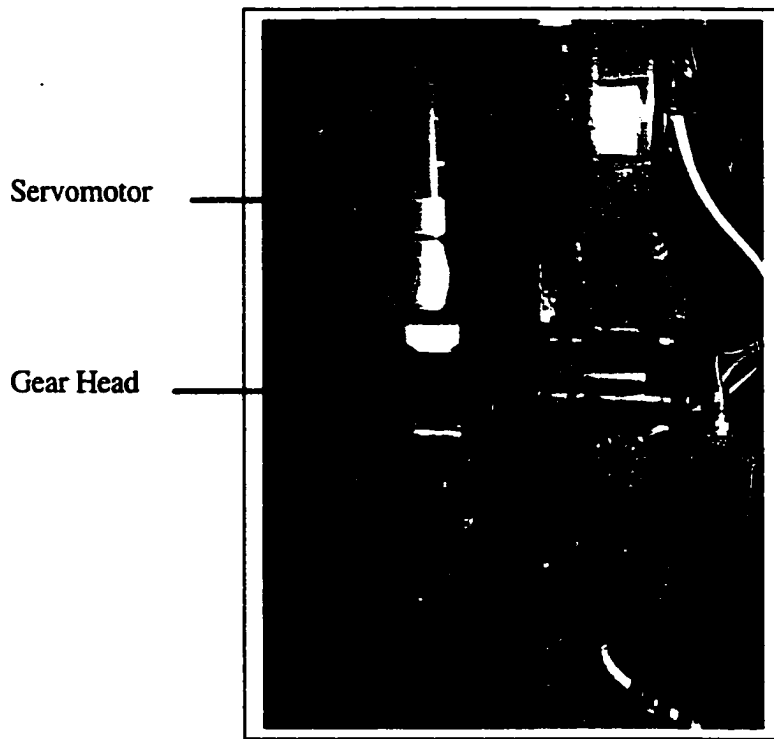


Figure 1.5: Wrist joint.

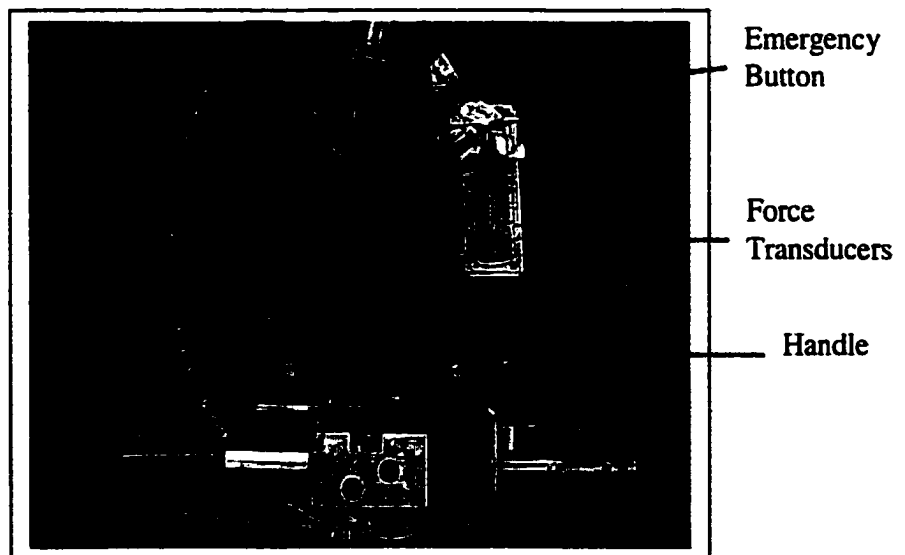


Figure 1.6: Handle and force transducers.

Literature Review

A device that would augment the lifting and carrying capabilities of a human being was built by the Department of Defense in the early 1960. The original goal was to design a master-slave system that would allow the human and the robotic manipulator to become an integrated system that used intelligence from the human being and the enormous lifting capabilities of the robotic manipulator. A later study showed that it was not feasible to duplicate all the degrees of freedom of a human being, because the final system would be extremely complex, and it would pose a tremendous challenge for the control and mechanical system design. A further work showed that a robotic manipulator with fewer degrees of freedom could accomplish most of the desired jobs. The development in this area diverged into two distinct directions. One followed the traditional concept of remote controlled robotic system, whereas the other eliminated the control device and integrated the human being into the robotic system.

A traditional remote controlled robotic manipulator consists of a control device and a slave robot. The control device is responsible for interpreting the intention of the operator and sending out the corresponding motion commands to the slave robot. A control device can be as simple as a potential meter or a joystick. On the other hand, a slave robot is solely responsible for carrying out the commands from the control device. Normally, a control device doesn't receive any feedback from the slave robot. The human operator, with his visual sense, judgement and experiences, closes the feedback loop for the entire control system. The performance of the manipulator heavily depends on the skills and familiarity of the operator.

In a traditional master/slave robot, the operator doesn't have any knowledge on the inertia of the work piece and the dynamic forces that the slave robot is experiencing since there is only visual feedback available to him. Recently, there has been progress on simulating the dynamic forces experienced by the robotic manipulator in a haptic display device. It is now possible for the operator to experience the downscaled version of dynamic forces that a slave robot encountered in a control device provided the control device is equipped with the necessary actuation. Chai [4] used the exoskeleton at Iowa State University and an industrial robot to simulate the dynamic forces of touching a virtual stiff wall, pressing a virtual push button and playing a virtual yo-yo. Edwards [5] used a Puma 560 as a haptic interface to virtual environments.

Even with the capability of simulating the dynamic forces in a control device, the operator using a remote controlled robotic manipulator still needs to rely on some visual aid, such as a TV camera for the positioning of the work piece when he is operating at a distance. Consequently, the accuracy and speed of the operation may be limited by the responsiveness of the camera because it has to focus on the work piece constantly. Keep in mind that the primary reason for using a remote controlled robot rather than a conventional fully automated robotic manipulator is the flexibility that the former can offer. Most of the times the operator has to make his judgement for the motion of the robot solely based on a 2D TV screen image. This might pose a challenge to the operator since the 2D TV screen does not offer the sense of depth.

A more accurate placement of the work piece and a faster operation are the critical factors affecting the productivity on a production floor. It is crucial for the operator to be adjacent to the end effector of the manipulator so that he can monitor the operation closely.

There are several advantages for putting a human operator in the workspace of the robotic manipulator. First, the human operator has physical contact with the robotic manipulator. Because of the direct and physical interaction with the robotic manipulator/work piece, the operator has a better feeling on the system inertia characteristics. For instance, when using a trolley, which is an un-powered manipulator, the operator needs to maneuver it with his strength. He will naturally push harder when moving up a ramp. This is because the gravity force is acting against him. He needs to increase his applied force in order to maintain the motion. The second advantage is that the operator can monitor the lifting, material handling and assembling operation more closely, and therefore a greater accuracy in the placement of the work piece and a faster operation of transporting the work piece can be expected. Finally, there is no need for a separate control device and visual aid for the operator. This leads to the development of the second type of robotic manipulator. The representative researches done on this field are the "Human Extender" at UC Berkeley and the "Cobot" at Northwestern University.

"Human Extender" was coined by Kazerooni and Guo [2] for a device that augmented human mechanical strength, while the operator's intellect remained the central control system for the device. In the human extender, the operator exchanged signal and power with the manipulator. In combination, the forces applied by the human operator and the actuation forces generated the final trajectory of the manipulator. In the controller design for the human extender, the actuator carried the major portion of the workload, whereas the human operator took up the remaining part.

Normally, dynamic interaction between the robot and its environment was neglected (except for interaction with a very stiff environment) and a model of the robot alone was

sufficient for control system design. Putting a human operator into the control loop was more difficult than designing a conventional robotic controller because there were two distinct systems which interact, the human operator and the robot. One of the systems, the human operator, was extremely complex and very difficult to characterize. The stiffness of a human arm could increase significantly by “tensing” the arm muscles – simultaneously activating opposing muscles about the joints. The net moment about a joint was a weighted difference of muscle tensions, and the net stiffness about the joint was a weighted sum of the contributions from each of the muscles [6]. Because of this, by carefully coordinating muscle activities, the net joint moment could be held constant while the net stiffness increased/decreased. Lanman [7] reported that the stiffness of a human elbow joint ranged from a minimum of 2 N-m/rad to 400 N-m/rad. Hayes and Hatze [8], Cannon and Zahalak [9] had similar findings. These results depicted that the stiffness about the elbow joint could vary over a wide range. Hogan [10] found that the effective damping ratio of the human arm was about 0.13, a rather lightly damped system. Because of the wide stiffness range of a human arm, the human operator could either be a stabilizing or destabilizing factor in the entire control system. By incorporating his own damping and low stiffness into the system, he could increase the stability margin of a system. However, he could also destabilize the system by reflecting the force back into the system by tensing his muscles. In a human-robot control system, kinetic energy must be exchanged between the human arm and the robot, therefore knowledge of human arm dynamics is required to predict the closed loop stability of the system. However, identifying human dynamics is extremely difficult since it can be changed voluntarily [6]. Besides, many other factors influence the behavior of human arm dynamics. Some of them are the viscoelastic properties of the joint surface, ligaments,

connective tissue [11], muscle mechanics, reflex effects, the relationship between joint position and muscle length, and the list goes on. Kearney and Hunter [12] summarized the models that had been used to describe the human dynamics. The models can be as qualitative as representing the human arm conceptually as a spring connected to a rack-and-pinion mechanism [13]. Of course, this conceptual model is only capable of capturing the characteristics of system behavior qualitatively, but cannot make quantitative predictions. Empirical models [11] that provided quantitative descriptions of system behavior for a particular set of conditions could be considered as a progress from the conceptual model. This model suffered the drawback that it could not in general be used to predict behavior other than the prescribed set. Finally, mathematical or analytical models had been used to describe the behavior. Mathematical models provide the most information about a system, and they are the most difficult to obtain. Linear system-identification methods had been used extensively to characterize the dynamics of ankle [14], wrist [15], elbow [16] and jaw [17]. A common finding had been that linear models provided excellent descriptions of joint dynamics if conditions such as the activation position and posture were maintained approximately constant throughout the experiment. Kearney and Hunter [12] concluded that joint dynamics could be modeled using a parametric model of the form:

where $T(t)$ is the external torque acting on the joint, I is the effective inertia parameter, B is the viscous parameter and K is the elastic parameter of the joint.

This model would predict result well only if the operating point, which was defined by the perturbation amplitude and the mean position, to be close to the original. Lacquantti

[16] found that the stiffness of a forearm was 13.8 N-m/rad when the testing subject was told not to resist the excitation motion. The stiffness could go as high as 62.1 N-m/rad when he was told to resist the excitation motion maximally. From the experiment, the natural frequency and damping ratio of the forearm was found to be 8.0 rad/sec (1.2 Hz), 0.338 in the “do not resist” case, and 17.3 rad/sec (2.7 Hz), 0.218 in the “maximally resist” case. In this research, it was observed that the system would be less stable if the operator was holding the handle with stiffened arms.

In the human extender, the human arm and hand were explicitly modeled as a passive second-order system. The reader should be aware that a human arm is fundamentally different from a second order system since the former is an active system and the later is a passive system. The net energy that a passive second-order system can deliver to its environment can not be greater than the energy it stores. However, a human arm is fully capable of supplying energy to its environment and initiating a motion. Therefore it is important to realize that a second order system can only approximate the true dynamics of a human arm and hand.

On the other hand, “Cobot”, a robot for collaboration with human operators, was investigated by Colgate and Wannasuphprasit [3] [18] [19] at Northwestern University. To manipulate a work piece, the cobot and the human operator determined its final motion. The human operator produced the motion of the cobot and the work piece by applying motive forces and moments. The cobot guided a human operator to move in a useful direction by setting up virtual surface that constrained the overall motions. For instance, a cobot could guide a surgeon to perform a surgery or an operator to assemble a door of an automobile. However, to ensure stability, a cobot could only provide energy to the actuator that was used

to enforce the kinematical constraint. In other word, the cobot was energetically passive. Recently, a cobot with powered actuation [20] has been developed. The safety of the power assisted cobot is preserved by using small size motors.

The stability associated with this research is another field of study by itself called “force control” or “contact instability”. Force control is a crucial step in enabling robots to perform certain tasks that are not possible with position control scheme, such as milling, drilling, and tightening a bolt, which requires significant interaction with the environment.

Eppinger and Seering [21] [22] [23] explained the often-observed instability of a force-controlled robot contacting a stiff surface was due to the non-colocation of sensors and actuators. The instability induced by the non-colocation of sensors/actuators was first noticed in the control of flexible structure [24]. The dynamic elements separating sensors/actuators introduced several problems. First, there were more degrees of freedom in the system than the sensors/actuators. Second, the states observed by the sensors were different from the states where the actuators were located. Finally, the signal, either the force or position, at the locations of the sensors had a phase shift from the control command. Therefore, it was the dynamic elements separating the sensors and actuators that had the most impact on the system stability. Whitney [25] modeled the environment as a spring with stiffness K . For a fixed controlling frequency, the feedback gain was inversely proportional to the environmental stiffness in order to maintain system stability. In other words, high bandwidth force control required a compliant sensor or environment.

Craig and Raibert [26] [27] suggested a hybrid position/force control scheme, where the force error function would decay according to a second order system behavior with user

specified parameters. However, they assumed that the robotic arm was rigid and this scheme neglected the dynamic elements separating the actuators and sensors.

Colgate and Hogan [28] analyzed contact stability using a passive physical equivalent method. They carried the force control problem a step further to consider the stability issue associated with the non-collocation of actuators/sensors. The major conclusion from [28] was that it would be more fruitful to reconsider the design of the manipulator rather than to design a controller because of the fundamental limitation.

The rigidity assumption in the dynamic modeling of robotic manipulators becomes invalid when they are intended for wide operating range or carrying heavy loads. Tasks involving fast motion or contact with the environment are expected to exhibit oscillatory behaviors, which are evoked by high acceleration forces or external forces. In this research, one of the problems we faced when implementing actuators and the controller for the system was the flexibility of the long reach arm. The oscillatory behavior became prominent when there was a heavy payload at the end effector. From vibration theory, one knows that the system natural frequency is inversely proportional to its inertia. The lowest natural frequency of the system was observed to be about 4 Hz. As the rigidity of the machine deteriorated, which might be due to the loosening of the joint bearings, the natural frequency decreased. There are two principle sources of vibration in a manipulator - joint elasticity and link flexibility. Joint elasticity is caused by the transmission elements such as the driving belts, chains and gears. In both cases, the overall system contains more degrees of freedom than the available actuators. In this research, the link flexibility was the principle source of vibrations at the end-effector.

In the control of flexible robot, there are two types of objective that a control designer is looking for. These are precise positioning and precise execution of trajectory. Strictly speaking, the former objective is easier to accomplish since its primary concern is to position the end-effector at a certain spot in a fixed duration. How well the end-effector tracks the trajectory at any instant in between the execution is immaterial. The latter pays particular attention to the precise tracking of the end-effector to the desired trajectory at every instant. Precise tracking of trajectory has wider applications in practice such as welding and spray painting.

There are a few schemes for controlling a flexible structure to track a desired trajectory. So far the assumed mode, model-based input shaping or feed-forward control scheme [29] is still the most widely recognized method that can achieve satisfactory performance in tracking task. In short, for feed-forward control, the whole motion task should be known in advance so that the required input torque can be computed off line, based on the available dynamic model of the robot. This method works satisfactorily when no perturbations act on the system and the initial state is correctly guessed. Most researchers found that flexible robotic structures can be modeled as Bernoulli-Euler cantilever beams, with the motion command input at the base of the cantilever. Hastings and Book [30] showed that only the lower two or three flexible modes of the cantilever would tend to be excited by the commands. In addition, servomotors act essentially like a low pass filter, which makes the excitation of the higher structure modes unlikely.

A controller for precise positioning is simpler than the tracking problem and it can be designed based on the frequency domain of the command signals. For instance, assuming that the first natural frequency of a flexible structure is ω . The first mode is considered since

it is the most prominent, the easiest to excite and the principle source of motion error. A half sine pulse with a pulse width of T has a notch at $1.5/T$ in the frequency domain. As a side note, a notch in the frequency domain simply implies that the command does not have any energy at that frequency. As long as the pulse width is chosen such that the system natural frequency coincides with the notch frequency, that mode of vibration will not be excited.

Luca [31] surveyed and classified different alternatives for generating the torque commands needed to perform typical motion tasks in flexible robots. He concluded that a global stability analysis for the trajectory tracking capabilities for feedback control law is still missing.

Garcia and Feliu [32] used an implicit force control scheme for a single-link flexible arm end-tip force regulation. The method was called implicit because there was no specific controller for the force and its control was achieved through the knowledge of force/displacement relationship of the robotic arm, i.e., backup the end-tip force by the deflection of the link. In this case, there was no need to have a force sensor mounted at the end-tip. However, the assumption they made for using this controller was that only the first mode of vibration would be excited during the motion.

Another focus of study in this research is to investigate various method of avoiding collision with the environment. Kazerooni and Mahoney [33] [34] addressed the issues of the dynamics, control and stability of human extenders. However, in their research, they didn't touch on the issue of collision avoidance when using these devices. Collision avoidance was traditionally considered as a high level path planning process until mid 1980, when a real time obstacle avoidance scheme using artificial potential field around an object was pioneered by Khatib [35]. The artificial field concept proposed by Khatib became part of

the low level inputs (artificial forces) into the system so that the end effector would move toward a target point under the influence of attractive force field and avoid collision under the repulsive force from an obstacle. By incorporating the potential field forces into the control algorithm, the potential forces become part of the system dynamics. The manipulator moves in a field of forces. The position to be reached is an attractive pole for the end effector and obstacles are repulsive surfaces for the manipulator. In his research, the low level programming capability was fully expended since the operator only needed to focus on the more important issues when controlling a manipulator such as approaching velocity, positioning the work piece and adjusting the orientation of the end effector.

There are three different ways of implementing the artificial potential field for collision avoidance and they are sensor based, model based and sensor/model hybrid scheme. Veelaert and Bogaerts [36] implemented the artificial potential field concept for collision avoidance in a joystick-controlled wheelchair. In their system, a pulse emitter was constantly sending out signal to the surrounding. By processing the signals of the original pulse as well as the echo from the surrounding, obstacles could be identified and the distances could be measured. In their research, both the joystick input from the operator and the artificial potential field from the algorithm determined the final course of the wheelchair.

Wong [37] focused on how to extract 3-D information from a 2-D image of a camera. The edges of obstacle were identified by a curve fitting method, and the overall shape of the obstacle was recognized by hypothesis matching process. In their research, a redundant manipulator was utilized for several purposes. First, the extra degrees of freedom could be used for singularity prevention in the Jacobian matrix. Second, they could be used for

collision avoidance with the environment. Finally, they were used to avoid local minimum created by the potential field function.

Borenstein and Koren [38] [39] [40] used a sensor/model hybrid scheme in a remote controlled mobile robot. The total control command composed of the human input and the potential field force from the proximity sensors. The potential field was generated based on the proximity sonar sensors. Basically the environment is divided into a grid array. Each individual cell was assigned a certainty value (CV) based on the statistical sensor reading. If the end effector is far away from the obstacle, its influence is not significant. However, when the end effector comes close to the obstacle, the potential field will play a major role in determining the state trajectory of the end effector.

Volpe and Khosla [41] proposed superquadric isopotential functions for designing repulsive wall, approaching surface and attractive well. When adding a repulsive wall and an attractive well, one should pay particular attention to the local minima that might be created from the summing process of the attractive and repulsive force fields. A manipulator might trap in one of these local minima and wouldn't be able to get out. By using superquadric isopotential functions, local minima can be avoided. In their paper, they also mentioned the concept of approach potential. An approach potential reduces the approaching velocity by converting the system kinetic energy into potential energy so the end effector won't collide and damage the work piece that it is going to pick up.

In a cluttered environment, the computational overhead for a model based collision avoidance scheme can be high simply due to a large number of obstacles in the workspace. Strenn, Hsia and Wilhelmsen [42] proposed a segmentation algorithm to save the need for intensive computation required. In the algorithm, any object within a certain region was

considered an obstacle and its effect was taken into account. However, for those outside the region, the algorithm simply ignored their effect on the effector trajectory.

The IAD at ISU is a further development of human extender and cobot. It is capable of avoiding collision with the environment while safety and performance of the operator can be significantly improved. In Chapter 2, overall system modeling of the mechanism will be provided. The system controller and the stability proofs will be elaborated in Chapter 3. Experimental results will be presented and discussed in Chapter 4. Finally, conclusions and future work will be given in Chapter 5.

CHAPTER 2 DYNAMIC MODELING

In order to explore different control algorithms developed for this project, a kinematical relationship is derived by the standard robotic formulation, and a dynamic model is developed by direct application of the Lagrange Equation. The approach in modeling the kinematics and dynamics of a simple air manipulator (SAM) can be described by (1) solid modeling & assembly, (2) kinematic derivation, (3) dynamic formulation using Lagrange's equation and, (4) constraint equation. The servo motor amplifier dynamics will be modeled and investigated. Structural resonance of the machine will be addressed and a controller compensating for the structural flexibility will be discussed.

Solid Modeling & Assembly

Physical properties such as weight, CG, mass moment of inertia of the mechanism are needed when developing the dynamic equations of the mechanism. These properties can be obtained either experimentally or analytically. In this research, every individual part of the mechanism is constructed in a solid modeling package. Once a part is modeled, the physical properties can be calculated by specifying the density of the part. Table 2.1 shows the parts that have significant contribution to the dynamics of the mechanism. Figure 2.1 shows the assembly view of the mechanism and the name assigned to each important part that will be used throughout this work. Figure 2.2 shows the schematic diagram representing the kinematics of the mechanism. Once all the parts of the mechanism have been modeled, the

connectivity between parts has to be understood so that the kinematical relationships of the mechanism can be written. Figure 2.2 shows the schematic diagram of the SAM.

Kinematics

Kinematics is the study of the position, velocity and acceleration of a system, independent of the forces that produce the motion. In the original configuration, the SAM is only powered by a pneumatic actuator in the vertical direction to provide the lifting force. Due to the parallelogram linkage design of the machine, its end effector will move on a horizontal plane if the pneumatic actuator is held fixed. In this research, the vertical motion is controlled separately by a pneumatic valve and it is not incorporated into the control law. In addition, the vertical displacement of the end effector is not changed when the machine is in motion. Therefore in the kinematics, we neglect this degree of freedom and model the machine as a RPR, a 3-degree-of-freedom robot as shown in Figure 2.3.

Table 2.1: Physical properties of the SAM.

Drawing Number	Name	Weight (kg)	Mass Moment of Inertia about CG (kg m^2)	CG from Pivot (m)
8532316	Force Link (link 2)	9.88	0.22864	NA
8534503	Parallel Linkage Vertical Arm (link 4)	10.40	2.99003	0.9342
8606210	Horizontal Arm Welded Assembly (link 1)	68.58	33.2995	0.5513
8532203	Parallel Linkage Horizontal Arm (link 3)	9.88	2.644	NA
8532329	PL Down Arm (link 4)	57.32	23.4326	0.5151
8532322	Parallel Arm Weldment Assembly (link 1)	10.84	3.0213	0.5513
NA	Counter Weight	202.6	NA	0.6096

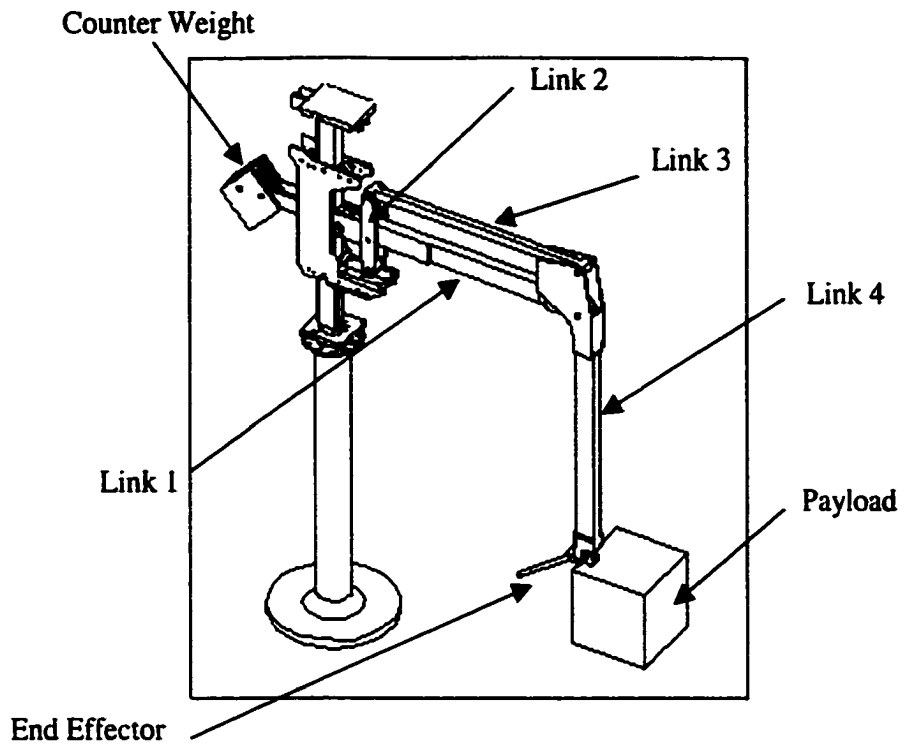


Figure 2.1: Assembly view of the SAM.

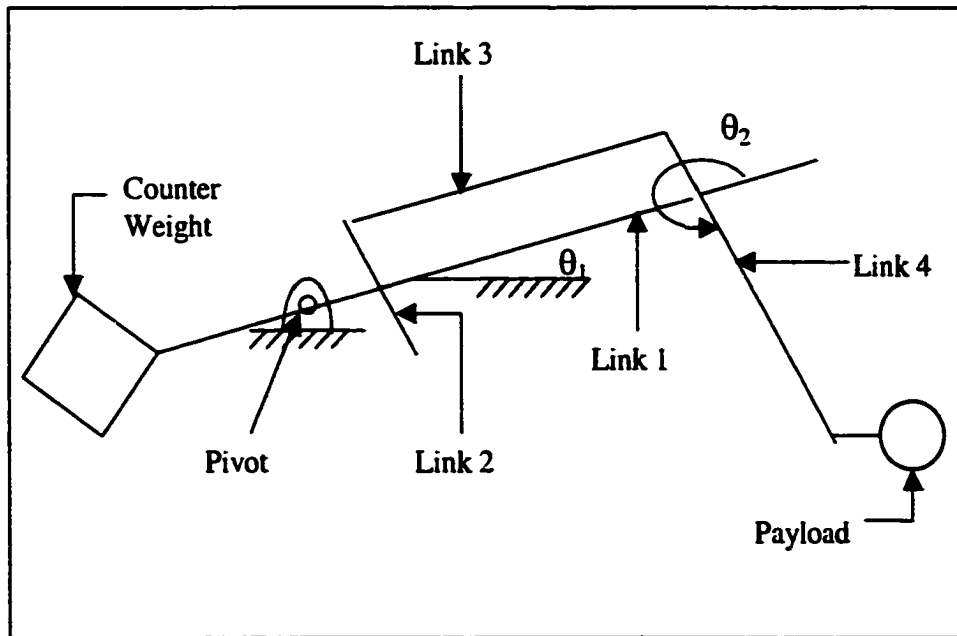


Figure 2.2: Schematic diagram of the SAM.

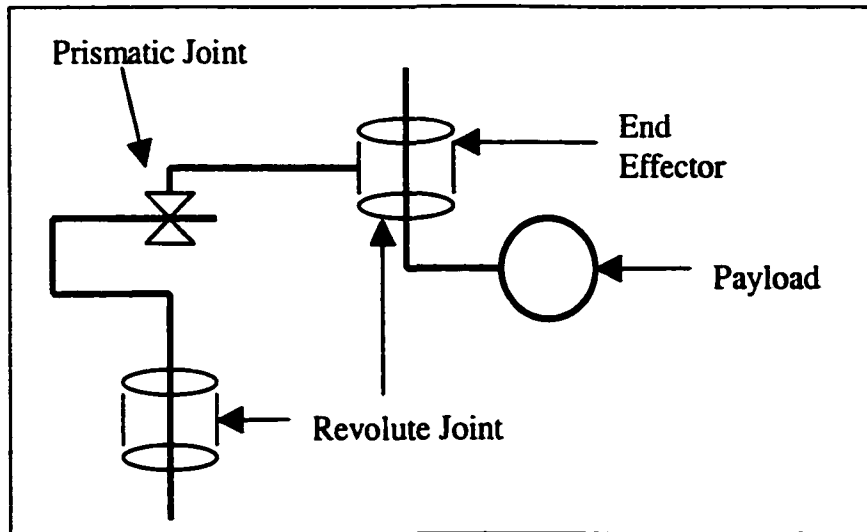


Figure 2.3: Standard robotic representation of the SAM.

The base revolute joint and the shoulder prismatic joint are primarily responsible for the displacement of the payload, whereas the wrist revolute joint is primarily responsible for the orientation of the payload.

Figure 2.4 shows the top view of the mechanism and the coordinate frames assignment. The coordinate frames are assigned according to the standard robotic practice. Note that the angular variables (θ_0 , θ_3) shown in Figure 2.4 are different from the standard practice. This is because in the dynamic analysis, that will be discussed in the next section, two more angular variables, θ_1 and θ_2 , are needed to fully describe the dynamics of the mechanism. A set of Denavit-Hartenberg (DH) parameters, which describes the link itself and its connection to a neighboring link, are tabulated in Table 2.2.

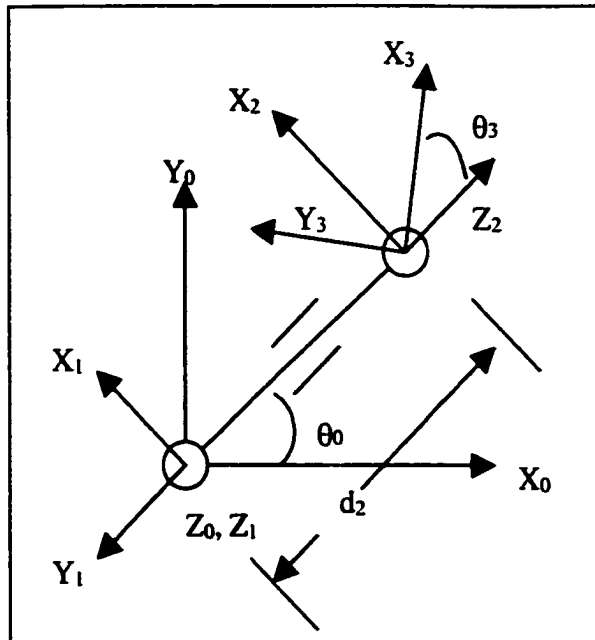


Figure 2.4: Coordinate frames assignment for the SAM.

Table 2.2: DH parameters describing the SAM.

	a_{i-1}	α_{i-1}	d_i	θ_i
1	0	0	0	$\theta_0 + 90^\circ$
2	0	90°	d_2	0
3	0	-90°	0	$\theta_3 - 90^\circ$

a_i = the distance from Z_i to Z_{i+1} measured along X_i .

α_{i-1} = the angle between Z_i and Z_{i+1} measured about X_i .

d_i = the distance from X_{i-1} to X_i measured along Z_i .

θ_i = the angle between X_{i-1} and X_i measured about Z_i .

The transformation matrices from frame {1} back to frame {0}, frame {2} to frame {1}, and frame {3} to frame {2} are

$${}^0_1T = \begin{bmatrix} -s_0 & -c_0 & 0 & 0 \\ c_0 & -s_0 & 0 & 0 \\ 0 & 0 & 1 & 0 \\ 0 & 0 & 0 & 1 \end{bmatrix}$$

$${}^1_2T = \begin{bmatrix} 1 & 0 & 0 & 0 \\ 0 & 0 & -1 & -d_2 \\ 0 & 1 & 0 & 0 \\ 0 & 0 & 0 & 1 \end{bmatrix}$$

$${}^2_3T = \begin{bmatrix} s_3 & c_3 & 0 & 0 \\ 0 & 0 & 1 & 0 \\ c_3 & -s_3 & 0 & 0 \\ 0 & 0 & 0 & 1 \end{bmatrix}$$

The total transformation matrix from frame {3} to frame {0} can be expressed as

$${}^0_3T = {}^0_1T {}^1_2T {}^2_3T = \begin{bmatrix} -s_0 & -c_0 & 0 & 0 \\ c_0 & -s_0 & 0 & 0 \\ 0 & 0 & 1 & 0 \\ 0 & 0 & 0 & 1 \end{bmatrix} \begin{bmatrix} 1 & 0 & 0 & 0 \\ 0 & 0 & -1 & -d_2 \\ 0 & 1 & 0 & 0 \\ 0 & 0 & 0 & 1 \end{bmatrix} \begin{bmatrix} s_3 & c_3 & 0 & 0 \\ 0 & 0 & 1 & 0 \\ c_3 & -s_3 & 0 & 0 \\ 0 & 0 & 0 & 1 \end{bmatrix}$$

$${}^0_3T = \begin{bmatrix} c_{03} & -s_{03} & 0 & c_0 d_2 \\ s_{03} & c_{03} & 0 & s_0 d_2 \\ 0 & 0 & 1 & 0 \\ 0 & 0 & 0 & 1 \end{bmatrix}$$

The position of the payload, assuming a distance of l_e from the end effector, can be written in frame {0} as

$${}^0R = {}^0_3T \begin{bmatrix} l_e \\ 0 \\ 0 \\ 1 \end{bmatrix} = \begin{bmatrix} l_e c_{03} + c_0 d_2 \\ l_e s_{03} + s_0 d_2 \\ 0 \\ 1 \end{bmatrix}$$

The Jacobian matrix 0J is ${}^0J = \begin{bmatrix} -s_0d_2 - l_e s_{03} & c_0 & -l_e s_{03} \\ c_0d_2 + l_e c_{03} & s_0 & l_e c_{03} \\ 0 & 0 & 0 \end{bmatrix}$

Note that the 0J expression shown above does not consider the orientation of the payload.

To include the effect, we augment the matrix to be

$${}^0J = \begin{bmatrix} -s_0d_2 - l_e s_{03} & c_0 & -l_e s_{03} \\ c_0d_2 + l_e c_{03} & s_0 & l_e c_{03} \\ 1 & 0 & 1 \end{bmatrix}$$

Eq (2.1) can be used to find out the equivalent joint torques due to the external applied forces at the payload.

$$\{\tau\} = {}^0J^T {}^0R_3 \cdot {}^3\{F\} \quad (2.1)$$

Where ${}^3\{F\}$ is the external applied-forces at the payload measured in frame {3}.

Note that $\{\tau\}$ is a 3x1 vector. The first element represents the equivalent joint torque on link 1, the second element represents the equivalent linear force from the prismatic actuator and the last element is the equivalent joint torque on the wrist joint. ${}^3\{F\}$ is a 3x1 vector corresponding to the forces in X_3 , Y_3 , and moment about Z_3 axis as shown in Figure 2.4. Eq (2.1) depicts how the external applied forces can be mapped into the corresponding joint torques. However, it does not reveal how the mechanism will react to the external applied forces. This brings us to the discussion of dynamic modeling, which describes the relationship between the system response and the applied force/motion, in the next section.

Dynamic Formulation of the SAM

From Table 2.1, one will find that link 2 and link 3 of the mechanism have lower inertia compared to the load carrying beams- link 1 and link 4. The inertia of link 2 is only 1% of link 4. While link 3 is about 8.3% of the inertia of link 1. Therefore, both link 2 and 3 are assumed to have negligible masses in the analysis. After this assumption, the mechanism can be simplified as shown in Figure 2.5(b). Figure 2.5 shows the differences between the kinematic model and the dynamic model that will be developed in the following section. In the kinematic model, the payload is only able to move on a horizontal plane when the pneumatic actuator is held fixed. Therefore the system is modeled as a 3-degree-of-freedom system. In contrary, the machine is modeled as a 4-degree-of-freedom system in the dynamic formulation. From Figure 2.5(a), one can see that the motions of link 1 and 4 are dependent on each other. In the dynamic formulation that will be presented, we will first derive the equations of motion with no constraint on the motions of link 1 and 4. A constraint equation will be developed next to reflect their motion dependencies.

The machine is originally designed to manipulate a light to moderate weight object. To reduce the physical labor of the operator, the overall machine inertia is minimized by making the arms thin and light. In Figure 2.5, although the payload is shown at a distance l_e from the end effector, in the actual operation, the payload is placed relatively close to the end effector to avoid imposing excessive moment due to the gravity on the machine. In short, l_e is very small.

In the dynamic formulation, we assume that the payload is placed at the revolute end joint, and the dynamic effect of the payload can be lumped into link 4. After making this assumption, the system can be simplified as shown in Figure 2.6. In Figure 2.6, θ_1 and θ_2 are

the joint angle variables describing the motions of link 1 and link 4 respectively. Their axes are always having the same direction and lying on XY plane, whereas θ_0 axis, which describes the motion of the base joint, is always perpendicular to XY plane.

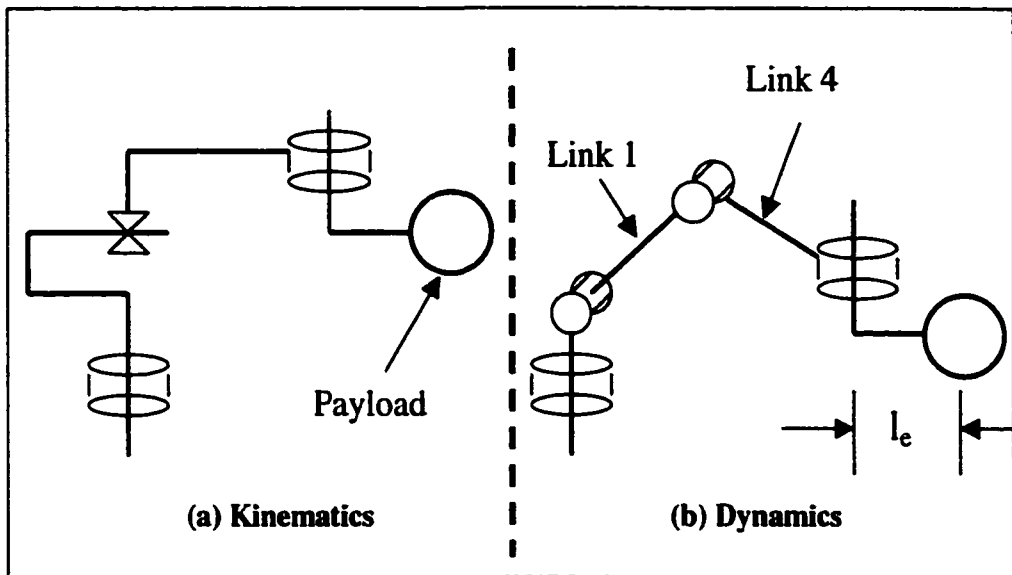


Figure 2.5: Comparison of kinematics and dynamics.

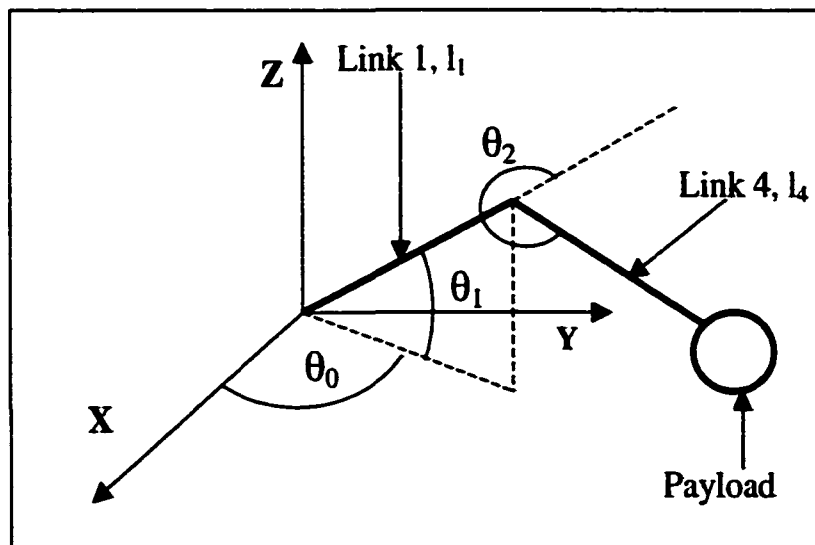


Figure 2.6: Dynamic representation of the SAM.

Lagrange's Equations

Lagrange's equations are used to derive the dynamics of the machine. In the following derivation, we do not place any constraint on the motions of θ_1 and θ_2 .

We begin with the potential energy of link 1, V_1 .

$$V_1 = m_1 g l_{c1} \sin \theta_1$$

l_{c1} is the distance from the pivot point to the mass center of link 1, m_1 is the mass of link 1 and g is the gravity constant. The angular velocity of link 1 can be written as

$$\bar{\omega}_1 = \langle \dot{\theta}_1 \sin \theta_0 \quad -\dot{\theta}_1 \cos \theta_0 \quad \dot{\theta}_0 \rangle^T$$

The velocity of link 1 centroid is $\bar{v}_1 = l_{c1} \langle -\dot{\theta}_0 s_0 c_1 - \dot{\theta}_1 c_0 s_1 \quad \dot{\theta}_0 c_0 c_1 - \dot{\theta}_1 s_0 s_1 \quad \dot{\theta}_1 c_1 \rangle^T$.

Mass Moment of Inertia

For a long, thin rod, the mass moment of inertia about its longitudinal axis is relatively small compared to the inertia about its transverse axes. To simplify the analysis, we assume that the mass moment of inertia of all the links about their longitudinal axes can be neglected. As shown in Figure 2.7, $I_{x'x'}$, which is a principle mass-moment of inertia of a link, is assumed to be zero. We further assume that the inertias about the transverse axes are about the same, namely $I_{y'y'} = I_{z'z'} = I_1$. By making these assumptions, the inertia tensor of link 1 can be written as:

$$[I_{1_principle}] = \begin{bmatrix} 0 & 0 & 0 \\ 0 & I_1 & 0 \\ 0 & 0 & I_1 \end{bmatrix}$$

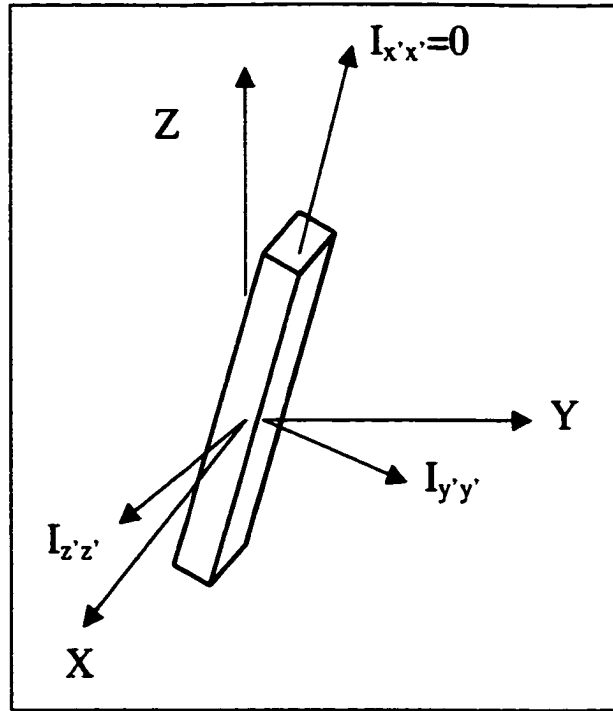


Figure 2.7: Mass moment of inertia of Link 1.

The transformation matrix from a local coordinate system (x' , y' , z') to the global Cartesian coordinate system can be expressed as

$${}^0_2R = \begin{bmatrix} c_0 & -s_0 & 0 \\ s_0 & c_0 & 0 \\ 0 & 0 & 1 \end{bmatrix} \begin{bmatrix} c_1 & 0 & -s_1 \\ 0 & 1 & 0 \\ s_1 & 0 & c_1 \end{bmatrix} = \begin{bmatrix} c_0 c_1 & -s_0 & -c_0 s_1 \\ s_0 c_1 & c_0 & -s_0 s_1 \\ s_1 & 0 & c_1 \end{bmatrix}$$

where $s_0 = \sin \theta_0$, $c_0 = \cos \theta_0$, $s_1 = \sin \theta_1$ and $c_1 = \cos \theta_1$.

The inertia of link 1 can be represented in the global Cartesian coordinate system by the following transformation. From the conservation of energy,

$$\frac{1}{2} {}^0\bar{\omega}^T \cdot {}^0 [I_{1_Cartesian}] \cdot {}^0 \bar{\omega} = \frac{1}{2} {}^2\bar{\omega}^T \cdot {}^2 [I_{1_principle}] \cdot {}^2 \bar{\omega} = \frac{1}{2} ({}^2_0R^0 \bar{\omega})^T \cdot {}^2 [I_{1_principle}] \cdot {}^2_0R^0 \bar{\omega}$$

where ${}^0\bar{\omega}$ is the angular velocity of link 1, and $I_{1_Cartesian}$ is the inertia tensor. Both ${}^0\bar{\omega}$ and $I_{1_Cartesian}$ are expressed in the global Cartesian coordinate system.

The expression can be rewritten as

$$[I_{1_Cartesian}] = {}_0^2R^T \cdot [I_{1_principle}]_0^2R = {}_2^0R \cdot [I_{1_principle}]_2^0R^T$$

$$[I_{1_Cartesian}] = \begin{bmatrix} c_0c_1 & -s_0 & -c_0s_1 \\ s_0c_1 & c_0 & -s_0s_1 \\ s_1 & 0 & c_1 \end{bmatrix} \begin{bmatrix} 0 & 0 & 0 \\ 0 & I_1 & 0 \\ 0 & 0 & I_1 \end{bmatrix} \begin{bmatrix} c_0c_1 & s_0c_1 & s_1 \\ -s_0 & c_0 & 0 \\ -c_0s_1 & -s_0s_1 & c_1 \end{bmatrix}$$

$$[I_{1_Cartesian}] = \begin{bmatrix} I_1(1 - c_0^2c_1^2) & -I_1s_0c_0c_1^2 & -I_1c_0s_1c_1 \\ -I_1s_0c_0c_1^2 & I_1 - I_1c_1^2 + I_1c_0^2c_1^2 & -I_1s_0s_1c_1 \\ -I_1c_0s_1c_1 & -I_1s_0s_1c_1 & I_1c_1^2 \end{bmatrix}$$

The kinetic energy of link 1 can be written as

$$T_1 = \frac{1}{2}m_1\bar{v}_1 \cdot \bar{v}_1^T + \frac{1}{2}\bar{\omega}_1^T \cdot [I_{1_Cartesian}] \cdot \bar{\omega}_1$$

The Lagrange function of link 1 is

$$L_1 = T_1 - V_1 = \frac{1}{2}(\dot{\theta}_0^2 \cos^2 \theta_1 + \dot{\theta}_1^2)(m_1l_{c1}^2 + I_1) - m_1gl_{c1} \sin \theta_0$$

Following the same procedures, we can proceed to link 4. The potential energy of link 4 is

$$V_4 = m_4g[l_1 \sin \theta_1 + l_{c4} \sin(\theta_1 + \theta_2)],$$

where l_{c4} is the distance to the mass center of link 4, m_4 is the effective mass of link 4 and payload at the end effector.

The angular velocity of link 4 can be written as

$$\bar{\omega}_4 = \langle (\dot{\theta}_1 + \dot{\theta}_2) \sin \theta_0, -(\dot{\theta}_1 + \dot{\theta}_2) \cos \theta_0, \dot{\theta}_0 \rangle^T$$

The position vector of link 4 centroid is

$$p_4 = \begin{pmatrix} (l_{c_4}c_{12} + l_1c_1)c_0 \\ (l_{c_4}c_{12} + l_1c_1)s_0 \\ l_1s_1 + l_{c_4}s_{12} \end{pmatrix}$$

The velocity of link 4 centroid can be expressed as

$$\bar{v}_4 = \begin{pmatrix} -(l_{c_4}c_{12} + l_1c_1)s_0\dot{\theta}_0 - (l_1s_1\dot{\theta}_1 + l_{c_4}s_{12}(\dot{\theta}_1 + \dot{\theta}_2))c_0 \\ (l_{c_4}c_{12} + l_1c_1)c_0\dot{\theta}_0 - (l_1s_1\dot{\theta}_1 + l_{c_4}s_{12}(\dot{\theta}_1 + \dot{\theta}_2))s_0 \\ l_1c_1\dot{\theta}_1 + l_{c_4}c_{12}(\dot{\theta}_1 + \dot{\theta}_2) \end{pmatrix}$$

The principle mass-moment of inertia of link 4 can be written as:

$$[I_{4_principle}] = \begin{bmatrix} 0 & 0 & 0 \\ 0 & I_4 & 0 \\ 0 & 0 & I_4 \end{bmatrix}$$

The transformation matrix from frame {3} to frame {0} can be expressed as

$${}^0_3R = \begin{bmatrix} c_0c_{12} & -s_0 & -c_0s_{12} \\ s_0c_{12} & c_0 & -s_0s_{12} \\ s_{12} & 0 & c_{12} \end{bmatrix}, \text{ where } s_{12} = \sin(\theta_1 + \theta_2), c_{12} = \cos(\theta_1 + \theta_2).$$

The inertia of link 4 can be represented in the global Cartesian coordinate system as

$$[I_{4_Cartesian}] = {}^0_3R \cdot [I_{4_principle}] \cdot {}^3_0R$$

The kinetic energy of link 4 can be written as

$$T_4 = \frac{1}{2} m_4 \bar{v}_4^T \cdot \bar{v}_4 + \frac{1}{2} \bar{\omega}_4^T \cdot [I_{4_Cartesian}] \cdot \bar{\omega}_4$$

The Lagrange function of link 4 is $L_4 = T_4 - V_4$

The Lagrange function for the machine is simply the sum of L_1 and L_4 , which can be expressed as

$$\begin{aligned}
L = & \frac{1}{2}\dot{\theta}_0^2 [m_1 l_{c1}^2 c_1^2 + I_1 c_1^2 + I_4 c_{12}^2 + m_4 l_{c4}^2 c_{12}^2 + m_4 l_1^2 c_1^2 + 2m_4 l_1 l_{c4} c_1 c_{12}] \\
& + \frac{1}{2}\dot{\theta}_1^2 [m_1 l_{c1}^2 + I_1 + m_4 l_1^2 + m_4 l_{c4}^2 + 2m_4 l_1 l_{c4} c_2 + I_4] \\
& + \frac{1}{2}\dot{\theta}_2^2 [I_4 + m_4 l_{c4}^2] + \dot{\theta}_1 \dot{\theta}_2 [m_4 l_1 l_{c4} c_2 + I_4 + m_4 l_{c4}^2] \\
& - [m_1 l_{c1} s_1 + m_4 (l_1 s_1 + l_{c4} s_{12})] g
\end{aligned}$$

Applying Lagrange formulation, $T = \frac{d}{dt} \left(\frac{\partial L}{\partial \dot{\theta}} \right) - \frac{\partial L}{\partial \theta}$, to all the variables, namely $\theta_0, \theta_1, \theta_2$,

we get

$$\begin{aligned}
T_0 = & [m_1 l_{c1}^2 c_1^2 + m_4 (l_1^2 c_1^2 + l_{c4}^2 c_{12}^2) + 2m_4 l_1 l_{c4} c_1 c_{12} + I_1 c_1^2 + I_4 c_{12}^2] \ddot{\theta}_0 \\
& - 2[(m_1 l_{c1}^2 + m_4 l_1^2) c_1 s_1 + m_4 l_1 l_{c4} \sin(2\theta_1 + \theta_2) + m_4 l_{c4}^2 c_{12} s_{12} + I_1 c_1 s_1 + I_4 c_{12} s_{12}] \dot{\theta}_0 \dot{\theta}_1 \\
& - 2[I_4 c_{12} + m_4 l_{c4}^2 c_{12} + m_4 l_1 l_{c4} c_1] s_{12} \dot{\theta}_0 \dot{\theta}_2
\end{aligned} \quad (2.2)$$

$$\begin{aligned}
T_1 = & [m_4 (l_1^2 + l_{c4}^2) + m_1 l_{c1}^2 + I_1 + I_4 + 2m_4 l_1 l_{c4} c_2] \ddot{\theta}_1 + (m_4 l_{c4}^2 + I_4 + m_4 l_1 l_{c4} c_2) \ddot{\theta}_2 \\
& + [m_1 l_{c1}^2 c_1 s_1 + I_1 c_1 s_1 + I_4 c_{12} s_{12} + m_4 l_1 l_{c4} \sin(2\theta_1 + \theta_2) + m_4 (l_1^2 c_1 s_1 + l_{c4}^2 c_{12} s_{12})] \dot{\theta}_0^2 \\
& - m_4 l_1 l_{c4} s_2 \dot{\theta}_2^2 - 2m_4 l_1 l_{c4} s_2 \dot{\theta}_1 \dot{\theta}_2 + [m_1 l_{c1} c_1 + m_4 (l_1 c_1 + l_{c4} c_{12})] g
\end{aligned} \quad (2.3)$$

$$\begin{aligned}
T_2 = & [m_4 l_1 l_{c4} c_2 + m_4 l_{c4}^2 + I_4] \ddot{\theta}_1 + (m_4 l_{c4}^2 + I_4) \ddot{\theta}_2 \\
& + [I_4 c_{12} s_{12} + m_4 l_{c4} s_{12} (l_1 c_1 + l_{c4} c_{12})] \dot{\theta}_0^2 + m_4 l_1 l_{c4} s_2 \dot{\theta}_1^2 + m_4 g l_{c4} c_{12}
\end{aligned} \quad (2.4)$$

The torque expressions can be written in a compact matrix notation as

$$\begin{Bmatrix} T_0 \\ T_1 \\ T_2 \end{Bmatrix} = H(\theta) \begin{Bmatrix} \ddot{\theta}_0 \\ \ddot{\theta}_1 \\ \ddot{\theta}_2 \end{Bmatrix} + C(\dot{\theta}, \theta) \begin{Bmatrix} \dot{\theta}_0 \\ \dot{\theta}_1 \\ \dot{\theta}_2 \end{Bmatrix} + G(\theta) \quad (2.5)$$

$$H(\theta) = \begin{bmatrix} h_{11} & 0 & 0 \\ 0 & h_{22} & h_{23} \\ 0 & h_{32} & h_{33} \end{bmatrix}, C(\dot{\theta}, \theta) = \begin{bmatrix} c_{11} & c_{12} & c_{13} \\ c_{21} & c_{22} & c_{23} \\ c_{31} & c_{32} & c_{33} \end{bmatrix}, G(\theta) = \begin{Bmatrix} 0 \\ g_2 \\ g_3 \end{Bmatrix}$$

$$h_{11} = [m_1 l_{c1}^2 c_1^2 + m_4 (l_1^2 c_1^2 + l_{c4}^2 c_{12}^2) + 2m_4 l_1 l_{c4} c_1 c_{12} + I_1 c_1^2 + I_4 c_{12}^2]$$

$$h_{22} = [m_4 (l_1^2 + l_{c4}^2) + m_1 l_{c1}^2 + I_1 + I_4 + 2m_4 l_1 l_{c4} c_2]$$

$$h_{23} = (m_4 l_{c4}^2 + I_4 + m_4 l_1 l_{c4} c_2)$$

$$h_{32} = [m_4 l_1 l_{c4} c_2 + m_4 l_{c4}^2 + I_4]$$

$$h_{33} = (m_4 l_{c4}^2 + I_4)$$

$$c_{11} = -[(m_1 l_{c1}^2 + m_4 l_1^2) c_1 s_1 + m_4 l_1 l_{c4} \sin(2\theta_1 + \theta_2) + m_4 l_{c4}^2 c_{12} s_{12} + I_1 c_1 s_1 + I_4 c_{12} s_{12}] \dot{\theta}_1 \\ - [I_4 c_{12} + m_4 l_{c4}^2 c_{12} + m_4 l_1 l_{c4} c_1] s_{12} \dot{\theta}_2$$

$$c_{12} = -[(m_1 l_{c1}^2 + m_4 l_1^2) c_1 s_1 + m_4 l_1 l_{c4} \sin(2\theta_1 + \theta_2) + m_4 l_{c4}^2 c_{12} s_{12} + I_1 c_1 s_1 + I_4 c_{12} s_{12}] \dot{\theta}_0$$

$$c_{13} = -[I_4 c_{12} + m_4 l_{c4}^2 c_{12} + m_4 l_1 l_{c4} c_1] s_{12} \dot{\theta}_0$$

$$c_{21} = [m_1 l_{c1}^2 c_1 s_1 + I_1 c_1 s_1 + I_4 c_{12} s_{12} + m_4 l_1 l_{c4} \sin(2\theta_1 + \theta_2) + m_4 (l_1^2 c_1 s_1 + l_{c4}^2 c_{12} s_{12})] \dot{\theta}_0$$

$$c_{22} = -m_4 l_1 l_{c4} s_2 \dot{\theta}_2$$

$$c_{23} = -m_4 l_1 l_{c4} s_2 \dot{\theta}_2 - m_4 l_1 l_{c4} s_2 \dot{\theta}_1$$

$$c_{31} = [I_4 c_{12} s_{12} + m_4 l_{c4} s_{12} (l_1 c_1 + l_{c4} c_{12})] \dot{\theta}_0$$

$$c_{32} = m_4 l_1 l_{c4} s_2 \dot{\theta}_1$$

$$g_2 = [m_1 l_{c1} c_1 + m_4 (l_1 c_1 + l_{c4} c_{12})] g$$

$$g_3 = m_4 g l_{c4} c_{12}$$

where $C(\dot{\theta}, \theta)$ represents the terms involving centripetal and Coriolis acceleration, whereas

$G(\theta)$ represents the gravity effect. $\dot{H} - 2C$ is skew symmetric.

Constraint Equation

The dynamic equations derived in the previous section placed no restriction on the motion of the end effector. In fact, the end effector will move on a horizontal plane if the pneumatic valve is held fixed when the machine is in motion. In other words, the pneumatic actuator is able to hold the relative height of the end effector stationary with respect to the ground. To describe this behavior, a constraint equation is needed to express the relationship between θ_1 and θ_2 . Figure 2.8 shows the constrained motion of the end effector. The height of the end effector, Z , can be expressed as

$$Z = r \sin \theta_1 + r \sin(\theta_1 + \theta_2) \quad (2.6)$$

Taking a partial of Eq (2.6), we get

$$\Delta Z = r \cos \theta_1 \cdot \Delta \theta_1 + r \cos(\theta_1 + \theta_2) \cdot (\Delta \theta_1 + \Delta \theta_2) \quad (2.7)$$

Since the height of the end effector is a constant, therefore $\Delta Z = 0$. Eq (2.7) can be rewritten as

$$\Delta \theta_1 = \frac{-\cos(\theta_1 + \theta_2)}{\cos \theta_1 + \cos(\theta_1 + \theta_2)} \Delta \theta_2 = \frac{-c_{12}}{c_1 + c_{12}} \Delta \theta_2 \quad (2.8)$$

Divided Eq (2.8) by Δt and taking limit, we get:

$$\dot{\theta}_1 = \frac{-c_{12}}{c_1 + c_{12}} \dot{\theta}_2 \quad (2.9)$$

Taking a time derivative of Eq (2.9), we get:

$$\ddot{\theta}_1 = \frac{-c_{12}}{c_1 + c_{12}} \ddot{\theta}_2 + \frac{\partial}{\partial t} \left(\frac{-c_{12}}{c_1 + c_{12}} \right) \dot{\theta}_2$$

$$\ddot{\theta}_1 = \frac{-c_{12}}{c_1 + c_{12}} \ddot{\theta}_2 + f_1 \dot{\theta}_2 \quad (2.10)$$

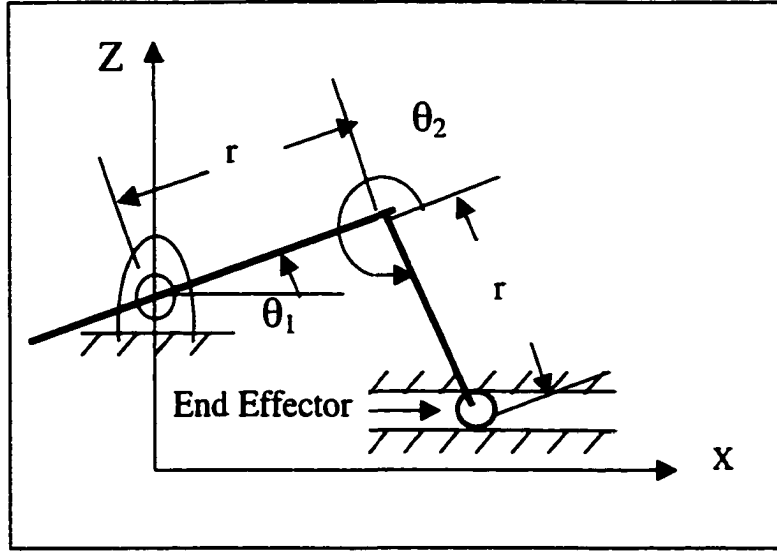


Figure 2.8: Constrained end effector motion.

We can replace the expressions of $\ddot{\theta}_1$ and $\dot{\theta}_1$ in the equations of motion by Eq (2.9) and Eq (2.10). The equations of motion, Eq (2.2), Eq (2.3) and Eq (2.4) can be rewritten as

$$\begin{aligned}
 T_0 = & [m_1 l_{c1}^2 c_1^2 + m_4 (l_1^2 c_1^2 + l_{c4}^2 c_{12}^2) + 2m_4 l_1 l_{c4} c_1 c_{12} + I_1 c_1^2 + I_4 c_{12}^2] \ddot{\theta}_0 \\
 & - 2[(m_1 l_{c1}^2 + m_4 l_1^2) c_1 s_1 + m_4 l_1 l_{c4} \sin(2\theta_1 + \theta_2) + m_4 l_{c4}^2 c_{12} s_{12} + I_1 c_1 s_1 + I_4 c_{12} s_{12}] \dot{\theta}_0 \cdot \left(\frac{-c_{12}}{c_1 + c_{12}} \right) \dot{\theta}_2 \\
 & - 2[I_4 c_{12} + m_4 l_{c4}^2 c_{12} + m_4 l_1 l_{c4} c_1] s_{12} \dot{\theta}_0 \dot{\theta}_2
 \end{aligned} \tag{2.11}$$

$$\begin{aligned}
 T_1 = & [m_4 (l_1^2 + l_{c4}^2) + m_1 l_{c1}^2 + I_1 + I_4 + 2m_4 l_1 l_{c4} c_2] \left(\frac{-c_{12}}{c_1 + c_{12}} \ddot{\theta}_2 + f_1 \dot{\theta}_2 \right) + (m_4 l_{c4}^2 + I_4 + m_4 l_1 l_{c4} c_2) \ddot{\theta}_2 \\
 & + [m_1 l_{c1}^2 c_1 s_1 + I_1 c_1 s_1 + I_4 c_{12} s_{12} + m_4 l_1 l_{c4} \sin(2\theta_1 + \theta_2) + m_4 (l_1^2 c_1 s_1 + l_{c4}^2 c_{12} s_{12})] \dot{\theta}_0^2 \\
 & - m_4 l_1 l_{c4} s_2 \dot{\theta}_2^2 - 2m_4 l_1 l_{c4} s_2 \left(\frac{-c_{12}}{c_1 + c_{12}} \right) \dot{\theta}_2^2 + [m_1 l_{c1} c_1 + m_4 (l_1 c_1 + l_{c4} c_{12})] g
 \end{aligned} \tag{2.12}$$

$$\begin{aligned}
T_2 = & [m_4 l_1 l_{c4} c_2 + m_4 l_{c4}^2 + I_4] \left(\frac{-c_{12}}{c_1 + c_{12}} \ddot{\theta}_2 + f_1 \dot{\theta}_2 \right) + (m_4 l_{c4}^2 + I_4) \ddot{\theta}_2 \\
& + [I_4 c_{12} s_{12} + m_4 l_{c4} s_{12} (l_1 c_1 + l_{c4} c_{12})] \dot{\theta}_0^2 + m_4 l_1 l_{c4} s_2 \left(\frac{-c_{12}}{c_1 + c_{12}} \right)^2 \dot{\theta}_2^2 + m_4 g l_{c4} c_{12}
\end{aligned} \tag{2.13}$$

These expressions can be written in a compact matrix notation as

$$\begin{Bmatrix} T_0 \\ T_1 \\ T_2 \end{Bmatrix} = \begin{bmatrix} H_{11} & 0 \\ 0 & H_{22} \\ 0 & H_{32} \end{bmatrix} \begin{Bmatrix} \ddot{\theta}_0 \\ \ddot{\theta}_2 \end{Bmatrix} + \begin{Bmatrix} v_0 \\ v_1 \\ v_2 \end{Bmatrix} + \begin{Bmatrix} 0 \\ g_2 \\ g_3 \end{Bmatrix} \tag{2.14}$$

where

$$H_{11} = [m_1 l_{c1}^2 c_1^2 + m_4 (l_1^2 c_1^2 + l_{c4}^2 c_{12}^2) + 2m_4 l_1 l_{c4} c_1 c_{12} + I_1 c_1^2 + I_4 c_{12}^2] \tag{2.15}$$

$$\begin{aligned}
H_{22} = & [m_4 (l_1^2 + l_{c4}^2) + m_1 l_{c1}^2 + I_1 + I_4 + 2m_4 l_1 l_{c4} c_2] \left(\frac{-c_{12}}{c_1 + c_{12}} \right) + (m_4 l_{c4}^2 + I_4 + m_4 l_1 l_{c4} c_2)
\end{aligned} \tag{2.16}$$

$$H_{32} = [m_4 l_1 l_{c4} c_2 + m_4 l_{c4}^2 + I_4] \left(\frac{-c_{12}}{c_1 + c_{12}} \right) + (m_4 l_{c4}^2 + I_4) \tag{2.17}$$

The expressions for v_0, v_1 and v_2 can be extracted from Eq (2.11) to Eq (2.13) directly.

A few comments are needed for Eq (2.14). First, T_0 is the joint torque on the base degree of freedom. From Figure 2.5, we see that the base joint coordinate is the same for both kinematics and dynamics. It is not surprising to find that the expression for H_{11} is actually the same as that for h_{11} in Eq (2.5). H_{22} and H_{33} are the inertias associated with θ_1 and θ_2 when their motions are constrained so that the end effector can only move on a horizontal plane. To get the actuation and constraint forces, we need another transformation.

Mapping from Joint Space to Actuator Space

In the operation of an IAD, servo-actuators are providing the motive forces and moment to the system. Therefore, it is crucial to understand the dynamic forces acting on the servo-actuators. To reflect the machine dynamic effects, we need to rewrite the equations of motion, Eq (2.11), Eq (2.12) and Eq (2.13) in the actuator frame-of-reference. Notice that for the base joint, the actuator space is the same as the joint space. Therefore, θ_2 is the only variable in the dynamic equations that needs transformation. Referring back to Figure 2.8, the end effector displacement in the X direction can be expressed as

$$x = r\cos\theta_1 + r\cos(\theta_1 + \theta_2) \quad (2.18)$$

Taking a time derivative of Eq (2.18) yields

$$\dot{x} = r\sin\theta_1 \cdot \dot{\theta}_1 + r\sin(\theta_1 + \theta_2) \cdot (\dot{\theta}_1 + \dot{\theta}_2) \quad (2.19)$$

Substituting Eq (2.9) into Eq (2.19), we get

$$\dot{x} = \frac{-r\sin\theta_2 \cdot \dot{\theta}_2}{\cos\theta_1 + \cos(\theta_1 + \theta_2)} = \frac{-rs_2 \cdot \dot{\theta}_2}{c_1 + c_{12}} = f_2 \cdot \dot{\theta}_2 \quad (2.20)$$

where

$$f_2 = \frac{-rs_2}{c_1 + c_{12}}$$

Taking a time derivative of Eq (2.20) yields

$$\ddot{x} = f_2 \cdot \ddot{\theta}_2 + \dot{f}_2 \cdot \dot{\theta}_2 \quad (2.21)$$

where

$$\dot{f}_2 = \frac{-r\dot{\theta}_2(c_1^2 + c_1^2c_2 + c_1c_{12} + c_{12}^2 - s_2s_{12}c_{12})}{(c_1 + c_{12})^3}$$

Eq (2.21) can be expressed as

$$\ddot{\theta}_2 = \frac{\ddot{x} - \dot{f}_2 \cdot \dot{\theta}_2}{f_2} \quad (2.22)$$

Substituting Eq (2.22) into Eq (2.14), we get

$$\begin{Bmatrix} T_0 \\ T_1 \\ T_2 \end{Bmatrix} = \begin{bmatrix} H_{11} & 0 \\ 0 & H_{22} \\ 0 & H_{32} \end{bmatrix} \begin{Bmatrix} \ddot{\theta}_0 \\ \ddot{x} - \dot{f}_2 \cdot \dot{\theta}_2 / f_2 \end{Bmatrix} + \begin{Bmatrix} v_0 \\ v_1 \\ v_2 \end{Bmatrix} + \begin{Bmatrix} 0 \\ g_2 \\ g_3 \end{Bmatrix} \quad (2.23)$$

Rearranging Eq (2.23) yields

$$\begin{Bmatrix} T_0 \\ T_1 \\ T_2 \end{Bmatrix} = \begin{bmatrix} H_{11} & 0 \\ 0 & H_{22}/f_2 \\ 0 & H_{32}/f_2 \end{bmatrix} \begin{Bmatrix} \ddot{\theta}_0 \\ \ddot{x} \end{Bmatrix} + \begin{Bmatrix} v_0 - H_{22} \cdot \dot{f}_2 \cdot \dot{\theta}_2 / f_2 \\ v_1 - H_{23} \cdot \dot{f}_2 \cdot \dot{\theta}_2 / f_2 \\ v_2 - H_{23} \cdot \dot{f}_2 \cdot \dot{\theta}_2 / f_2 \end{Bmatrix} + \begin{Bmatrix} 0 \\ g_2 \\ g_3 \end{Bmatrix} \quad (2.24)$$

To get the equivalent force from the pneumatic actuator and linear actuator, we can multiply the lower two equations of Eq (2.24) by J^{-T} , where J is the Jacobian matrix that can be expressed as

$$J = \begin{bmatrix} -rs_1 - rs_{12} & -rs_{12} \\ rc_1 + rc_{12} & rc_{12} \end{bmatrix}$$

$$J^{-T} = \frac{1}{r^2 s_2} \begin{bmatrix} rc_{12} & -rc_1 - rc_{12} \\ rs_{12} & -rs_1 - rs_{12} \end{bmatrix} = \begin{bmatrix} j_{11} & j_{12} \\ j_{21} & j_{22} \end{bmatrix}$$

Actuation and constraint forces can be expressed as:

$$\begin{Bmatrix} F_{Linear} \\ F_{Pneumatic} \end{Bmatrix} = J^{-T} \begin{Bmatrix} T_1 \\ T_2 \end{Bmatrix} = \begin{bmatrix} j_{11} & j_{12} \\ j_{21} & j_{22} \end{bmatrix} \left[\begin{bmatrix} 0 & H_{22}/f_2 \\ 0 & H_{23}/f_2 \end{bmatrix} \begin{Bmatrix} \ddot{\theta}_0 \\ \ddot{x} \end{Bmatrix} + \begin{Bmatrix} v_1 - H_{22} \dot{f}_2 \dot{\theta}_2 / f_2 \\ v_2 - H_{23} \dot{f}_2 \dot{\theta}_2 / f_2 \end{Bmatrix} + \begin{Bmatrix} g_1 \\ g_2 \end{Bmatrix} \right]$$

$$\begin{Bmatrix} F_{Linear} \\ F_{Pneumatic} \end{Bmatrix} = \frac{1}{f_2} \begin{bmatrix} 0 & j_{11}H_{22} + j_{12}H_{23} \\ 0 & j_{21}H_{22} + j_{22}H_{23} \end{bmatrix} \begin{Bmatrix} \ddot{\theta}_0 \\ \ddot{x} \end{Bmatrix} + \begin{bmatrix} j_{11} & j_{12} \\ j_{21} & j_{22} \end{bmatrix} \begin{Bmatrix} v_1 - H_{22}\dot{f}_2\dot{\theta}_2 / f_2 \\ v_2 - H_{23}\dot{f}_2\dot{\theta}_2 / f_2 \end{Bmatrix} + \begin{Bmatrix} g_1 \\ g_2 \end{Bmatrix} \quad (2.25)$$

In Eq (2.25), we see that the constraint ($F_{Pneumatic}$) and actuation (F_{Linear}) forces due to **inertia effect** are independent of θ_0 . However, be aware that they are still functions of θ_0 with the first and zero derivatives.

Figure 2.9 shows the H_{11} element of Eq (2.24). The curves in Figure 2.9 were generated based on the information of the existing mechanism and we assumed that there were 0, 250 and 500 lb payloads at the end effector. From H_{11} , that represents the mass-moment of inertia about the base joint, one can see that the inertia is larger when the mechanism is in the fully extended configuration than when it is fully retracted.

Figure 2.10 shows the (1,2) element of the inertia matrix in Eq (2.25). It shows the inertia effect acting on the linear actuator. Quite opposite to the base joint, the inertia of the mechanism actually goes down as the end effector moves from the inner to the central position, and then it picks up again from the central to the outer configuration.

Figure 2.9 and Figure 2.10 are important to the design of the controller. They reveal the inertial effects that the servo actuators need to overcome at different configurations. In the following section, servomotor and amplifier dynamics will be modeled and discussed, the controller designed to compensate for the inertia effects will also be addressed.

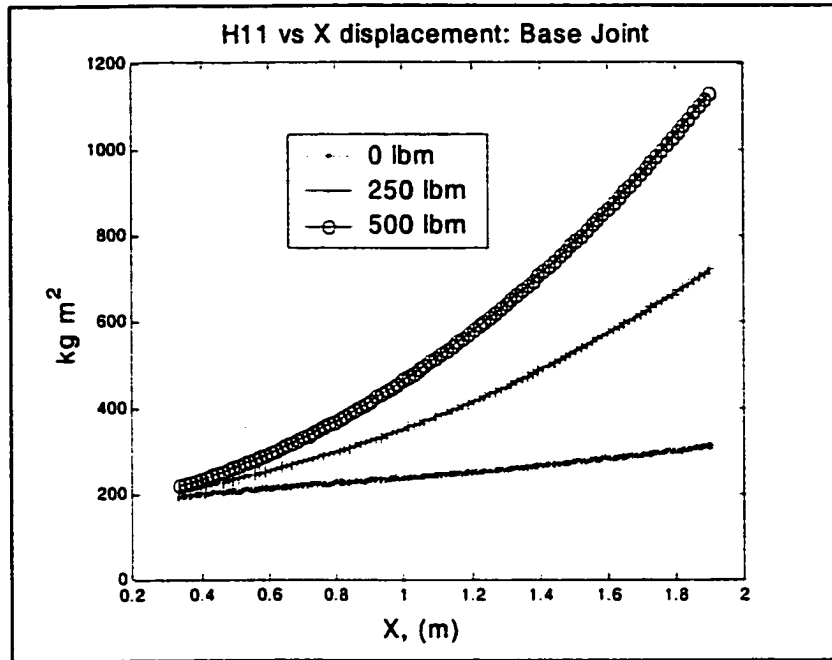


Figure 2.9: Moment of inertia of the base joint for different payloads.

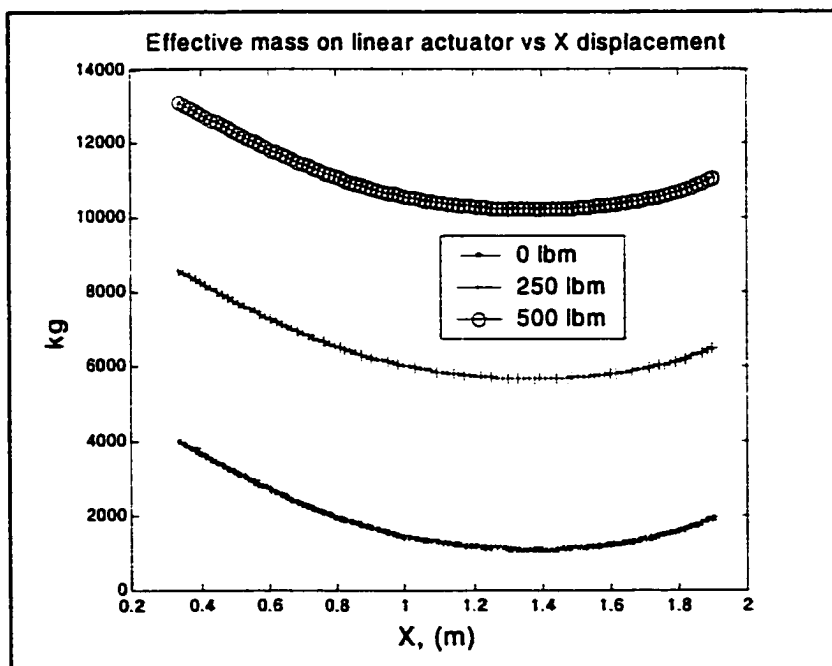


Figure 2.10: Effective mass on the linear actuator for different payloads.

Amplifier + Servomotor Dynamics Modeling

An amplifier converts a low-level analog or a digital command to a high power voltage or current necessary to drive a servomotor. There are two types of amplifiers commonly used in industry, and they are the linear amplifier and the switching amplifier. A linear amplifier has the benefit of low cost and no radiated electrical noise. However, due to high-energy dissipation of output transistors, a linear amplifier can be very hot, which usually requires a cooling system and a large heat sink. On the other hand, a switching amplifier utilizes pulse width modulation (PWM) to minimize heat generation. A switching amplifier is the most popular amplifier used in industry for its least amount of heat generated. In addition, a switching amplifier is also more efficient than a linear amplifier because of less energy wasted in producing heat. The major drawback for a switching amplifier is the noise it introduces into the system.

A switching or PWM amplifier can be configured to operate in four different modes. They are the current mode, the voltage mode, the back EMF mode and the IR compensation mode. Description of each one of them follows.

Current mode: It is also known as torque mode. This is the most common operating mode. It is used with a position controller whereby the amplifier produces a torque output proportional to the reference voltage (command) input.

Voltage mode: It is also known as tach-feedback mode. It is used when a tachometer reading is available. The amplifier compares the tach feedback with the command signal and adjusts the voltage and current output accordingly.

Back EMF mode: This mode of operation is used for velocity control when tach feedback signal is unavailable. The input voltage commands a proportional motor voltage regardless of power supply voltage.

IR compensation mode: It is used for simple speed control. An external circuit commands a DC voltage in response to changes in load.

At the basis of a PWM amplifier is a current control circuit that controls the output current by varying the duty cycle of the output power stage. Figure 2.11 shows the actual voltage output of the PWM amplifier used in this research. The voltage output of the PWM amplifier has “On” and “Off” stages. In the “On” stage, the voltage output is 160 volt. In the “Off” stage, the voltage is zero. By varying the “On” stage duration, current output can be adjusted. The difference between the current demanded and the actual output current determines the switch “On” time. The switching frequency of a PWM amplifier was preset by the manufacturer to be as high as 20 kHz, so that it had the minimum current ripple and audible noise. In this research, PWM amplifiers operated in the current mode were used to power the base, shoulder and wrist joints. At the heart of current mode, the amplifier circuitry can be shown in Figure 2.12. The equivalent block diagram of the current mode is shown in Figure 2.13.

At this stage, we don't really know the dynamics contributed by the PWM, control logic and the current sensor block as shown in Figure 2.13. To investigate the effect, we connected the amplifier to a servomotor and performed an experiment. The block diagram representing the amplifier-servomotor dynamics is shown in Figure 2.14.

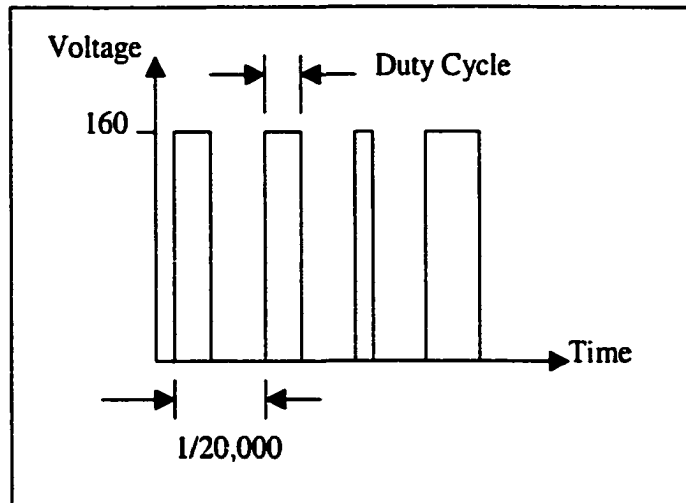


Figure 2.11: PWM voltage output [42]

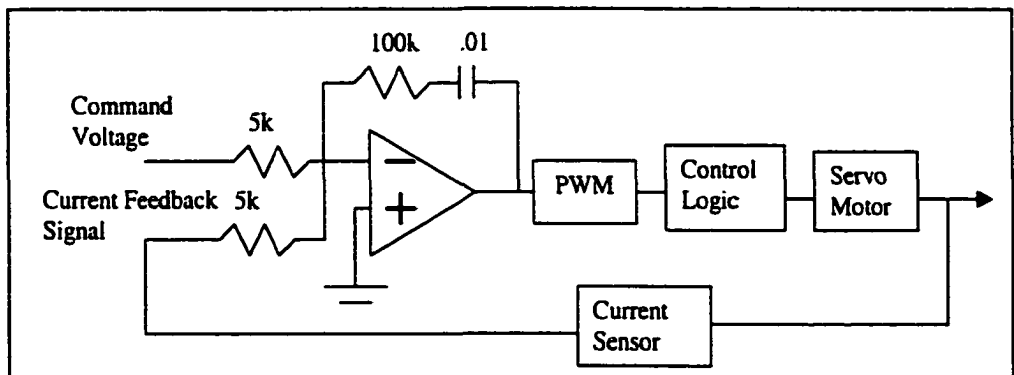


Figure 2.12: Circuit diagram of current mode. [43]

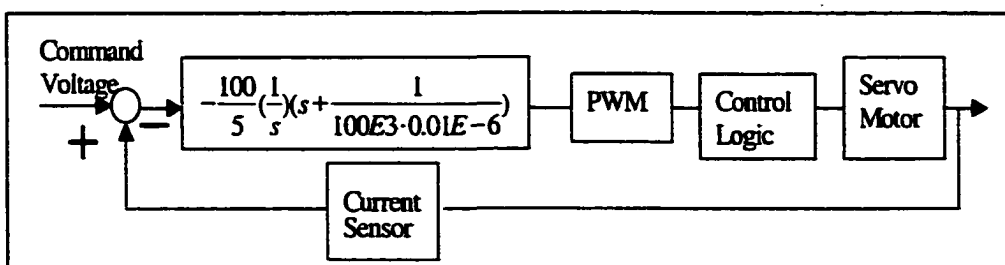


Figure 2.13: Equivalent block diagram of a PWM amplifier in current mode.

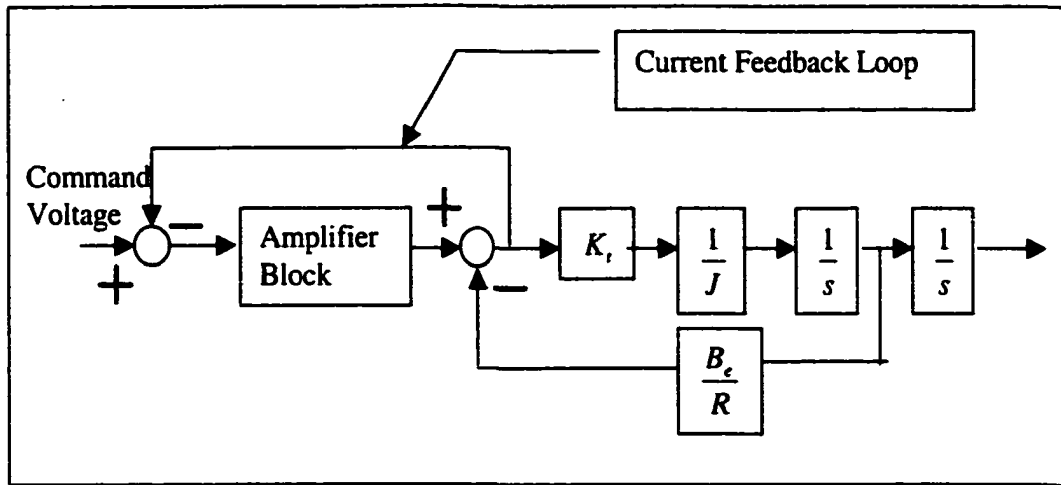


Figure 2.14: Experiment for identifying amplifier dynamics.

The servomotor used in this experiment had a torque constant K_t of 1.41 lb-in/amp, a back EMF constant B_e of 0.1594 V-sec/rad, an armature resistance R of 1.8Ω and a rotor inertia J of 0.00163 lb-in-sec². A step command voltage was applied to the system. The response of the servomotor was observed by an optical encoder. The reading from the encoder was collected at 1000 Hz in a data acquisition board. A first time-derivative was taken on the data collected and it is shown in Figure 2.15.

There are several observations can be made in Figure 2.15. First, the motor spins up at a constant acceleration until it hits the maximum velocity, and the acceleration depends on the magnitude of the command voltage. Second, there is no noticeable transient at the beginning of the response curve. From these observations, we can draw two important conclusions from this experiment.

Conclusion 1: The dynamics contributed by the amplifier is negligible compared to the servomotor dynamics. There is not any obvious transient even if we zoom in the data

closely. The transient response is simply too fast for the data acquisition board to capture. Practically, we can treat the servo amplifier as a pure gain element in the dynamic modeling as long as it is operated in the linear range.

Conclusion 2: A closer look at Figure 2.15 reveals that the velocity profile follows a “ramp” curve instead of a typical first order system response curve. As a reminder, an open loop dc motor is a first order system in the velocity domain. It suggests that the influence of the back emf has been eliminated by the amplifier.

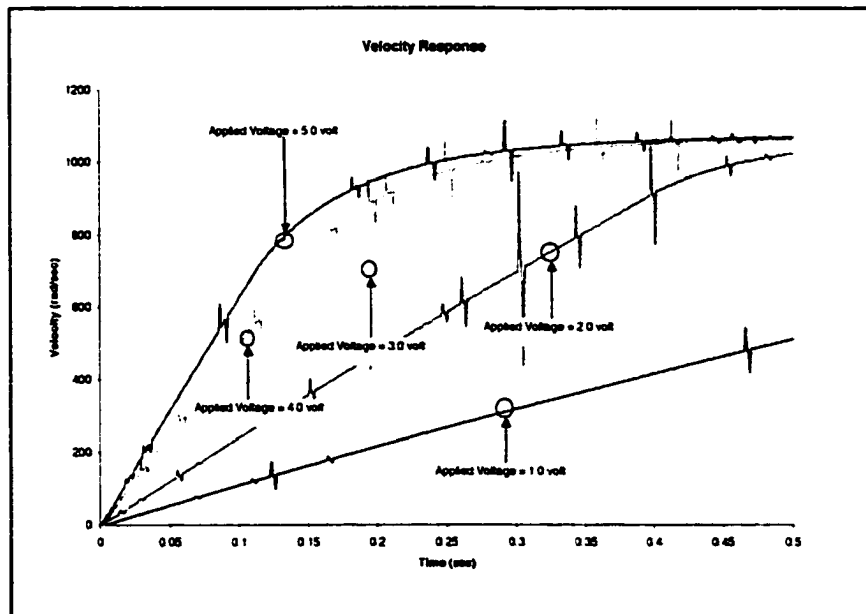


Figure 2.15: Velocity response of an amplifier-servomotor system to a step voltage command.

Based on the conclusions, the amplifier will be treated as a current source that outputs current proportional to the command voltage instantaneously. Therefore, the dynamics of an amplifier-servomotor system can be modeled as shown in Figure 2.16. Note that in Figure 2.16, we exclude the motor damping based on conclusion 1. In fact, the motor damping force

is small compared to the external damping force. In the controller design section, we will again bring in the motor damping into formulation and do a further investigation of its effect on system dynamics. Using the same procedures, the amplifiers for the base, linear and wrist joints were identified. The command voltage and the actual output current were plotted against each other as shown in Figure 2.17. All of the amplifiers used in this research have a current limit of about 9.0 amp. As one can see from the figure, the gains for all of them are about the same at 1.0 amp/volt.

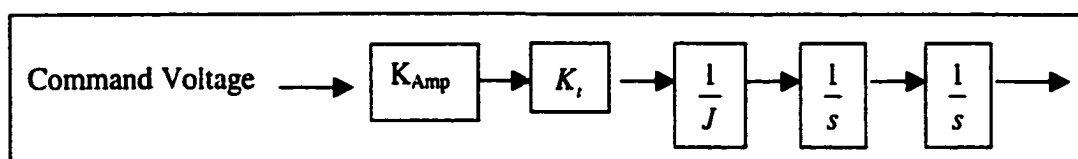


Figure 2.16: Simplified servomotor + amplifier system block diagram.

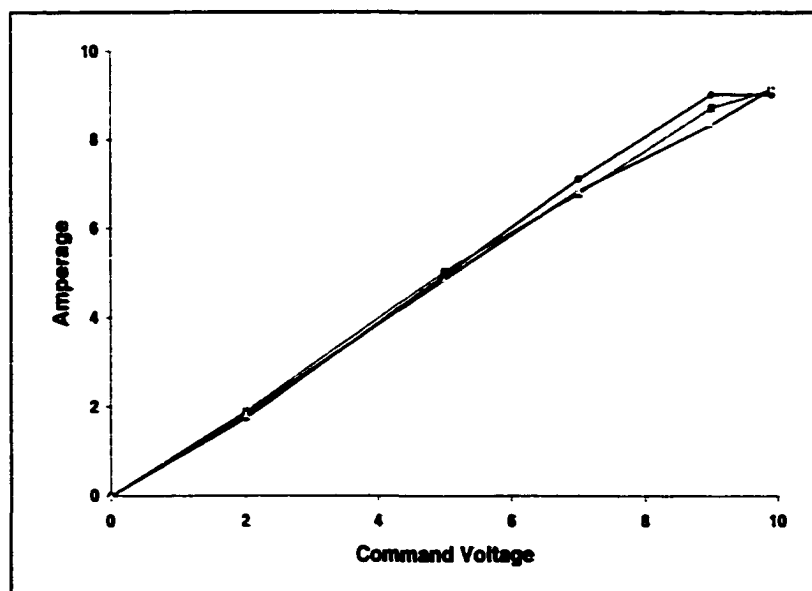


Figure 2.17: Amplifier gains of base, linear and wrist joints.

The system shown in Figure 2.16 is only marginally stable if we close the positional feedback loop since there are two poles at the origin. Ideally, two zeros can be placed as to cancel the effects of the poles so that we get a flat frequency-response function in every frequency. However, implementation of zeros requires taking numerical derivatives of the raw data explicitly. A numerical derivative, that has a slope of 20 dB/decade in the frequency domain, amplifies noise in the high frequency range.

Controller Design

Consider a double pole system shown in Figure 2.18. Closing the positional feedback loop with a unity controller, the closed loop poles lie on the imaginary axis. A PD or a lead controller can stabilize this system. A PD controller introduces a zero into the system and it can be written as $K_p + K_d s$, or $K_d (s + \frac{K_p}{K_d})$. The frequency response function (FRF) of the controller has a slope of 20 dB/decade after the cutoff frequency at $\frac{K_p}{K_d}$ rad/sec. The controller will amplify noise if the noise is above $\frac{K_p}{K_d}$ rad/sec.

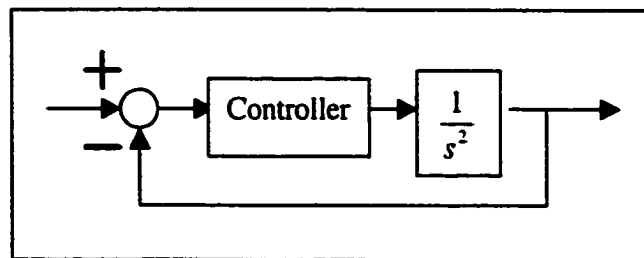


Figure 2.18: Controller design for a double pole system.

The closed loop transfer function shown in Figure 2.18 with a PD controller is

$$\frac{K_p + K_d s}{s^2 + K_d s + K_p}.$$

From the closed-loop system transfer-function, we see that the closed loop

poles can be adjusted by choosing appropriate control gains. However, implementation of a PD controller requires taking a numerical derivative on the raw data explicitly. Depending

upon the frequency of the noise in the raw data, the cutoff frequency, $\frac{K_p}{K_d}$, must be chosen to avoid amplifying the noise excessively. Therefore, there is a limit on how large the derivative gain, K_d , can be in a PD controller design.

To avoid taking numerical derivatives on the raw data, a lead controller provides another way to stabilize the system. The major distinction between a lead and a PD controller is that the lead controller introduces a pole and a zero into the system. A lead controller has the form $\frac{s+a}{s+b}$, where “a” and “b” represent the locations of the zero and pole in “S” plane. Figure 2.19 compares the FRF of a PD to the FRF of a lead controller. As shown in Figure 2.19, both of the controllers have a slope of 20 dB/decade after the first cutoff frequency at “a” rad/sec. The FRF of the lead controller will turn flat after “b” rad/sec, whereas the PD controller keeps increasing at a rate of 20 dB/decade. The lead controller will still magnify any signal and noise when they are above “b” rad/sec, but not as much as the PD controller.

A double pole system with a lead controller has a root locus as shown in Figure 2.20. What is the advantage of introducing a pole then? Consider a simple lead controller as shown in Figure 2.21. In Figure 2.21, the one on the left is a lead controller expressed in the continuous time domain and the one on the right is the approximation of the controller

expressed in the discrete time domain. The discrete time approximation shown is derived based on a backward derivative formula, $\frac{1-Z^{-1}}{dt}$. Z^{-1} is a time delay operator, and dt is the controlling period. Note that there are numerous numerical derivative schemes can be utilized to approximate the controller.

From the discrete time representation of the lead controller shown in Figure 2.21, the output variable Y can be written as

$$Y = \frac{KX(1+a \cdot dt) + Y_{old} - KX_{old}}{1+b \cdot dt} \quad (2.26)$$

From Eq (2.26), we see that no explicit numerical derivative is taken on the input variable “X”. As far as taking a numerical differentiation on the raw data is concern, the zero introduced by a lead controller is subjected to less restriction on where it can be compared to a zero introduced by a PD controller.

The next question is “how do we choose the locations of the pole and zero for a lead controller?” Theoretically, we should place the controller pole as far out to the left half plane as possible so that it has a minimum effect on the system dynamics. As a side note, a PD controller places a zero at K_p/K_d and a pole at negative infinity. Choosing the controller pole is subjected to two restrictions. First, the system is controlled discretely using a digital computer; there is a limit on how far the pole can be placed without inducing instability. Any closed loop pole that lies outside the Nyquist frequency limit causes instability. As a basic rule, one needs at least 10 data points to recover a cycle of motion without excessive distortion of the wave form. Second, as shown in Figure 2.19, a lead controller still magnifies signal and noise above “b” rad/sec. Therefore, the frequency of the noise is still a

major concern in choosing the location of pole. In the experimental results presented below, the system was controlled at 300 Hz. We chose to place the pole at 15 Hz. A 15 Hz controlling frequency was approximately equal to -94 in the “S” plane.

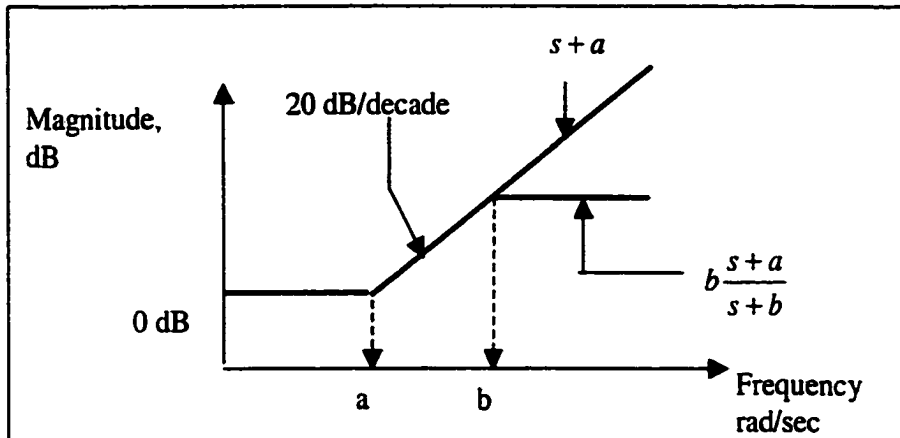


Figure 2.19: Comparison of FRF of a PD and a lead controller.

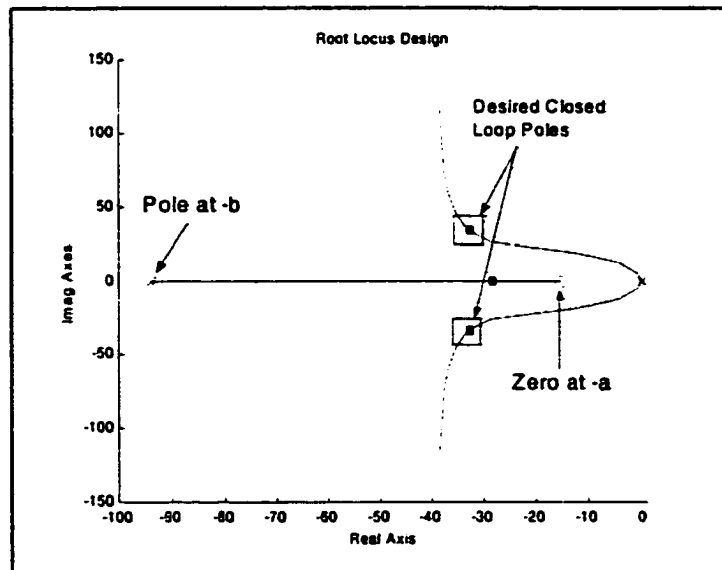


Figure 2.20: A lead controller design.

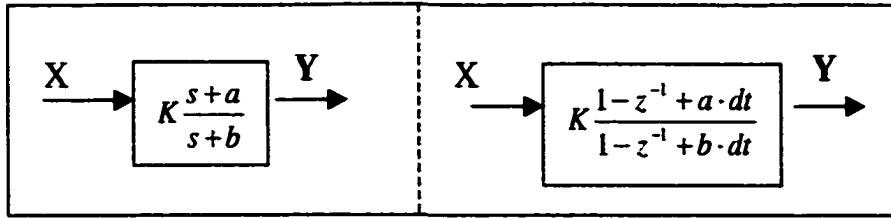


Figure 2.21: Representation of a lead controller in continuous and discrete time domain.

To choose the zero location for the controller, we needed to decide the locations of the closed-loop poles. In this experiment, the closed-loop poles were chosen so that the system had a natural frequency of 7.5 Hz with a damping ratio of 0.707. A system natural frequency of 7.5 Hz and a damping ratio of 0.707 were corresponding to $-33.3 \pm 33.3i$ in the “S” plane. Figure 2.20 shows the desired closed-loop poles and the controller pole and zero.

Figure 2.22 shows the location of desired closed-loop pole and its relationship to the open-loop poles and zero. Using the angular criteria, angular contribution by the controller zero was

$$\theta_z - \theta_{p1} - \theta_{p2} - \theta_{p3} = -180^\circ$$

$$\theta_z = \theta_{p1} + \theta_{p2} + \theta_{p3} - 180^\circ = 118.75^\circ$$

Based on the angular contribution, the location of zero was found to be at -15.6 . The magnitude criteria allowed us to find out the overall gain, and it was calculated as followed.

$$\frac{K|s+a|}{|s+b| \cdot |s| \cdot |s|} = 1.0$$

$$\Rightarrow K = \frac{|s+b| \cdot |s| \cdot |s|}{|s+a|} = \frac{(15\pi)^2 \cdot 69.23}{37.71} = 4076$$

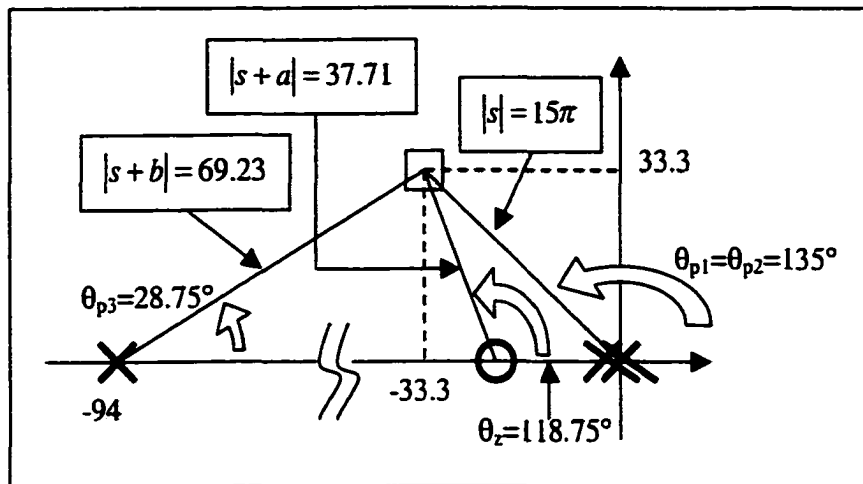


Figure 2.22: Pole zero location of a lead controller.

Experimental Results

In this section, we present some preliminary experimental results of the servomotor-amplifier system with a lead controller. This experiment used an amplifier ($K_{Amp} = 1.50$ amp/volt), a servomotor ($K_t = 1.41$ lbf/amp, $J = 0.00163$ lb-in-sec²), and a lead controller described before, to verify the servomotor-amplifier model derived in the previous section. The control gain, let it be K_{needed} , is calculated as follows.

$$K_{Needed} \cdot K_{Amp} \cdot K_t \cdot J^{-1} = 4076$$

$$K_{Needed} = 3.14$$

The overall system dynamics is shown in Figure 2.23. A step positional command was given to the system. Both the experimental and simulation results were shown in Figure 2.24. Notice that the response curve shown in Figure 2.24 came from a third order system even though it appeared to be a classical step response of a second order system. In this experiment, the step size was limited to 4.0 radians to avoid saturation of the amplifier. In Figure 2.24, the simulation result was superimposed on the experimental result. They agreed

well with each other. We concluded that our modeling of servomotor and amplifier represents their true dynamics. As a side note, this controller is considering the worse possible situation since we assume that there is no damping in the system. In reality, a mechanical system will always have some damping; its effect will be discussed next.

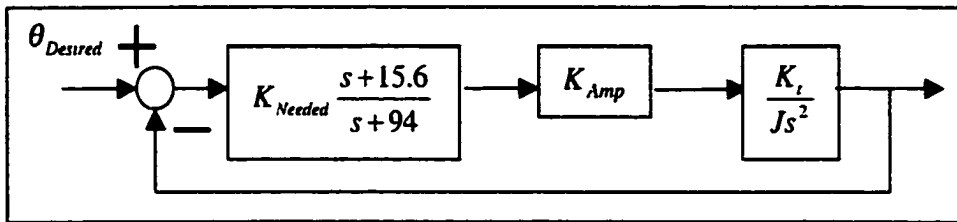


Figure 2.23: Close loop system with a lead controller.

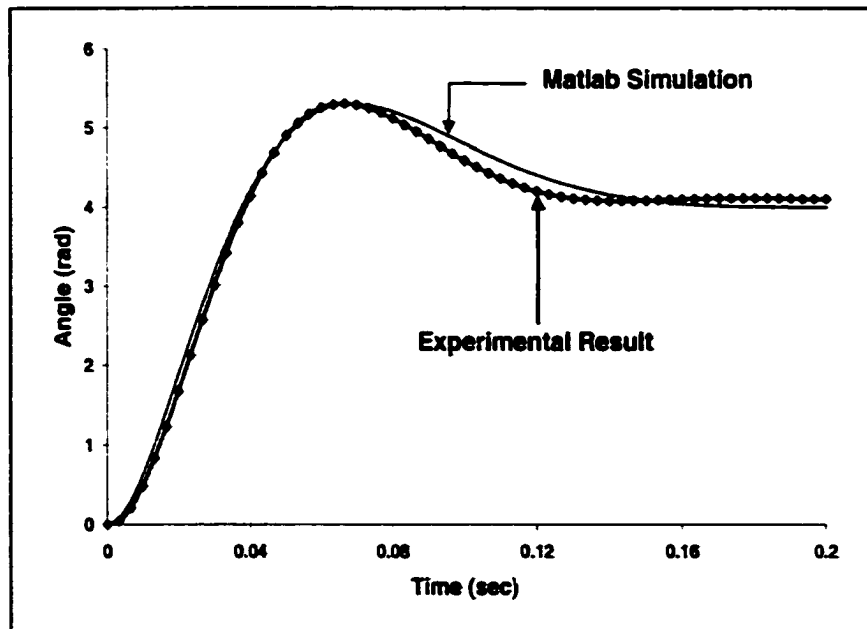


Figure 2.24: Simulation and experimental result of an amplifier-servomotor system response to a step command.

External Inertia and Damping Effects

From the previous section, a good correlation between the experimental and simulation results confirmed the model of servomotor and amplifier. A lead controller was able to stabilize the system by modifying the closed loop poles. Would the controller be stable when the servomotor was connected to an external system? The dynamics of a servomotor, an amplifier and an external system, that has an inertia of J_e and a damping of B_e , can be represented by Figure 2.25.

Block diagram shown in Figure 2.25 can be simplified and shown as Figure 2.26. We observed the following effects introduced by an external system. First, a pole at the origin was driven to $(-\frac{B_e}{J + J_e})$. We see that how far to the left of the new pole was directly proportional to the external damping. Figure 2.27 shows a family of system root loci with different external damping. In the figure, the external inertia, J_e , was assumed to be zero. The effect of external inertia will be elaborated next. From the figure, we see that the external damping pulls the system root locus toward the left half plane and the real axis. Therefore, an **external damping helps improving the system stability**. On the other hand, from the expression of the open loop pole, we see that its location is also a function of the external inertia.

Figure 2.28 shows the effects of external inertia on the system root locus and it was generated based on the ratio of the external and motor inertia. The top left figure is the same as Figure 2.27 and it is generated for reference. The top right figure assumed that the external inertia was one times of the motor inertia. The bottom left and right figures assumed the external inertia to be two and three times of the motor inertia respectively. From the

figures, we see that the effect of inertia overshadowed the damping effect quickly. When the external inertia was large compared to the motor inertia, the pole, as discussed previously, would again be driven back to the origin. In fact, in the machine used for this research, the base joint servomotor, after the gear reduction, had to drive an effective inertia of at least 15 times of its own when the machine was unloaded. From the analysis, we conclude that **external inertia destabilizes the system by driving the open loop pole toward the right half plane**. The worse possibility is that the external inertia gets so large that it overshadows the damping effect.

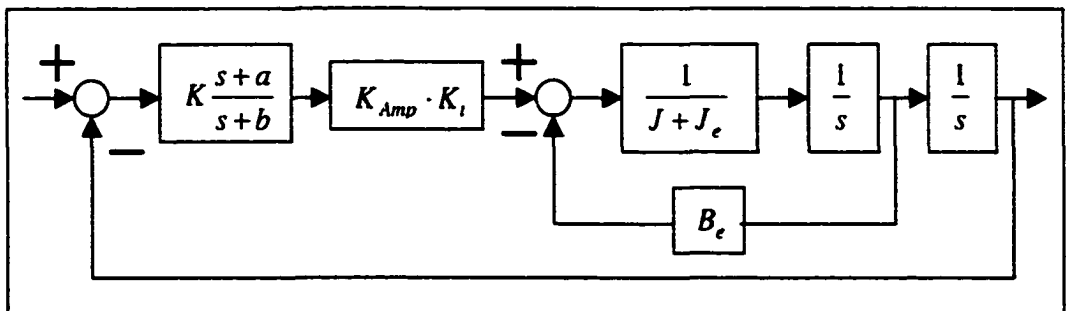


Figure 2.25: Dynamics of a servomotor and an external system.

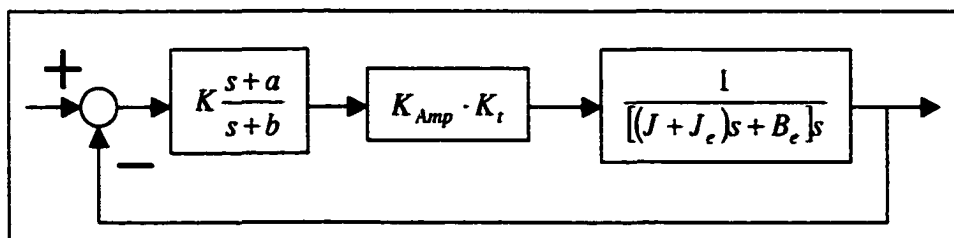


Figure 2.26: System with external damping and inertia.

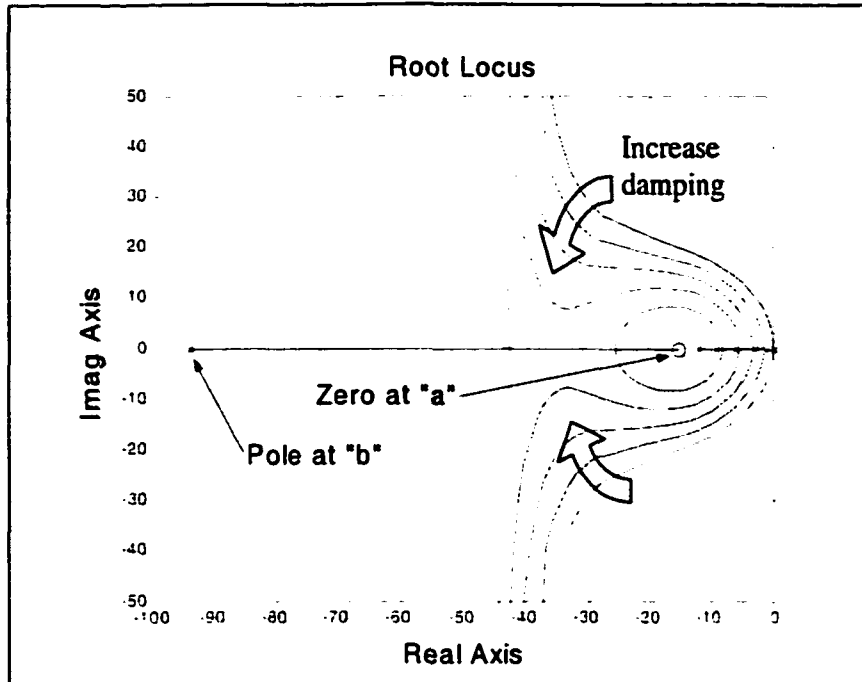


Figure 2.27: Effect of external damping on the system root locus.

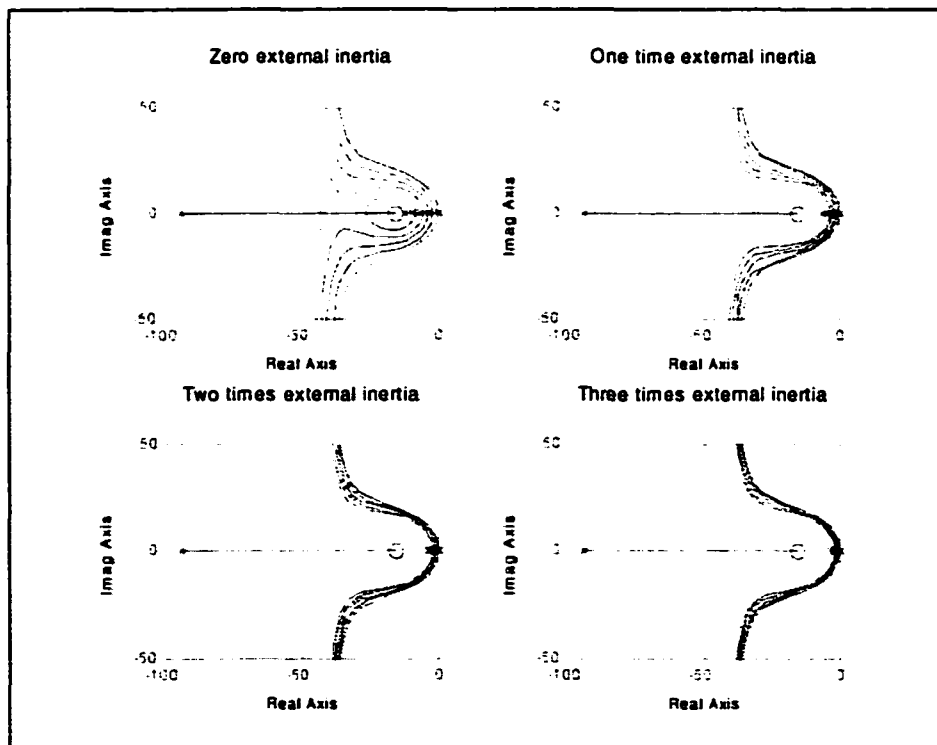


Figure 2.28: Inertia and damping effects on the system root locus.

Figure 2.29 was generated based on the assumption that the damping effect was negligible compared to the inertia effect. As the external inertia increases, the closed loop poles will move toward the origin since the inertia has an inverse relationship with the overall system gain. In order to maintain the closed locations of the loop poles, the overall control gain must be changed according to the variation of inertia. In the controller design, a gain scheduling method was used for the base joint so that the control gain would change according to the machine inertia as shown in Figure 2.9. For the linear actuator, the inertia, as shown in Figure 2.10, appeared to be relatively flat in the middle, the operating region. Therefore, in the controller design, the control gain for the linear actuator was kept at constant. The effects of external damping and inertia can be summarized as follows: (1) External damping increases system stability-margin by pulling an open loop pole toward the stable left half plane. (2) External inertia destabilizes the system by driving an open loop pole toward the origin. (3) External inertia decreases the overall system gain.

Finally, a few words are required on the lead controller. As one can see, with extra damping from the external system, a more stable system will result. As far as damping is concern, the lead controller can only perform better since it is designed for the worse possible case where damping is equal to zero. For the external inertia, the control gain must be adjusted according to the changing inertia so that the closed loop poles will be kept stationary. However, in the worse case, the closed loop poles will be at the origin, and a marginally stable system will result.

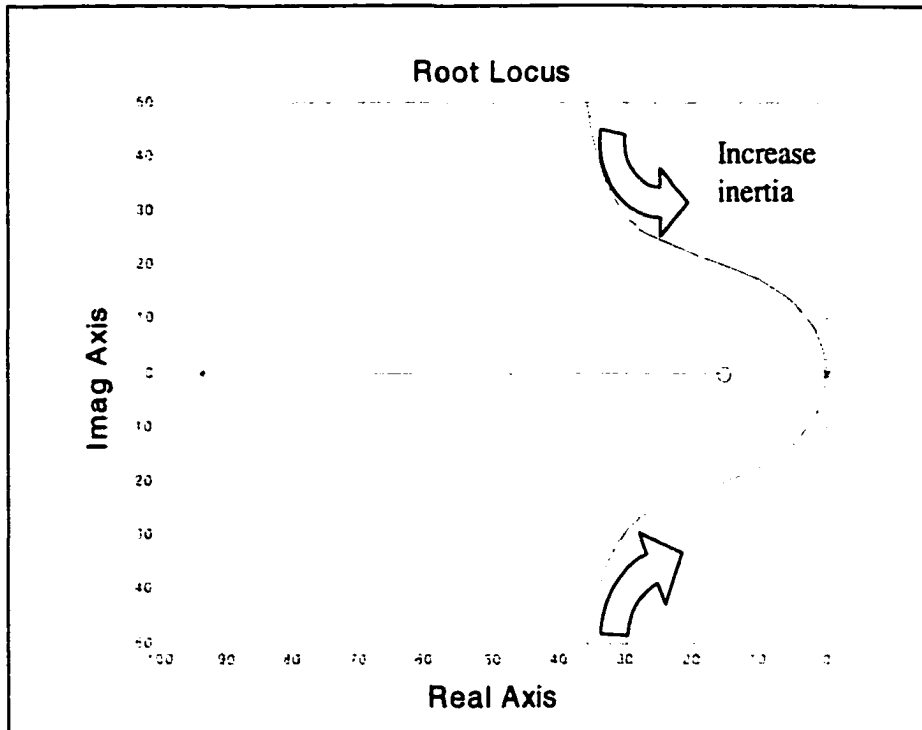


Figure 2.29: Inertia effects on the control gain.

Structural Flexibility

The SAM was originally designed for a manual operation. Structural flexibility might affect the performance of the machine and, sometimes even bring discomfort to the operator, but it did not pose a danger to the safety of the operator. In the original machine, two modes of vibration could be easily excited. They were the torsion mode of the arm and bending mode of the main post. Both of them would cause the out of plane motion at the end effector. Consider a restrained single-degree-of-freedom system shown in Figure 2.30. In the left figure, the notations m , c and k represent the mass, damping and stiffness of the system flexibility. F in the figure represents the input forcing function. k' is the environmental stiffness that the system is coupled to. The equivalent system is represented

on the right figure. The equivalent spring rate k_{equiv} shown on the right figure can be expressed as

$$k_{equiv} = \frac{kk'}{k+k'}$$

The system transfer function can be written as

$$\frac{X}{F} = \frac{1}{ms^2 + cs + k_{equiv}} = \frac{1}{ms^2 + cs + \frac{kk'}{k+k'}} \quad (2.27)$$

If the environmental stiffness, k' , is zero, the system transfer function can be simplified to $\frac{1}{ms^2 + cs}$. We see that the system has two real roots. No oscillatory behavior can be observed on this system. On the other hand, if the environmental stiffness is large, the equivalent stiffness $k_{equiv} \approx k$, the system transfer function becomes $\frac{1}{ms^2 + cs + k}$, which is a typical second order system. This simple example explained two observations we made in the device. First, it was not easy to excite the resonance in the original machine through the base joint because the joint bearing provided a very little resistance to the turning motion. Therefore, the system transfer-function between the input (force) and output (end effector displacement) of the system had two real roots. Second, after the machine was modified and actuators were installed, the resonance of the machine could be excited more easily through the base joint than the machine without the actuators. It was because the servomotor and actuator were more resistive to motion than a base joint bearing alone, which was designed to minimize friction/resistance. In this case, the machine exhibited a typical second-order-system behavior.

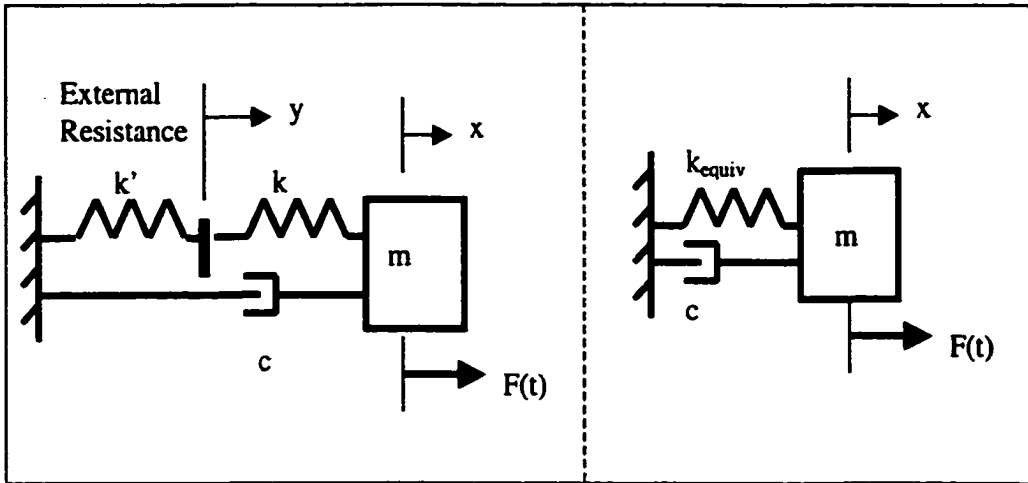


Figure 2.30: A restrained SDOF system.

An open loop transfer function of the base joint servomotor and the machine flexibility can be expressed in Figure 2.31. In Figure 2.31, ω_n is the natural frequency associated with the first vibration mode of the structure, and ξ is the first-mode-damping ratio. In this research, only the first mode of vibration will be considered since it is the principle mode of vibration that is usually excited and it is the principle source of motion errors. As mentioned before, the dominant vibration modes observed on the machine were the torsion mode of the parallelogram linkages and the first bending mode of the main post. Definitely, their natural frequencies and damping ratios were different, and would vary from one machine to the other. From our observation, the torsion mode of the parallelogram linkages was the primary mode that caused the oscillatory motions at the end effector. Therefore, the first mode vibration was referring to the torsion mode of the linkages.

Figure 2.32 shows the root locus diagram of the system, which includes the structural flexibility and the servomotor dynamics, with a unity controller. One can clearly see that the

system is unstable when closing the feedback loop. With a single lead controller as discussed before, it is still possible to stabilize the system by choosing an appropriate system gain. However, depending upon the flexibility of the machine, the poles from the structural flexibility can still dominate the system dynamics. From experiment, it was found that with a single lead controller, the motion of the base joint servomotor would excite the whole structure to be too oscillatory to be useful.

A pole-zero cancellation method was used in this research to make the system less oscillatory. A pair of complex zero, which was close to the structural poles, was implemented as to cancel the dynamics of structural flexibility. The overall system and the controller can be shown in Figure 2.33. In Figure 2.33, $\hat{\omega}_n$ and $\hat{\xi}$ are the estimated values of the machine first mode natural frequency and damping ratio. If both of the estimated parameters are close to the actual ones, the dynamics resulting from the structural flexibility will be cancelled by the zeros from the controller. As before, we need to make the system causal by adding a pair of poles at $-b$.

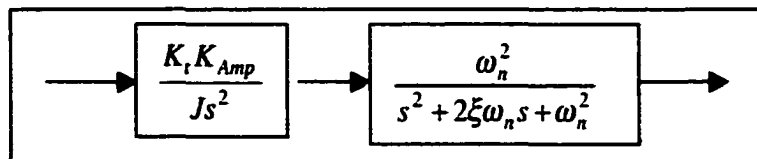


Figure 2.31: Base joint model with structural flexibility.

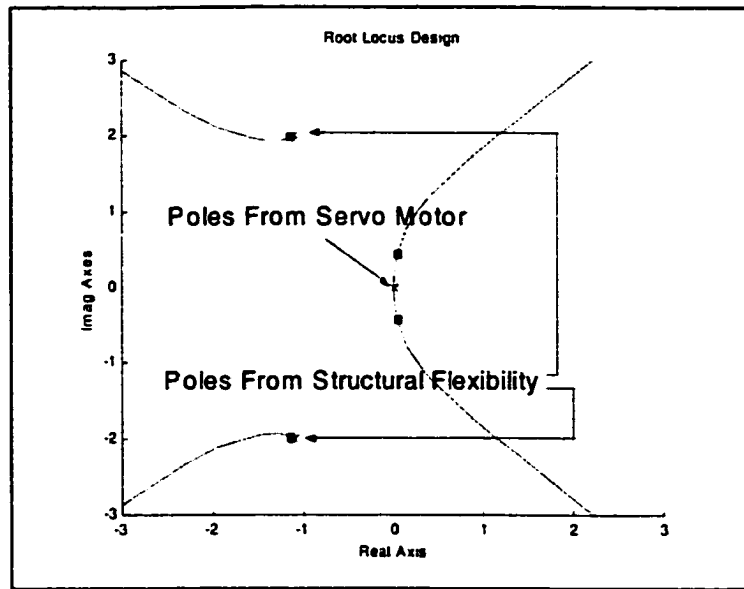


Figure 2.32: Root locus of base joint with structural flexibility.

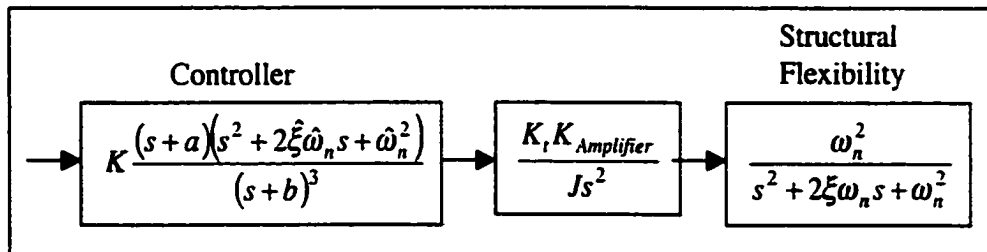


Figure 2.33: Base joint dynamics and controller.

Looking at the structural flexibility compensator, as shown in Figure 2.33, from the frequency domain, it is a filter with a notch at $\hat{\omega}\sqrt{1-\hat{\xi}^2}$ rad/sec. The compensator acts like a dynamic absorber that flattens the FRF of the system, particularly at the frequency where the structural is dynamically weak.

CHAPTER 3 CONTROL APPROACH

In this chapter, the system controller is presented. First, the control law for generating the end effector trajectory will be discussed. Second, a fictitious repulsive force field for collision avoidance will be described. Stability proofs of the repulsive force field will be given. Next, an artificial attractive force field for guiding the end effector moving toward a predefined target will be explained. Stability proof of the attractive force field will be provided.

State Controller

In this research, the desired trajectory of the individual joint was calculated based on the control inputs of the operator. To provide ease of operation, our goal was to design a control system that was as simple and intuitive to the user as possible. We adopted a concept that the end effector should move in a direction of the user-applied force, and that the acceleration of the end effector was proportional to the magnitude of the applied force. A force transducer appeared to be a natural choice for this application. There were force transducers mounted on the handle of the mechanism as shown in Figure 1.6.

The force transducers served two purposes. First, they were used to sense the force inputs from the operator. Second, they were used for transmitting the forces and the moment from the handle to the machine. In Chapter 4, we will show experimentally that the human operator is supplying a significant portion of the motive forces and moment to the system. It is important that the force transducers are able to physically transmit forces and moment to

the machine. In this research, we were controlling only 3 out of a total 4 degrees of freedom of the machine. Our initial implementation of the controller used a 6-axis force/torque transducer that was capable of measuring forces and moments on all three orthogonal axes simultaneously. However, the 6-axis force/torque transducer was replaced by two 2-axis force transducers later due to several reasons. First, two 2-axis force transducers cost less than a 6-axis force/torque transducer. Next, the 6-axis force/torque transducer was not designed for an industry setting. Dusty environment, impacting and overloading of the transducer would seriously shorten the useful life of the sensor. Finally, two 2-axis force transducers could transmit moment to the machine better than a 6-axis force/torque transducer.

The force transducer that was chosen for this research only allowed measurement of forces in two orthogonal axes, therefore two transducers were needed to gather enough information for the controller. Using the force measurements at the input handle allowed for a simple determination of both the desired direction and the required speed of the payload.

The actual target position for the payload is computed as follows

$$\begin{Bmatrix} X_{target} \\ Y_{target} \\ \theta_{target} \end{Bmatrix} = \begin{Bmatrix} X_{current} \\ Y_{current} \\ \theta_{current} \end{Bmatrix} + \begin{Bmatrix} \Delta X_d \\ \Delta Y_d \\ \Delta \theta_d \end{Bmatrix} \quad (3.1)$$

$$\begin{Bmatrix} \Delta X_d \\ \Delta Y_d \\ \Delta \theta_d \end{Bmatrix} = \begin{bmatrix} K_{force} & 0 & 0 \\ 0 & K_{force} & 0 \\ 0 & 0 & K_{moment} \end{bmatrix} \begin{Bmatrix} f_x \\ f_y \\ m_z \end{Bmatrix} \quad (3.2)$$

where K_{force} and K_{moment} are the constant control gains. In this controller design, both the user-applied forces and the motive forces generated by the joint actuators work to move the object. Rewrite Eq (3.1) as

$$\begin{Bmatrix} X_{target} \\ Y_{target} \\ \theta_{target} \end{Bmatrix} - \begin{Bmatrix} X_{current} \\ Y_{current} \\ \theta_{current} \end{Bmatrix} = \begin{Bmatrix} \Delta X_d \\ \Delta Y_d \\ \Delta \theta_d \end{Bmatrix} = \begin{Bmatrix} error_X \\ error_Y \\ error_\theta \end{Bmatrix} \quad (3.3)$$

One can see that Eq (3.2) is the error function used in the error feedback control. Since the error function does not use the positional information explicitly, therefore this is an open loop controller. To generate the desired trajectory, let's look at the Jacobian matrix derived in Chapter 2.

$$\Delta \bar{X} = {}^0 J \cdot \Delta \bar{\theta} \quad (3.4)$$

$${}^0 J = \begin{bmatrix} -s_0 d_2 - l_e s_{03} & c_0 & -l_e s_{03} \\ c_0 d_2 + l_e c_{03} & s_0 & l_e c_{03} \\ 1 & 0 & 1 \end{bmatrix} \quad (3.5)$$

where the leading superscript {0} represents the base frame. The Jacobian matrix shown in Eq (3.5) is the relationship between the end effector space and the joint space. In our formulation, we generate ΔX (Eq (3.2)) by using the force transducer inputs. To find out the corresponding joint angle displacement, we need to write Eq (3.4) as:

$$\Delta \bar{\theta} = {}^0 J^{-1} \cdot \Delta \bar{X} \quad (3.6)$$

In using Eq (3.6), one should pay particular attention to the fact that the force transducer signal was measured with respect to the tool frame, {3}. We need to transform the force measurements to the appropriate frame of reference before using Eq (3.6), which can be expressed as:

$$\Delta \bar{\theta} = {}^0 J^{-1} \cdot \Delta \bar{X}$$

$$\Delta \bar{\theta} = {}^0J^{-1} \begin{bmatrix} K_{force} & 0 & 0 \\ 0 & K_{force} & 0 \\ 0 & 0 & K_{moment} \end{bmatrix} {}^3R \begin{Bmatrix} f_x \\ f_y \\ m_z \end{Bmatrix} \quad (3.7)$$

where 3R is the rotational matrix which transforms the information in frame {3} back to frame {0}.

Repulsive Field for Collision Avoidance

In a cluttered manufacturing environment, collision of heavy lift assist device can occur simply due to the large inertia of the payload and the inertia of the lift device itself that the operator is not able to stop the motion in time. With all the joints powered by actuators, the inertia and friction forces have been partially compensated for in an IAD. Therefore, the operator can move the work piece with less effort. It also implies that the operator tends to move the work piece at a higher speed. Collision can still happen in an IAD. Using a fictitious repulsive force field around the obstacles in the workspace, an addition to the robot joint control law, can be developed that moves the manipulator so as to maximize the distance of the robot to all of the obstacles in the workspace. In this research, we are implementing a repulsive field as a mean of collision avoidance.

A physical fixture or barrier makes its presence known by producing reaction forces when contacted by a work piece. Likewise, a viable virtual fixture must be able to produce reaction forces to prevent work piece penetration. Virtual fixture can be realized by direct actuation or making use of fixed ground to support reaction forces [3]. The later is widely used since it is passive and stable. Direct actuation is used in tele-robotic operation and

haptic interfaces. Direct actuation has been used [4] to implement the dynamic environment with which an operator interacts. The dynamic environment could normally be described by a set of ordinary differential equations with constant parameters. A repulsive force field is very different an ordinary differential equation since the parameter describing the system stiffness is a non-linear function of position. A repulsive wall has been widely implemented in a tele-operated manipulator, but not in an IAD that has a direct physical contact with the human operator. In this work, the primary contribution is the successful implementation of a repulsive “soft” wall and the system stability proof of the repulsive wall algorithm that will be presented in the next section.

The major challenge in implementing an artificial potential field in a fully automated robotic manipulator is that it is possible for the manipulator to get trapped at a local minimum in the field that is at a different location than the desired target. This could result from the addition of the field developed for repulsive wall and the field for the attractive well. For a heavy lift assist device this is not a serious issue, since the operator can always use his strength to pull the manipulator out of a local minima, if necessary, as long as the attractive force from the artificial potential field is within a reasonable magnitude.

A more serious concern when designing a potential force field came from the repulsive wall to prevent collision with obstacles in the workspace. In a fully automated or a remote controlled robotic manipulator, the repulsive wall resisted the motion by canceling the desired position of the robot in the command. Therefore, the repulsive force field might only need to resist the inertia loads of the manipulator. However, with a human physically interacting with the manipulator, eventually the actuators must resist the human applied load. The traditional repulsive wall has an infinite stiffness at the edge of the obstacle [35] to

ensure the end effector can not penetrate it. When an operator pushes against the repulsive wall, depending upon a number of factors such as the magnitude of the applied force, the multiplying factor K_{force} in Eq (3.2) as well as the existing kinetic energy, the end effector can be driven very close to the wall. Because of the repulsive nature of the algorithm, the system stiffness increases as the end effector moves closer to the wall. The system natural frequency, which is directly proportional to the system stiffness, increases accordingly. In the dynamic modeling of servomotor, higher order dynamics such as the motor inductance and the flexibility of the rotor shaft are normally neglected. These effects will play an important role in determining the dynamic behavior of the servomotor if its natural frequency is driven high enough by the repulsive wall. Second order approximation of servomotor dynamics won't be valid and the un-modeled dynamics of the servomotor will destabilize the system. Furthermore, because the system is implemented in a discrete time math using the digital computer, sampling effects come to dominate the stability of the response. The system is controlled at a finite frequency. The sampling theorem imposes a limitation on how stiff the wall can be without causing instability. In the following section, we will investigate and discuss the relationship between the sampling frequency and the stiffness of the wall and provide a new approach on how to avoid the stability problem.

Interaction of the Human Applied Force with the Repulsive Force Field

It was shown in the previous chapter that the differential equation governing the dynamics of a amplifier + servomotor is

$$J\ddot{\theta} = K_t \cdot K_{Amp} \cdot V \quad (3.8)$$

where K_t is the torque constant, J is the mass moment of inertia of rotor, K_{Amp} is the amplifier gain, and V is the command voltage. In the controller design, we are using the classical repulsive field [35] that has the form

$$F_r = \frac{C_r}{(\theta - \theta_r)^3} \quad (3.9)$$

where F_r is the repulsive force, C_r is a constant that controls the shape of the wall, and θ_r is the location of the repulsive wall. As mentioned in Chapter 2, two controllers could be used to stabilize a system with two poles that were very close to the origin. The next question we need to answer is, with the controller, either a PD or lead, will the system be stable if the repulsive force field is added to the existing system? With the human operator in the workspace of the manipulator, he will be in great danger if the overall system is unstable. Therefore, absolute stability of the system is critical. In the following section, stability proofs for the controllers will be provided.

Stability Proof of Repulsive Force Field Implemented by a PD Controller

Figure 3.1 shows the overall system dynamics of a servomotor with a repulsive force field implemented by a PD controller. In Figure 3.1, the environmental stiffness, which might come from the human arm, was modeled as a spring with stiffness K_E . A PD controller was used to stabilize the inner feedback loop. On the feedback path, a repulsive force would be generated based on the position of the motor.

The control law for a PD controller can be written as

$$V = K_p \cdot e + K_d \cdot \dot{e} \quad (3.10)$$

where K_p , K_d are proportional and derivative gains and e is the error function. K_p is used to adjust the responsiveness of the system to the operator-applied force and it has a direct influence on the system natural frequency. K_d , which will be demonstrated later, has a direct influence on the system damping.

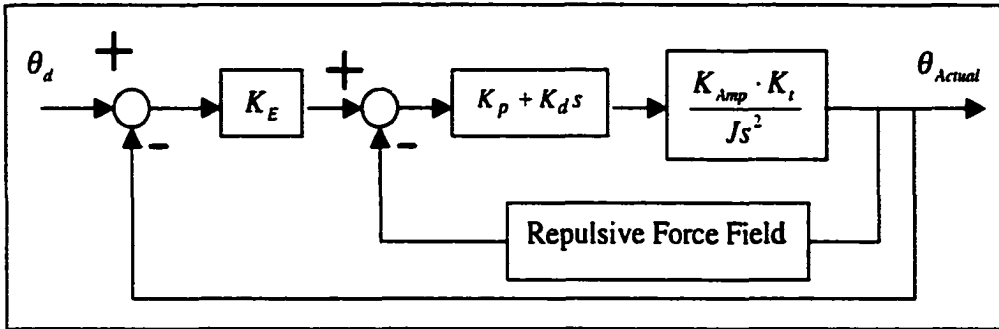


Figure 3.1: A PD controller for implementing repulsive force field

In an error-feedback control system, the plant is driven to minimize the difference between the desired state and the actual state. When designing the error function for the IAD, we are using the fact that the system must move in the direction that it will reduce the total acting force. The total acting force comes from the operator-applied force and the artificial force field. Therefore, the error function can be expressed as

$$e = F_u + F_r = F_u + \frac{C_r}{(\theta - \theta_r)^3} \quad (3.11)$$

where F_u is the user-applied force. Taking a time derivative of Eq (3.11), we get

$$\dot{e} = \frac{-3C_r \dot{\theta}}{(\theta - \theta_r)^4} \quad (3.12)$$

assuming F_u is a constant

The governing equation of the inner loop system can be written as

$$J\ddot{\theta} + \frac{3K_t K_{Amp} K_d C_r}{(\theta - \theta_r)^4} \dot{\theta} - \frac{K_t K_{Amp} K_p C_r}{(\theta - \theta_r)^3} = K_t K_{Amp} K_p F_u \quad (3.13)$$

As one can see on the right hand side of Eq (3.13), the user-applied force is scaled by the product of K_p , K_t and K_{Amp} , and that has a direct influence on the responsiveness of the system to the applied force. Linearizing Eq (3.13) about $\theta = \theta_0, \dot{\theta} = \dot{\theta}_0 = 0$, we get

$$J\Delta\ddot{\theta} + \frac{3K_t K_{Amp} K_d C_r}{(\theta_0 - \theta_r)^4} \Delta\dot{\theta} + \frac{3K_t K_{Amp} K_p C_r}{(\theta_0 - \theta_r)^4} \Delta\theta = 0 \quad (3.14)$$

Looking at Eq (3.14), the system damping is always positive for $K_d > 0$ and $C_r > 0$, and it is increasing as θ_0 approaches θ_r . The system stiffness is positive for $K_p > 0$ and $C_r > 0$. Therefore Eq (3.14) is stable assuming that all other higher order dynamics are negligible. If the outer feedback loop is closed, the overall system will still be stable since the inner loop gives two stable poles. However, we can't be certain where the final poles will lie in the left half plane since K_E , the environment stiffness, as shown in Figure 3.1, is operator dependent. In addition, K_E can be changed easily by the operator. If K_E is high, eventually the close loop poles will lie outside the boundary defined by the Nyquist frequency, and an unstable system will result.

Stability Proof of Repulsive Field Implemented by a Lead Controller

This time we will provide the stability proof of a repulsive force field implemented by a lead controller. As before, the environmental stiffness was modeled as a spring with

stiffness K_E . K_c in Figure 3.2 represents the control gain. The repulsive force field generates a resisting force according to the actual location of the servomotor.

Linearizing F_r of Eq (3.9) about $\theta = \theta_0 + \Delta\theta$, we get

$$F_r = \frac{C_r}{(\theta_0 - \theta_r)^3} - \frac{3C_r}{(\theta_0 - \theta_r)^4} \Delta\theta$$

$$F_r = \frac{C_r}{(\theta_0 - \theta_r)^3} - \frac{3C_r}{(\theta_0 - \theta_r)^4} (\theta_{Actual} - \theta_0) \quad (3.15)$$

$$F_r = \frac{C_r}{(\theta_0 - \theta_r)^3} + \frac{3C_r\theta_0}{(\theta_0 - \theta_r)^4} - \frac{3C_r}{(\theta_0 - \theta_r)^4} \theta_{Actual}$$

Notice that the first two terms on the right hand side of F_r expression are simply constants for an arbitrary angle θ_0 . Block diagram can be modified to Figure 3.3.

The transfer function of the inner feedback loop shown in Figure 3.3 can be written as

$$TF = \frac{K_c \left(\frac{s+a}{s+b} \right) \frac{K_{Amp} \cdot K_t}{Js^2}}{1 + K_c \left(\frac{s+a}{s+b} \right) \left(\frac{K_{Amp} \cdot K_t}{Js^2} \right) \left(\frac{3C_r}{(\theta_0 - \theta_r)^4} \right)} \quad (3.16)$$

$$TF = \frac{(\theta_0 - \theta_r)^4 K_c \cdot K_{Amp} \cdot K_t (s+a)}{(\theta_0 - \theta_r)^4 Js^3 + (\theta_0 - \theta_r)^4 Jbs^2 + 3C_r \cdot K_c \cdot K_{Amp} \cdot K_t \cdot s + 3C_r \cdot K_c \cdot K_{Amp} \cdot K_t \cdot a}$$

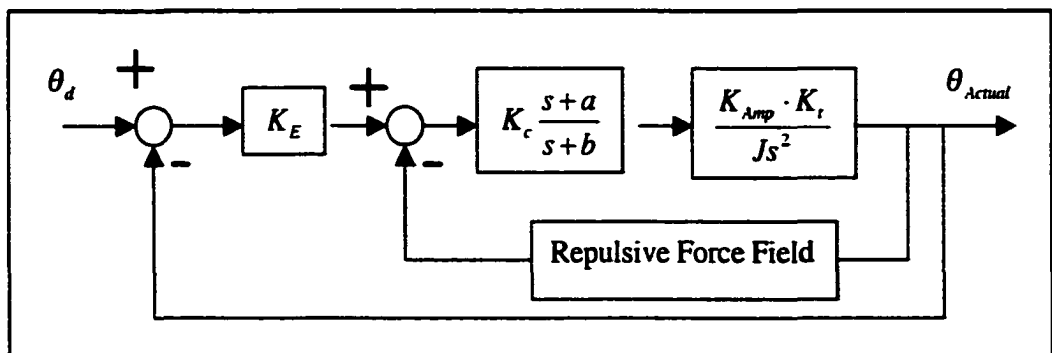


Figure 3.2: Lead controller for implementing repulsive field

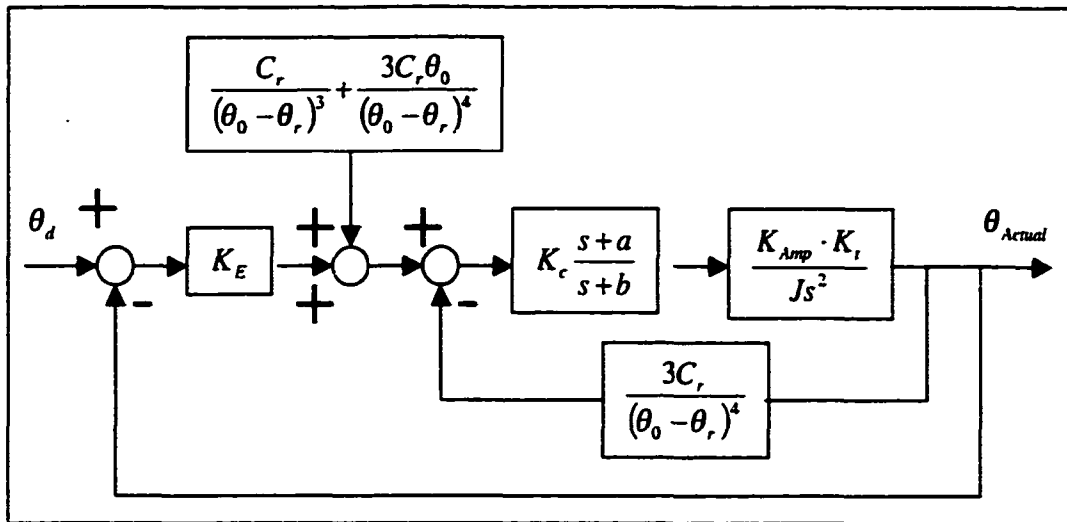


Figure 3.3: Linearized repulsive force field dynamic model.

To investigate the stability, we use Routh-Hurwitz Criterion. A Routh-Hurwitz table is constructed and shown in Table 3.1. The expression for “A” shown in Table 3.1 is positive since the controller pole “b” is further to the left than the zero, “a”. For “B”, it is positive since “a” is positive. From this, we conclude that the inner loop has 3 stable poles and one stable zero. The next question is: “Do we still have a stable system if we close the outer feedback loop?” By counting the number of pole and zero, we know that the asymptotes will be at 90° and 270° . Since all the poles are in the left half plane, therefore with the outer feedback loop, we still have a stable system. The controller with three stable poles and three stable zeros will modify the resultant root locus slightly different from a single lead controller, but the asymptotes are still at 90° and 270° , and the system is still stable. However, if the structural flexibility is taken into consideration, the stability of the system with the controller can not be guaranteed since the number of finite pole minus the number of

finite zero is 4. The asymptotes for the closed loop root locus are at 45° and 135° . The root locus will eventually break into the unstable right half plane if the loop gain is high enough.

Table 3.1: Routh Table for TF

s^3	$(\theta_0 - \theta_r)^4 J$	$3C_r \cdot K_c \cdot K_{Amp} \cdot K_t$
s^2	$(\theta_0 - \theta_r)^4 Jb$	$3C_r \cdot K_c \cdot K_{Amp} \cdot K_t \cdot a$
s^1	$A = \frac{3C_r \cdot K_c \cdot K_{Amp} \cdot K_t (b-a)}{b}$	0
s^0	$B = 3C_r \cdot K_c \cdot K_{Amp} \cdot K_t \cdot a$	0

Implementation of Repulsive Wall: PD Controller

In the actual implementation of the control system, state $e(t)$ is sampled discretely and reconstructed using a zero order hold. However, the output of a zero order hold is a function of $e(kT)$ only, where $k=0,1,2,\dots$, and T is the sampling period. Hence, many different input signals can result in the same output signal from the zero order hold. Shannon's sampling theorem mentions that a function of time $e(t)$ which contains no frequency components greater than f_0 hertz is uniquely determined by the values of $e(t)$ at any set of sampling points spaced $1/(2f_0)$ seconds apart. Thus, in choosing the controlling frequency for a system, it should be greater than twice the highest frequency component of significant amplitude of the system. For instance, if one controls a system at 500 Hz, the highest natural frequency possible for the system must be strictly less than 250 Hz. However, as a general guide, at least 10 data points are needed to fully capture one cycle of motion and

to avoid major distortion of the waveform. For the PD controller, the system natural frequency can be written as

$$\omega_n^2 = \frac{3K_t K_{Amp} K_p C_r}{J(\theta_0 - \theta_r)^4} \quad (3.17)$$

We can also write the expression for damping ratio as:

$$2\xi\omega_n = \frac{3K_t K_{Amp} K_v C_r}{J(\theta_0 - \theta_r)^4} \quad (3.18)$$

$$\xi = \frac{3K_t K_{Amp} K_v C_r}{2J(\theta_0 - \theta_r)^4 \omega_n}$$

In the actual implementation of this algorithm, it is possible to define a system natural frequency (without violating the sampling theorem) and then solve for θ_0 using Eq (3.17).

$$\theta_0 = \theta_r - \frac{3K_t K_{Amp} K_p C_r}{J\omega_n^2}^{\frac{1}{4}} \quad (3.19)$$

θ_0 from Eq (3.19) tells us the location where the system natural frequency will be equal to the predefined frequency ω_n .

To resolve the stability issue associated with the system natural frequency, we propose to calculate the repulsive force as follows.

- (1) Select a K_p and K_d so that the system has the desired close loop poles when the effect of the repulsive wall is at the minimum.
- (2) Select a desired system natural frequency, ω_n . Use Eq (3.19) to solve for θ_0 .
- (3) Examine the damping ratio, ξ by using Eq (3.18). If the damping ratio is not appropriate, go back to Step (2) and select another natural frequency. Repeat this process until a good combination is achieved.

(4) When $\theta < \theta_0$, the repulsive force is calculated according to the classical repulsive force field formulation, Eq (3.9).

(5) When $\theta > \theta_0$, the repulsive force should have an additional linear spring force that is proportional to the distance from θ_0 . The total repulsive force can be expressed as

$$F_r = \frac{C_r}{(\theta_0 - \theta_r)^3} + \frac{3C_r}{(\theta_0 - \theta_r)^4}(\theta_0 - \theta) \quad (3.20)$$

$\theta > \theta_0$

Figure 3.4 shows the difference between the classical formulation and the modified formulation for a repulsive wall. In the figure, θ_0 was chosen to be at 40 degree. Before reaching 40 degree, the modified formulation was exactly the same as the classical formulation. However, after 40 degree, the repulsive force increased linearly.

Note that Eq (3.12) becomes

$$\dot{e} = \frac{-3C_r\dot{\theta}}{(\theta_0 - \theta_r)^4} \quad (3.21)$$

After modifying the repulsive force function, system dynamics can be expressed as

$$J\ddot{\theta} + \frac{3K_t K_{Amp} K_d C_r}{(\theta - \theta_r)^4} \dot{\theta} - \frac{3K_t K_{Amp} K_p C_r}{(\theta_0 - \theta_r)^4} (\theta_0 - \theta) = K_t K_{Amp} K_p F_u + \frac{K_t K_{Amp} K_p C_r}{(\theta_0 - \theta_r)^3}$$

$$J\ddot{\theta} + \frac{3K_t K_{Amp} K_d C_r}{(\theta - \theta_r)^4} \dot{\theta} + \frac{3K_t K_{Amp} K_p C_r}{(\theta_0 - \theta_r)^4} \theta = K_t K_{Amp} K_p F_u + \frac{K_t K_{Amp} K_p C_r}{(\theta_0 - \theta_r)^3} + \frac{3K_t K_{Amp} K_p C_r}{(\theta_0 - \theta_r)^4} \theta_0$$

$\theta > \theta_0$

(3.22)

Equation (3.13) describes the system dynamics when θ is less than θ_0 and Eq (3.22) is used when θ is more than θ_0 . One can see that with the spring rate modification, Eq (3.22) is still a stable system.

Modified spring rate at $\theta = \theta_0$ also works for the system with a lead control. In proving the system stability for the lead controller, we linearized the feedback spring rate at $\theta = \theta_0$, which is the same as fitting a linear spring at $\theta = \theta_0$. Therefore, the stability proof for a lead controller is not necessary.

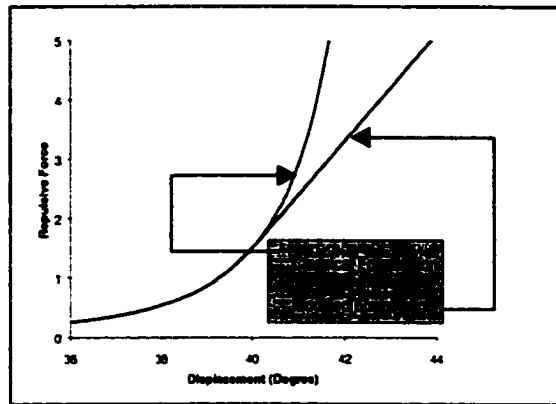


Figure 3.4: Comparison of classical and modified repulsive force field.

Experimental Result: Repulsive Wall with PD Controller

In the experimental result presented below, the servomotor and amplifier have the properties shown in Table 3.2. In the first experiment, we were using a PD controller with $K_p=1.71$, $K_d=0.0514$. With this zero location, we will get a pair of closed loop poles at $-33 \pm 33i$, corresponding to a natural frequency of 7.5 Hz and a 0.707 damping ratio when the repulsive wall is not effective. Figure 3.5 shows the experimental setup. The user applied a constant force to the servomotor. The location of repulsive wall was set to be at 45 degree. The artificial force will have an effect on the system dynamic only if the end effector is close to the wall. In the implementation of the modified repulsive wall, the placement of θ_0 has a

direct influence on the system natural frequency and damping ratio when the repulsive wall takes effect on the system dynamics. In the system used for this experiment, the relationship of natural frequency, damping ratio with respect to the placement of θ_0 is shown in Figure 3.6.

Table 3.2: Servomotor and Amplifier Properties.

Constant	Value
K_t : Torque Const.	1.41 lb-in/amp
K_{Amp} : Amplifier Gain	1.50 amp/volt
J : Mass moment of inertia	0.00163 lb-in-sec ²
C_r : Repulsive Wall Const.	.001

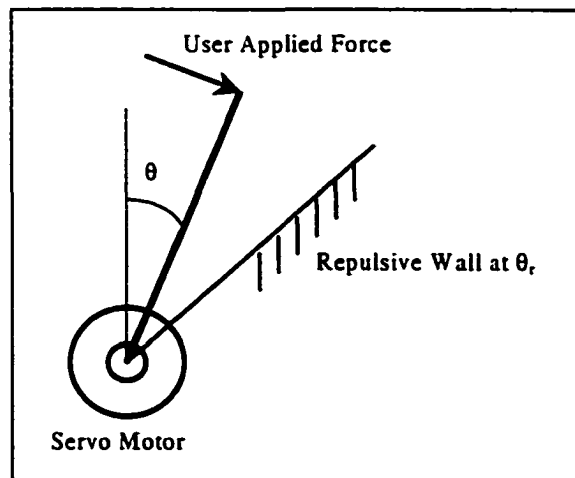


Figure 3.5: Experimental setup.

From Figure 3.6, we see that as the end effector moves closer to the repulsive wall at 45° , system natural frequency and damping ratio increase dramatically. One should be cautious to choose a θ_0 so that the resultant close loop pole won't fall outside the boundary defined by the Nyquist Sampling theorem.

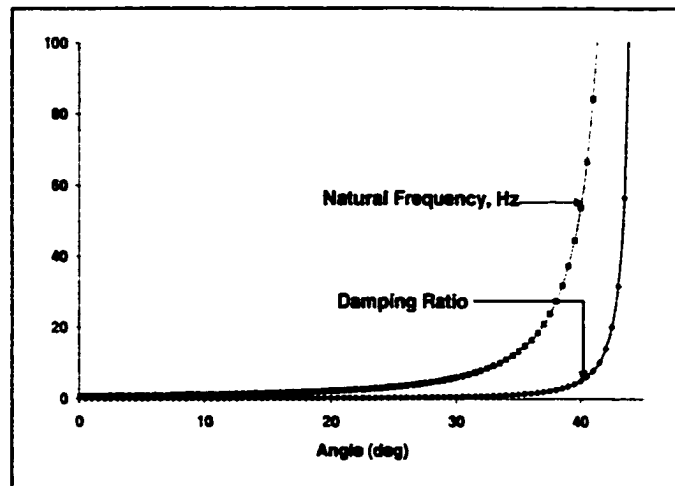


Figure 3.6: System natural frequency & damping ratio

In this experiment, we chose a natural frequency of 10 Hz. From Eq (3.19), the damping ratio was found to be 0.944. Figure 3.7 shows the response of the servomotor to the original and modified repulsive wall formulation when the user-applied torque T_u (Notice that we could only apply a torque to a servomotor) was 0.4 lb-in. Looking at Eq (3.13), one will notice that the user-applied torque is scaled by the factor $K_t K_{Amp} K_p$ of 3.61. Therefore, when the artificial force is absent, there is a constant 1.44 lb-in of torque acting on the servomotor. Figure 3.7 gives us a good idea on the differences between the original and modified repulsive wall. At the beginning of the response curve, we see that both formulations exhibit exactly the same characteristics. As the end effector came closer to the wall, the original formulation pushed the end effector back harder than the modified formulation. Theoretically, both formulations should give a stable response. However, the experimental results show a contradicting conclusion. One can see that the original formulation induced oscillation shortly after the first time the end effector was pushed

backward, and the oscillation was growing as time went by. It might be because the system was driven too close to the wall, resulted in a system natural frequency that was high enough to induce instability in the system. Another possibility would be the current limit on the power amplifier. In the stability analysis, we were assuming that there wasn't any limitation on the current capability of the power amplifier. An important observation we should make on the figure is that the modified formulation allows the end effector to penetrate the wall. Finally, the modified formulation did not induce any oscillation, as predicted by the calculated damping ratio. Figure 3.8 shows that the system with modified repulsive wall response to different user applied torques. All of them show the similar, stable dynamic response to the forcing function.

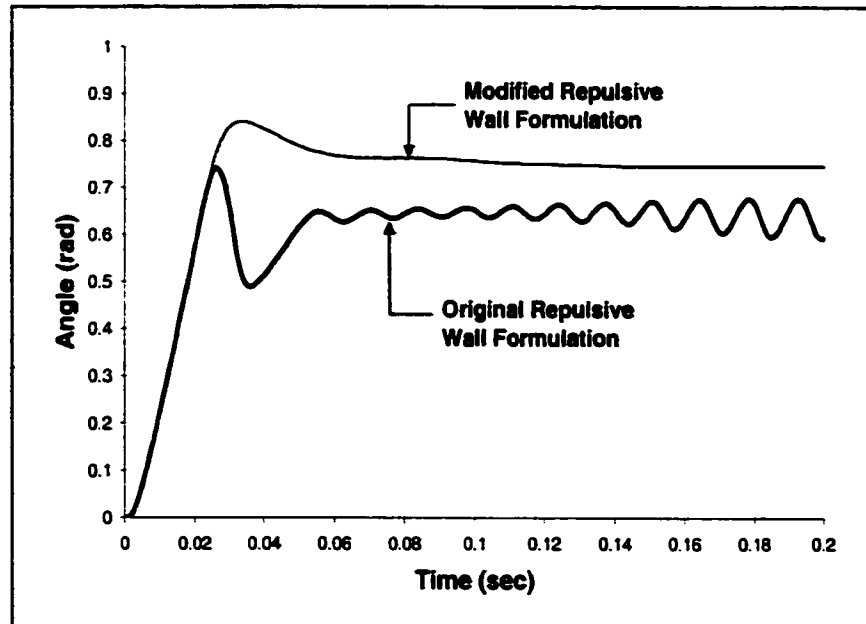


Figure 3.7: System response to the original & modified repulsive wall formulations.

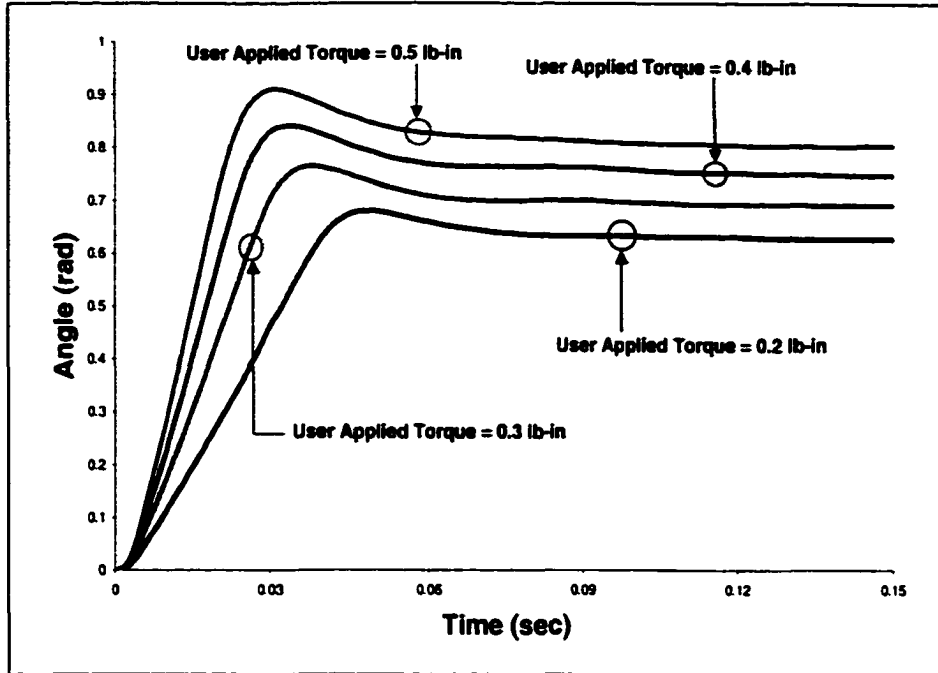


Figure 3.8: System response to different user-applied torques.

Implementation of Repulsive Wall: Lead Controller

Implementation of repulsive wall for the system with a lead controller is not as trivial as the one with a PD controller. Looking at the system transfer function, Eq (16), we realize that we have 3 poles for this system. There are either three real poles or one real pole and one pair of complex poles. Rewrite Eq (3.16) as

$$TF = \frac{K_c \cdot K_{Amp} \cdot K_t (s + a)}{Js^3 + Js^2 + \frac{3C_r \cdot K_c \cdot K_{Amp} \cdot K_t}{(\theta_0 - \theta_r)^4} s + \frac{3C_r \cdot K_c \cdot K_{Amp} \cdot K_t \cdot a}{(\theta_0 - \theta_r)^4}} \quad (3.23)$$

We see that the location of poles strongly depends on $(\theta_0 - \theta_r)^4$.

Using the same servomotor, amplifier, the lead controller $(3.14 \frac{s+15.6}{s+94})$ developed in Chapter 2, and the repulsive wall at 45° , the roots of the system characteristic equation is shown in Figure 3.9.

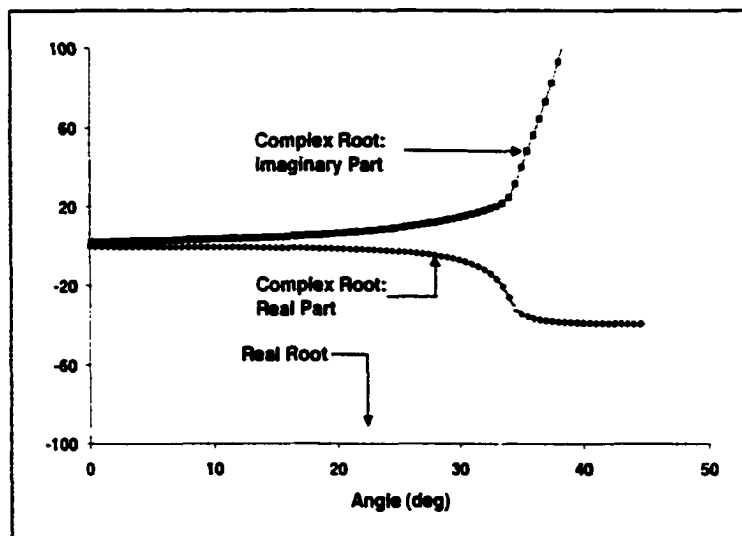


Figure 3.9: Roots of CE

When the end effector is far from the repulsive wall, which is at 45° , one can see that the real root is close to -94 , the pole introduced by the controller, whereas the complex roots are close to zero. However, as the end effector moves closer to the repulsive wall, the real root is getting closer toward the controller zero, which is at -15.6 . From the stability proof, we know that the system will always be stable since the poles will always stay on the left half plane. Indeed, on Figure 3.9, it shows us that both the real root and the real part of complex roots converge to a negative number. However, a more serious concern when designing the repulsive field with a lead controller comes from the magnitude of the imaginary part of the system roots. One can see that the imaginary part diverges very quickly

as the end effector approaches the wall. Figure 3.10 shows the magnitude of the complex poles. System natural frequency is defined by the magnitude of the poles. As the end effector comes close to the repulsive wall, the system natural frequency grows rather quickly and it poses a challenge to the Nyquist stability criterion. We can still use the general guideline established for designing the system controller, let the maximum natural frequency of the system to be at 1/20 of the sampling frequency (-94 in the “s” plane). In this case, it corresponds to about 37°. At this location, the complex close loop poles are $-37.5 \pm 73.5i$ and the real pole is -18.8.

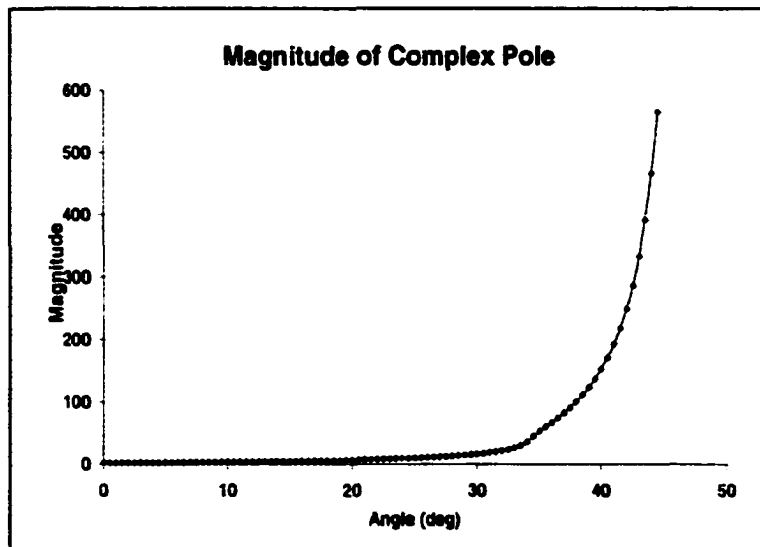


Figure 3.10: Magnitude of complex solutions

Experimental Result

Figure 3.11 shows the system response to the original repulsive wall formulation. The experimental result shows that the system will be stable when the user-applied force is less than 0.45 lb-in. An unstable system results for a moment larger than 0.45 lb-in. The

magnitude of moment might not be significant since it is dependent on the controller and properties of the system. However, it tells us that there is a limit where system will be stable. Therefore, with the original formulation, stability cannot be guaranteed.

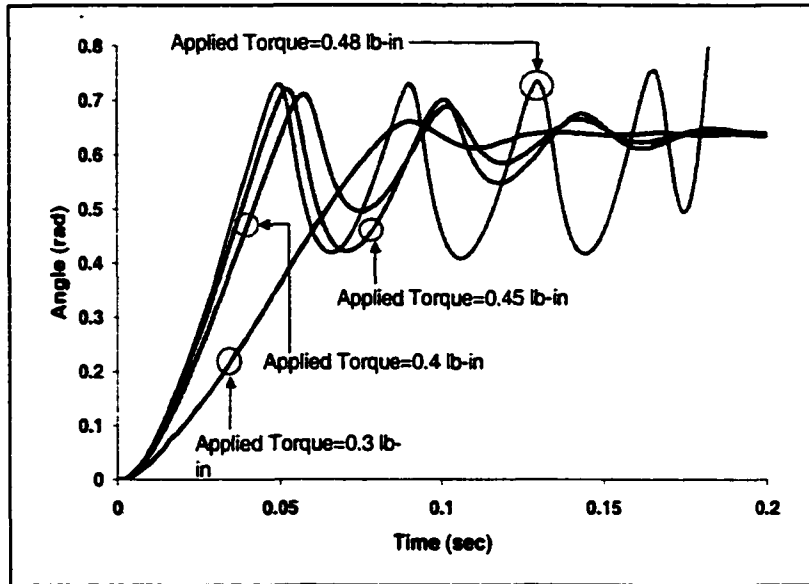


Figure 3.11: Original repulsive wall formulation: lead controller

Figure 3.12 shows the system response to the modified repulsive wall. We made several observations on this figure. First, all of them remain stable regardless of the applied torque. Secondly, they all have the same natural frequency of about 25 Hz. The significance of this frequency still needs further investigation. Finally, the system oscillation dies out.

Figure 3.13 further compares the differences between the original and the modified formulation for the repulsive wall. Indeed they follow the same response at the beginning. As soon as the end effector was close to the wall, the modified formulation reacts with a more gradual and favorable response.

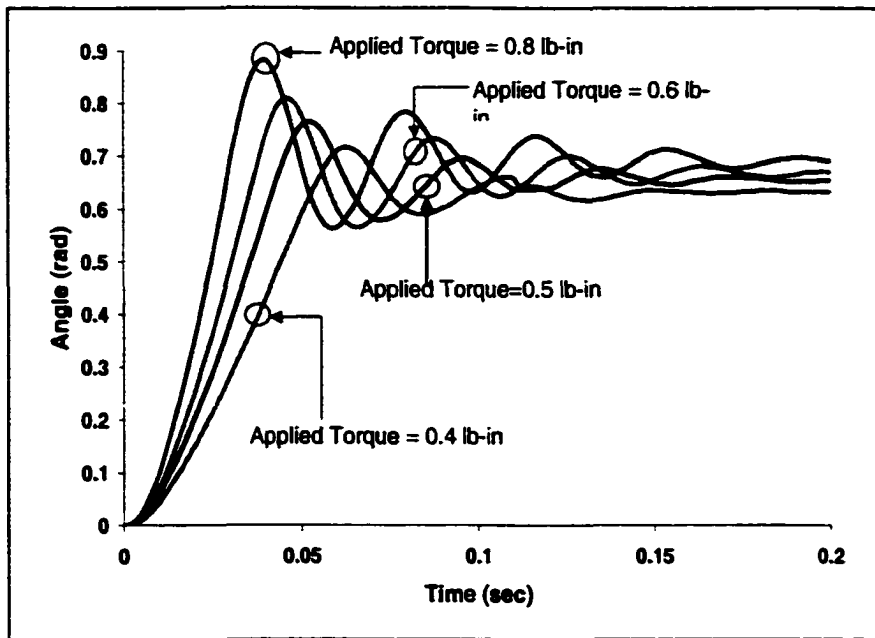


Figure 3.12: Modified repulsive wall: lead controller

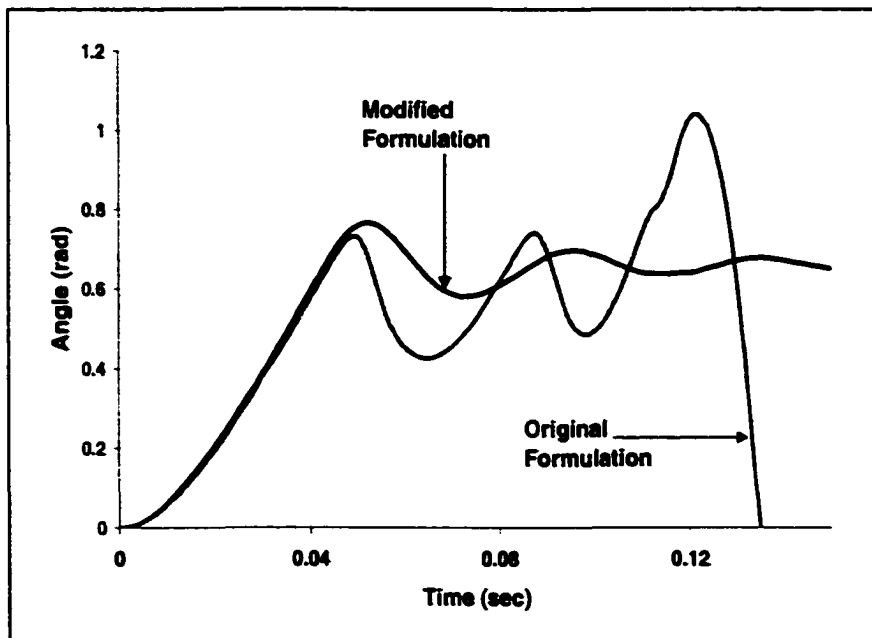


Figure 3.13: Comparison of the original and modified repulsive wall formulation

Attractive Force Field Formulation

An attractive force field is designed to guide the operator to move the work piece in a preferred way and orientation toward a target, which might be important in certain assembly process. An artificial force field takes the following form.

$$F_a = -c_a \cdot (\theta - \theta_a)^{2DN+1} e^{-(\theta - \theta_a)^2 N},$$

$$c_a = \eta_a \left(\left(\frac{2DN+1}{2N} \right)^{DN+0.5} e^{-\left(\frac{2DN+1}{2} \right)} \right)^{-1} \quad (3.24)$$

In Eq (3.24), θ_a is the location of the target point. η_a controls the magnitude of the attractive force. D controls the distance between the peaks of the attractive force, and N will have an effect on the sharpness of the peaks.

Figure 3.14 shows the shape of an attractive force field. In the figure, the target point is located at 0.0. When the state approaches the target point from the negative end, the positive attractive force pulls it moving toward the target. Once the state is at the target point, the attractive force is zero. If it keeps moving in the positive direction, the artificial force will push it back to the target point shown as the negative force in the figure.

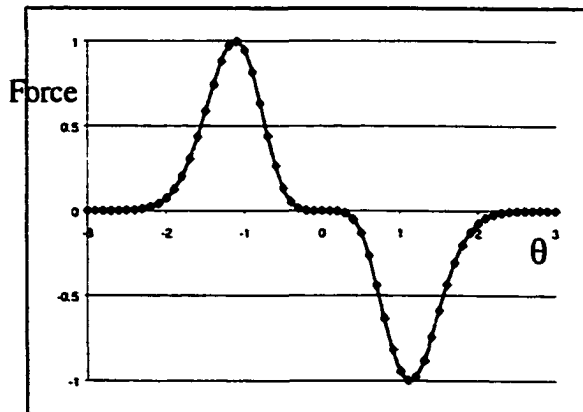


Figure 3.14: A typical attractive force field.

Stability Analysis of Attractive Force Field: PD Controller

We will provide the stability proof of an attractive force field using a PD controller.

The error function can be written as:

$$\begin{aligned}
 error &= F_u + F_a \\
 error\dot &= \dot{F}_a \\
 &= \frac{-c_a(\theta - \theta_a)^{2DN} [2DN + 1 - 2(\theta - \theta_a)^2 N] \dot{\theta}}{e^{(\theta - \theta_a)^2 N}}
 \end{aligned} \tag{3.25}$$

assuming F_u is constant.

The differential Equation describing the dynamics of the servomotor and the controller is:

$$J\ddot{\theta} + \frac{K_t K_{amp} K_d c_a (\theta - \theta_a)^{2DN} \{2(\theta - \theta_a)^2 N - 2DN - 1\}}{e^{(\theta - \theta_a)^2 N}} \dot{\theta} + \frac{K_t K_{amp} K_p c_a (\theta - \theta_a)^{2DN+1}}{e^{(\theta - \theta_a)^2 N}} = K_t K_{amp} K_p F_a \tag{3.26}$$

Without the user-applied force, one can see that the equilibrium point, i.e., all the derivatives of the state vector are identically zero, is at $\theta = \theta_a$, and it is unique in the entire vector space. However, this is not a stable equilibrium point because both damping and spring force are equal to zero at this point. Let θ_a be zero, the system stiffness term can be written as

$$\frac{K_t K_{amp} K_p c_a (\theta)^{2DN}}{e^{(\theta)^2 N}} \tag{3.27}$$

One can see that the system stiffness is symmetric about the equilibrium point. From negative infinity to positive infinity, the work done by the spring force on the system is equal to zero. Therefore, in the stability analysis, the effect from this nonlinear spring can be excluded.

Figure 3.15 shows the damping coefficient of Eq (3.26). The system damping coefficient changes from negative to positive as θ goes from $-\infty$ to θ_a . Let's look at the total work done by the system damper when K_d , C_a and velocity are unity. Assuming velocity to be constant can be justified by the fact that the state will have a higher velocity when it is inside the region where damping coefficient is positive than in the region where damping is negative.

Figure 3.16 shows the spring force and damping force (by assuming unity velocity) as the end effector moves toward the equilibrium point. When the end effector approaches the equilibrium point from Region A as shown Figure 3.16, under the influence of the spring force and the damping force, the end effector accelerates moving toward the equilibrium. As soon as the end effector enters Region B in the same figure, the damping force works against the motion of the end effector. However, spring force is still pulling the end effector toward the equilibrium. From Figure 3.16, one can conclude that the velocity of the end effector is building up in Region A. The velocity of the end effector reaches a maximum in the region B. It implies that the average velocity in Region B is larger than the average velocity in Region A. Keep in mind that in Region A, the negative damping coefficient adds energy into the system. However, because of the lower average velocity in Region A, the energy added in this region due to the negative damping coefficient will be smaller than the energy dissipated by the damping in Region B. Figure 3.17 shows the simulation results where the velocity, damping and spring force were plotted on the same graph. Indeed, one can see that the velocity reaches a maximum in Region B, where the damping force resists the motion. To be conservative in the analysis, we assume that the average velocity for both of the regions to be the same and investigate the work done by the system damper.

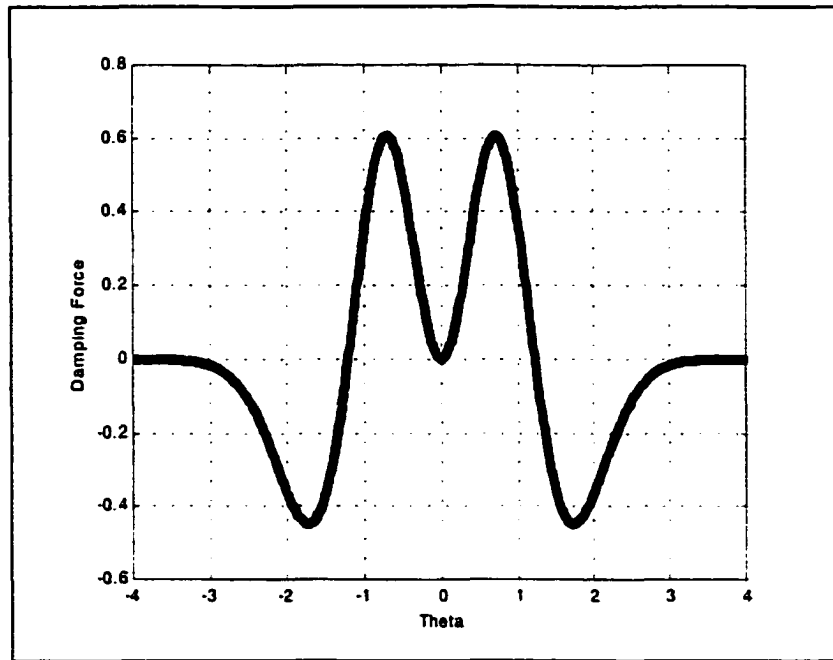


Figure 3.15: Damping coefficient.

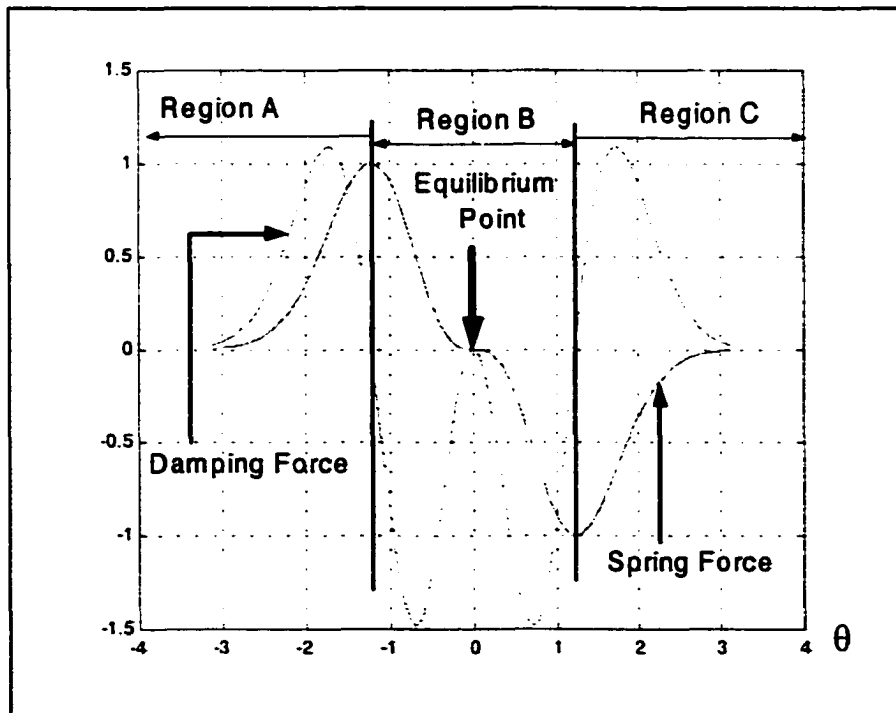


Figure 3.16: Spring force and damping force of an attractive force field.

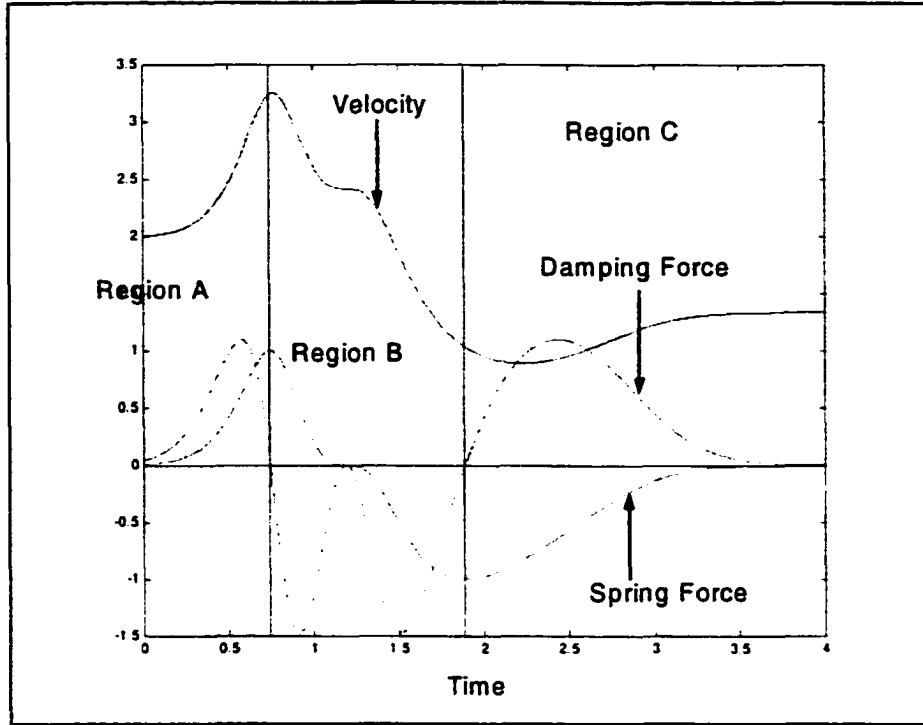


Figure 3.17: Effect of attractive well on the velocity response.

Assuming constant velocity, the work done by the damper can be expressed as

$$\begin{aligned}
 \text{Work} &= \int_0^{\infty} \frac{-\theta^{2DN} [2N\theta^2 - 2DN - 1]}{e^{\theta^2 N}} d\theta \\
 &= \int_0^{\infty} -2N\theta^{2DN+2} e^{-\theta^2 N} d\theta + \int_0^{\infty} (2DN + 1)\theta^{2DN} e^{-\theta^2 N} d\theta
 \end{aligned} \tag{3.28}$$

The first term of Eq (3.28) can be evaluated as:

$$\begin{aligned}
 &\int_0^{\infty} -2N\theta^{2DN+2} e^{-\theta^2 N} d\theta \\
 &= \left[\theta^{2DN+1} e^{-\theta^2 N} \right]_0^{\infty} - \int_0^{\infty} e^{-\theta^2 N} d(\theta^{2DN+1}) \\
 &= \left[\theta^{2DN+1} e^{-\theta^2 N} \right]_0^{\infty} - (2DN + 1) \int_0^{\infty} \theta^{2DN} e^{-\theta^2 N} d\theta
 \end{aligned} \tag{3.29}$$

We see that the second term of Eq (3.29) cancels with the second term of Eq (3.28).

Therefore the work done is simply

$$Work = \left[\theta^{2DN+1} e^{-\theta^2 N} \right] \geq 0 \quad (3.30)$$

From Eq (3.30), we know that the system damper does a positive work as the state moves from any other place to the equilibrium. Therefore, the overall system energy reduces. A second order system with a positive stiffness and the system damper is reducing the system kinetic energy as it moves from any point to the equilibrium state, we can conclude that the overall system is stable.

Simulation Results

In this section some simulations of attractive force field will be presented. Figure 3.18 shows the simulation result assuming a zero external applied force. In the simulation, we let the system start from the region where damping was negative with a finite initial velocity pointing toward the equilibrium. In this region, the system damping increased the overall system kinetic energy. Because of the negative damping factor and the attractive force, the state accelerated toward the equilibrium point. As soon as the state moved into the positive damping region, the system damper exerted a force opposite to the direction of the velocity and retarded the motion of the state. One can see the velocity in this region reduces as shown in the figure. The state finally settled down at the equilibrium.

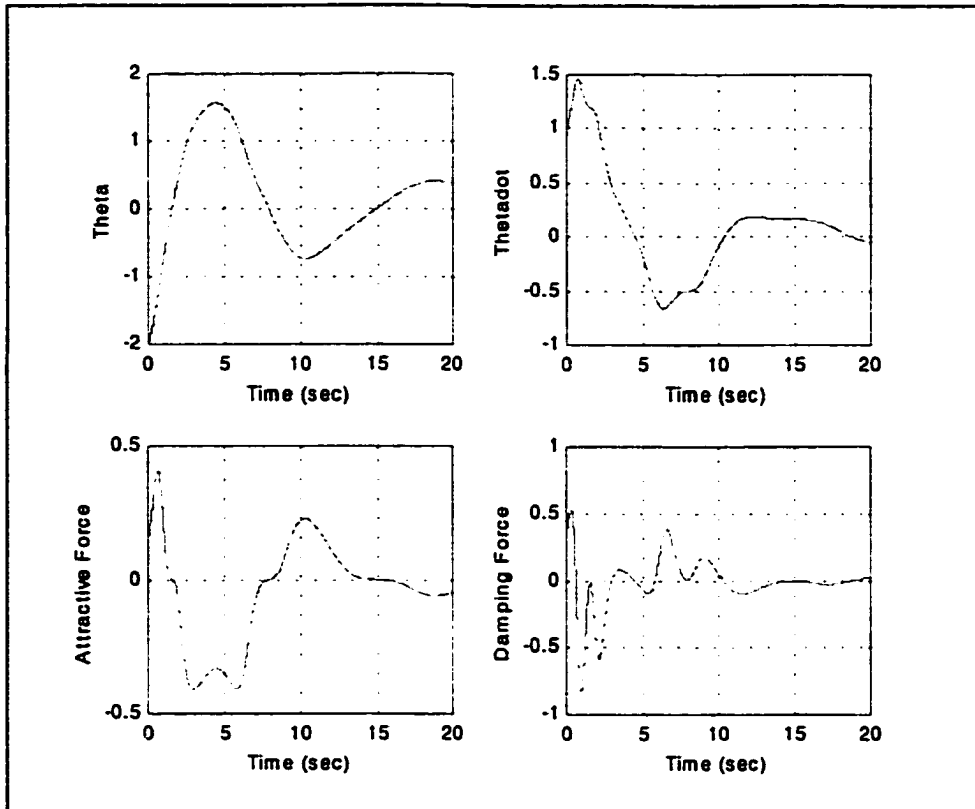


Figure 3.18: System response to an attractive well when $\theta = -2.0$, $\dot{\theta} = 1.0$

Figure 3.19 shows the system response when the initial velocity is large enough for the state to overcome the influence of the attractive well. The initial state was in the negative damping region with a large initial velocity pointing toward the equilibrium. From the top right figure, we see that the system damper increased the velocity of the state initially. As soon as the state went into the positive damping region, the velocity dropped because of the positive damping force. The velocity went down until the state entered the region where damping coefficient again became negative. From there, the velocity picked up.

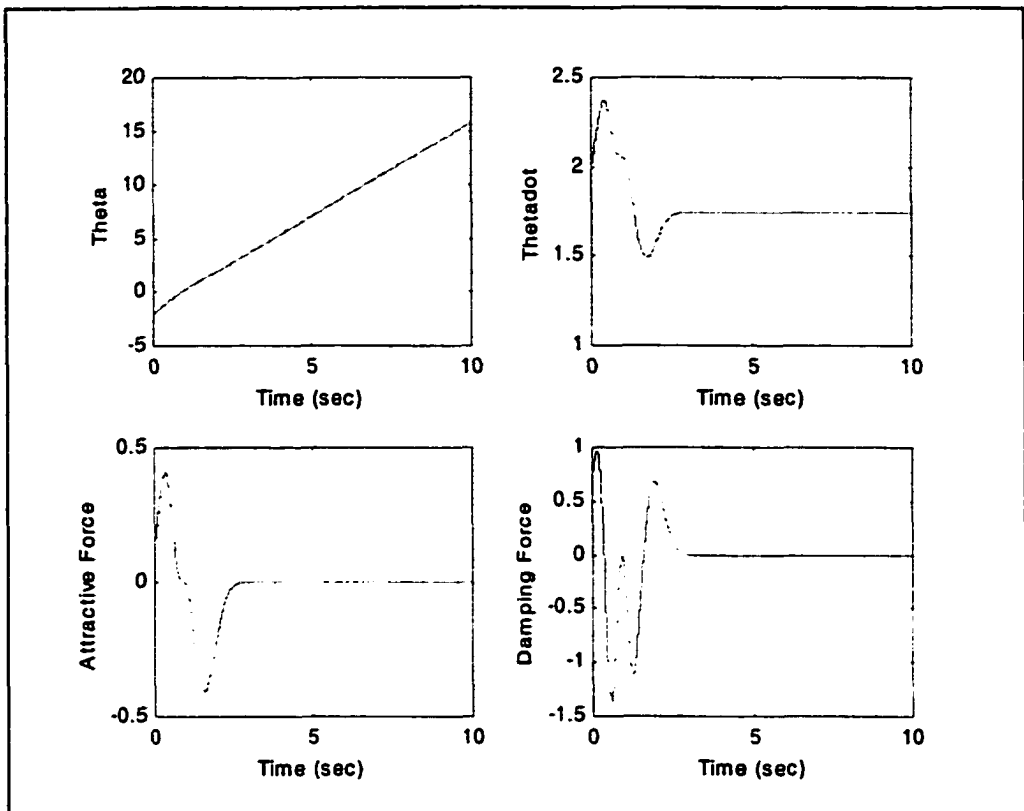


Figure 3.19: System response when the initial velocity is large

We made several observations on Figure 3.19. First, the simulation results showed that the system damper in overall did a positive work, i.e., the system kinetic energy dropped. Second, the attractive well is meant to guide and help the operator in maneuvering the work piece. The attractive force should be moderate enough so that the operator can overcome its effect if he wanted to. Finally, we want the influence of the attractive well to take effect only when the end effector is relatively close to it. From Figure 3.16, one can see that both the attractive and the damping force decayed quickly as the end effector moved away.

CHAPTER 4 EXPERIMENTAL RESULTS

In this chapter, the following experimental results will be presented. First, the system response to the user force inputs when the end effector is far from the artificial force field will be investigated. Both a loaded and unloaded machine will be tested. The user-applied forces and the actuation forces will be compared. Second, the controller compensating for the structural flexibility will be tested by examining the system response to high frequency excitations. Third, a modified repulsive force field based on joint angle will be constructed. Experimental result shows the stability of the modified repulsive force field. Fourth, a composite wall is constructed to simulate the real world obstacles. The implementation issues and limitations of the repulsive force wall will be discussed. Finally, an attractive force field is constructed for correcting the orientation of the payload when the end effector is in the proximity of the attractive force field region.

Experimental Result I

In this section, the experimental results showing the overall state controller will be presented. User applied forces, actuation forces and system response will be compared and contrasted. Figure 4.1 shows the top view of SAM at its home configuration and the global coordinate system that will be used throughout this chapter. The end effector in the figure represents where the wrist joint is located.

In the first experiment, the user applied command force to the handle in the global X direction (by pushing and pulling) for a few seconds, and then applied force in the global Y

direction for another few seconds. Finally, he applied forces in both X and Y directions and moment about the vertical axis to initiate a general plane motion.

Figure 4.2 shows the actuation force and user-applied force in the global X direction. In the real mechanism, the actuation force could not be measured directly. The actuation force shown in Figure 4.2 was calculated based on the command voltage, which was proportional to torque since we were in current mode on the amplifiers. From Chapter 2, the current from a PWM amplifier in current mode was directly proportional to the command voltage. The command voltage could then be used to approximate the actuation torque from the servomotor. Using the relationship between the joint torque and force at the end effector, we could calculate the equivalent actuation force.

In this experiment, the user-applied force was mainly in the normal direction (the global X direction as shown in Figure 4.1) in Region A of Figure 4.2. Referring to Figure 4.1, the motion in the global X direction at the home configuration was primarily carried out by the linear actuator. In Region B of Figure 4.2, the user-applied force was mainly in Y, the tangential direction. The base joint was primarily responsible for the motion. Finally, in Region C, the user applied forces in both directions and a moment about the vertical axis. In this case, the overall motion required coordination from all three actuators.

From Figure 4.2, we see that in Region A, the actuation force is simply a scaled version of the user-applied force. The actuation force followed the command faithfully. Notice that the actuation force was about twice the magnitude of the user-applied force. It indicated that the human was supplying about $1/3$ of the total motive force to the system. In Region B, the force in X direction was at minimum. In Region C, the actuation force in the X direction picked up again. In this region, all three actuators were involved in generating

the overall motion, and there was not a simple relationship between the applied force and the actuation force in any single direction.

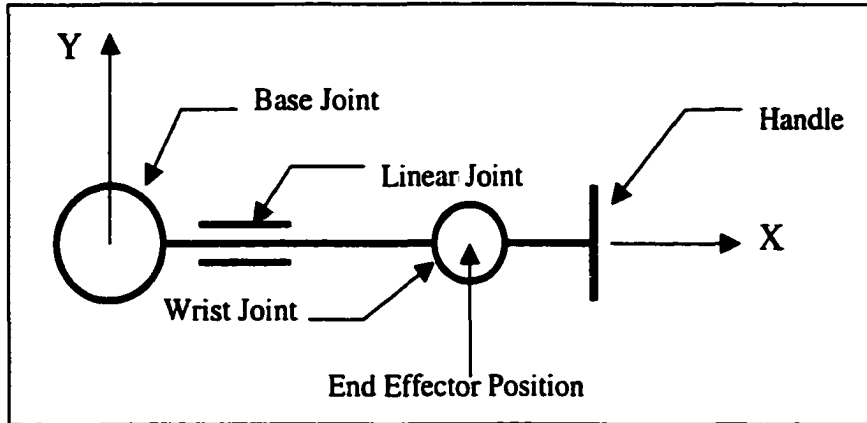


Figure 4.1: Home configuration of the SAM

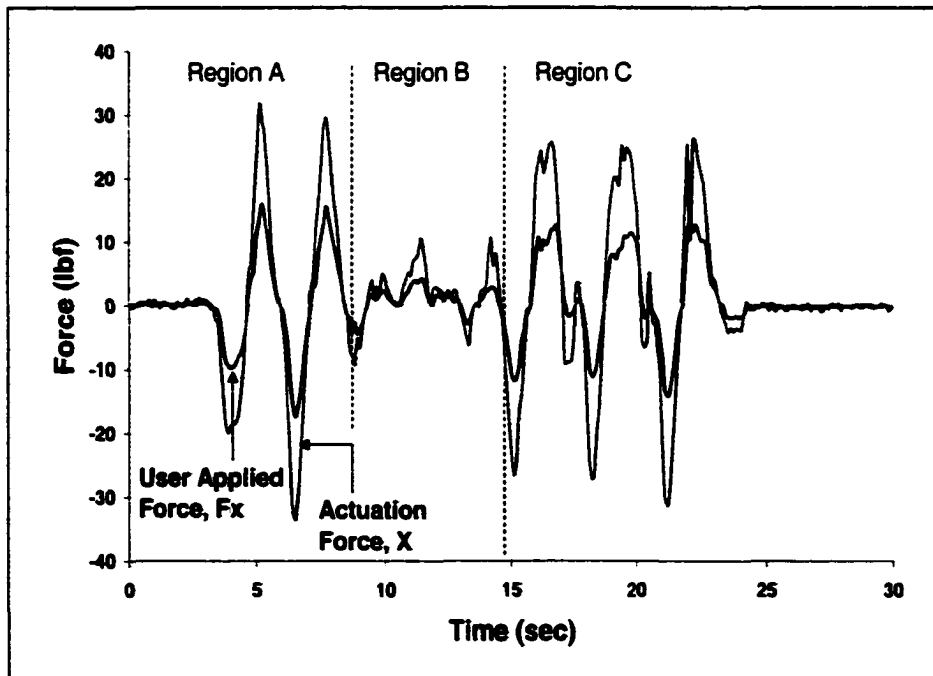


Figure 4.2: User-applied force and actuation force in X direction.

Figure 4.3 compares the applied force and the actuation force in the Y direction. In Region B, the actuation force followed the command closely. However, the actuation force was about 3 times the magnitude of the user-applied force, which was a larger scaling factor compared to the actuation force in the X direction shown in Figure 4.2. It was because this degree of freedom had a larger inertia, which was the inertia of the whole machine rotating about the main post. Therefore, it required a higher torque to accelerate the mechanism. In addition, human arm was stronger in the fore aft direction than the lateral direction, the controller was designed to be more sensitive to lateral motions of human arms to give a more uniform feeling. Consequently, we see a larger multiplying factor for the lateral force. In Region A, the actuation force was mainly from the linear actuator. The machine had a low inertia along this axis, and a low control gain was used for this joint.

Figure 4.4 compares the actuation moment and the user-applied moment. In Region C, the actuation moment deviated from the user-applied moment. Keep in mind that in this region; forces in both directions and a moment were applied to the system. Since the machine did not have uniform dynamics throughout the entire workspace, there was a certain degree of mismatch of the actuation forces. The changing of the machine inertia, which was a function of the machine configuration, Coriolis effect and centripetal force, could cause the mismatch of actuation forces. Despite all these factors, the actuation moment in general followed the control command.

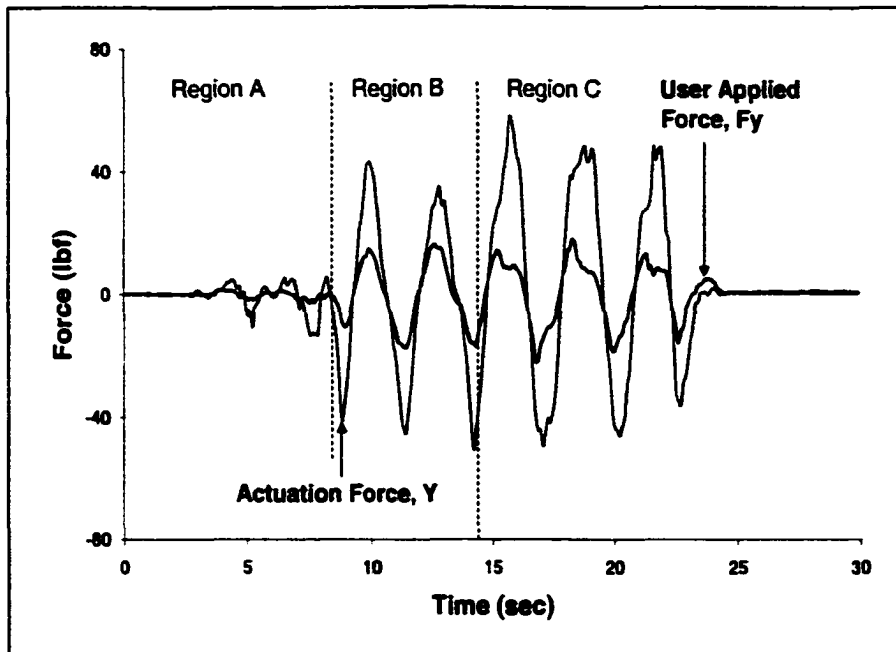


Figure 4.3: User-applied force and actuation force in Y direction.

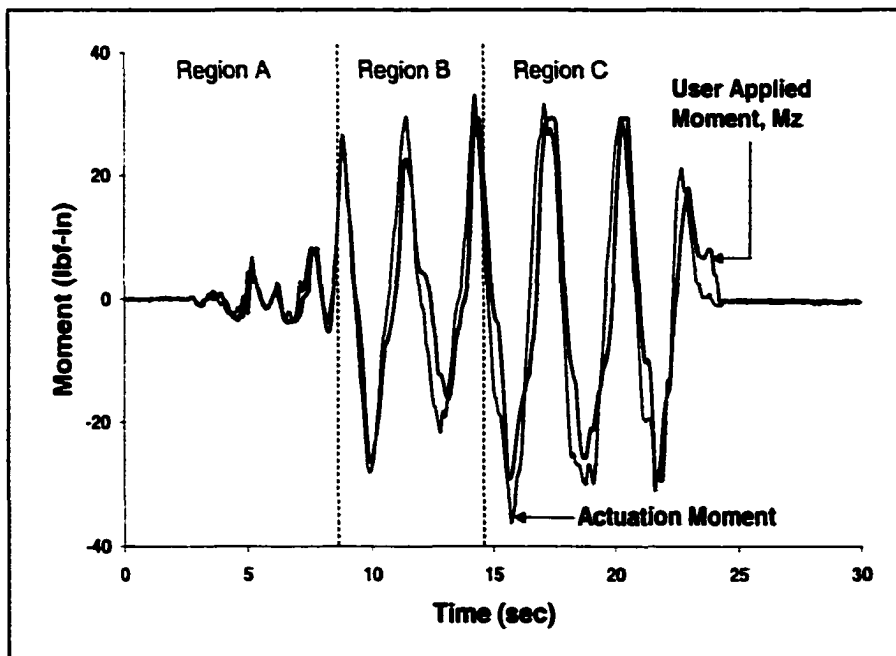


Figure 4.4: User-applied moment and actuation moment

Figure 4.5 shows the end effector position of the machine in the Y direction when it was subjected to the user-applied force discussed before. The end effector position moved in the direction of the user-applied force with a phase shift. From the force/displacement relationship, we see that indeed they are about 180 degree apart from each other. In addition, one could see that the system acted as a low pass filter that smoothed the control command.

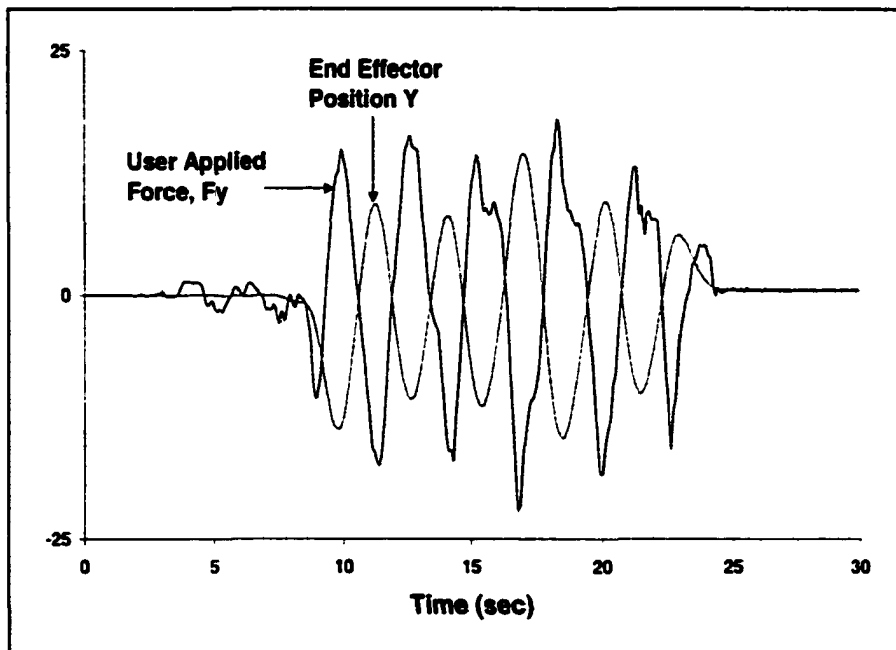


Figure 4.5: User-applied force and system response in Y direction.

In the second part of this experiment, a bucket, which was about 100 lbm, was chained to the end effector as shown in Figure 4.6. This is to test the system response when the machine is loaded. Figure 4.7 shows the actuation force and the user-applied force in the X direction. Same as the unloaded case, the actuation force was about twice the magnification of the user-applied force. The user was still supplying about 1/3 of the total

motive force to the system. Since the controller was open loop, the user would feel the increase of inertia when the machine was loaded. Figure 4.8 shows the actuation force and the user-applied force in the Y direction. This figure depicts similar information as Figure 4.3, and the magnification factor was also approximately 3.0. In this experiment, the steel hanging bucket was swinging when the machine was in motion. The pendulum behavior of the bucket reflected the inertia force back to the force transducer at the handle and interacted with the controller. Therefore, we see high frequency applied forces in Figure 4.8. It was also observed that the system was slightly more oscillatory compared to the unloaded case.



Figure 4.6: Machine with a 100 lbm payload.

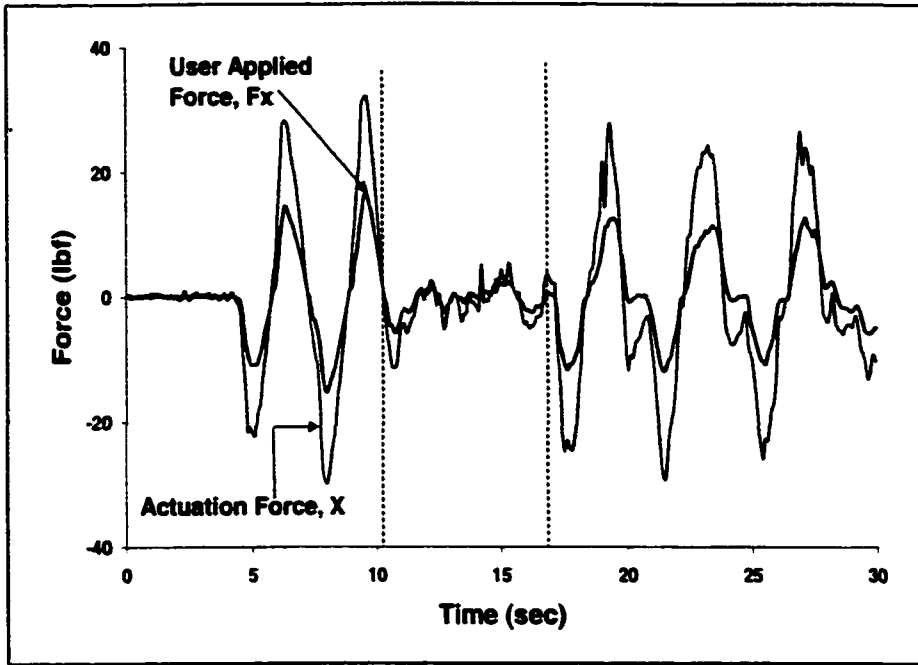


Figure 4.7: User applied force and actuation force in X direction with a 100 lbm payload.

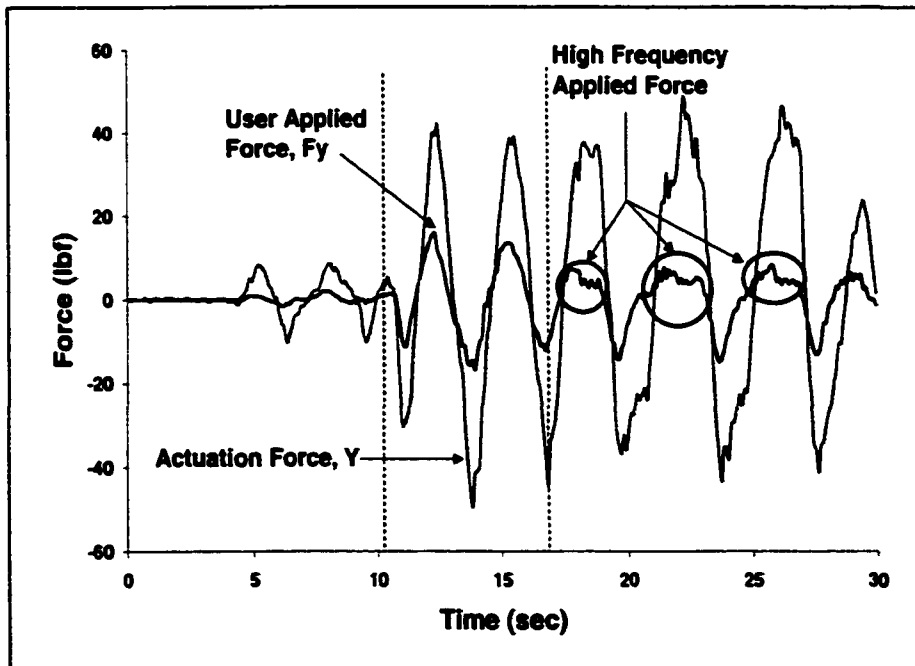


Figure 4.8: User applied force and actuation force in Y direction with a 100 lbm payload.

Experimental Result II

In this section, the controller having structural flexibility compensation will be tested. By observation, the machine encountered the first resonance at about 3-4 Hz. In the controller design, a pair of complex zero was put at the locations corresponding to 4 Hz with a damping ratio of 0.2 in order to cancel the dynamic effects resulting from the structural flexibility. The damping ratio used in the controller was based on our observation of the system behavior. It was noticed that the resonance frequency of the machine reduced when it was loaded with a heavy object. From the control-point-of-view, a system with a low natural frequency required more control effort since the control command must avoid the system natural frequency. Restraining the control commands to the low frequency range might make the overall system response to be sluggish.

Until now our system does not have the capability to identify the system resonance frequency in order to move the compensating zeros to the optimal locations. However, it is possible to use a system identification method to estimate the system natural frequency in real time.

In this experiment, the user applied an oscillating force in the global Y direction to excite the structure when the machine was at its home configuration. The tester was told to excite the structure at the frequency that he felt that would induce the most oscillations in the machine. It ended up that the excitation force had a frequency of about 4 Hz. The user-applied force and actuation-force from the controller were plotted against each other in Figure 4.9.

From Figure 4.9, one could see that the actuation force remained at about the same magnitude as the user-applied force and they were only slightly out of phase. The controller

did not magnify the control signal that would excite the structure. As soon as the user stopped to apply oscillation, the actuation force ceased and oscillations in the structure died out. This experiment alone could not prove the absolute stability of the system, but it told us that the oscillations in the structure did not induce self-excited vibration.

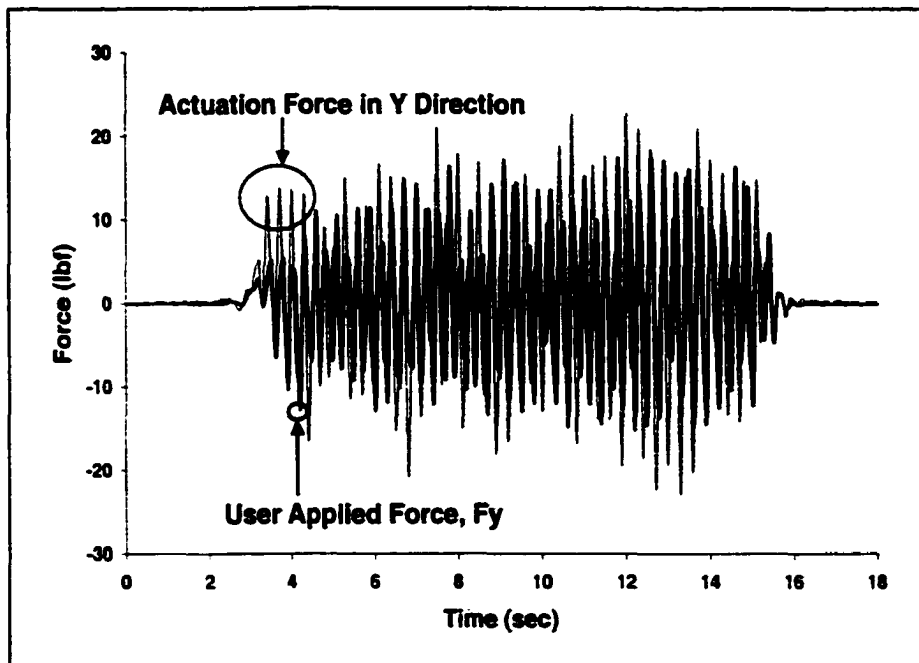


Figure 4.9: User-applied force & actuation force

Figure 4.10 shows the end effector position of the machine under excitation. Note that the force has a unit of lb., and the end effector takes on inch. In Figure 4.10, the end effector oscillated at the excitation frequency. However, the magnitude of the oscillations was very small. In fact, the machine could vibrate easily under the external excitations from a human being. Therefore, it is hard to decide if the actuation force or human-applied force had contributed more to the oscillations shown in Figure 4.10. Note that the end effector

position shown in Figure 4.10 was calculated based on the encoder readings of the base joint. In this experiment, the oscillations were contributed mostly by these three factors. They were the flexibility of the base joint, which included the looseness of chain, the elasticity of the link and the flexibility of the wrist joint.

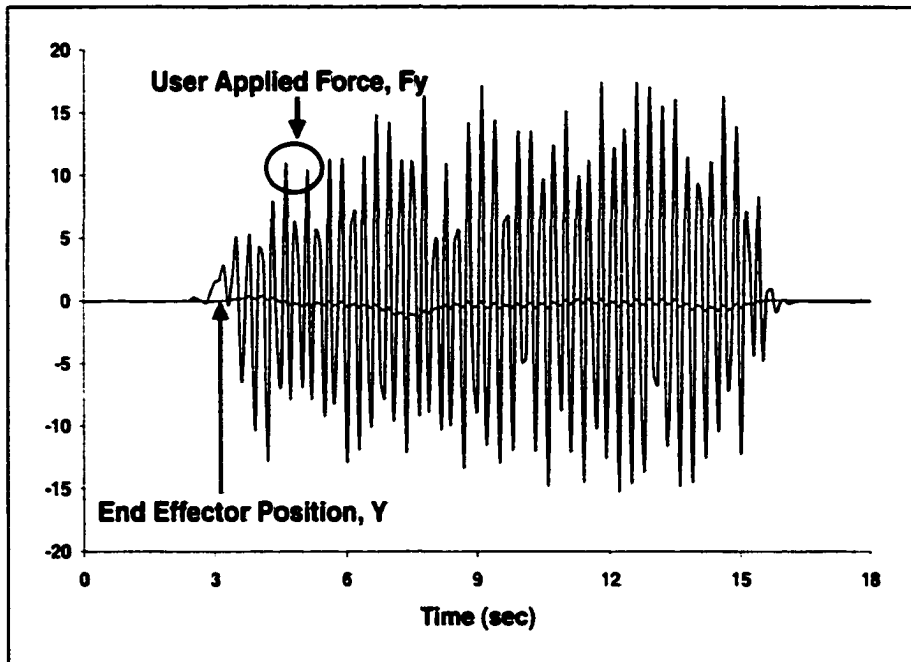


Figure 4.10: User-applied force & end effector position in Y.

The second part of the experiment was to turn the handle 90 degrees from its home configuration and applied excitation forces to excite the structural vibrations. This experiment differs from the previous one since the dynamics of the wrist joint is not directly coupled to the system. As shown in Figure 4.11, from 1.0 to 4.0 second, the user was turning the handle to about 90 degree from the home configuration. One could see that the actuation force was simply a multiple of the control command, according to the force magnification

factor discussed before. However, as soon as the user started to apply oscillatory force, the multiplication effect of the actuation force decreased.

Figure 4.12 showed the system response to the excitations. From 1.0 – 4.0 second, the system reacted to the user-applied force that was at a low frequency. However, as soon as the forcing function went into a high frequency region, starting from 5.0 to 9.0 second, the controller simply ceased to magnify the user applied force through actuators. One important thing to keep in mind was that the controller was different from a typical low pass filter. One could see that the actuation force followed the command with a small phase shift. The controller simply attenuated the magnitude of the actuation force.

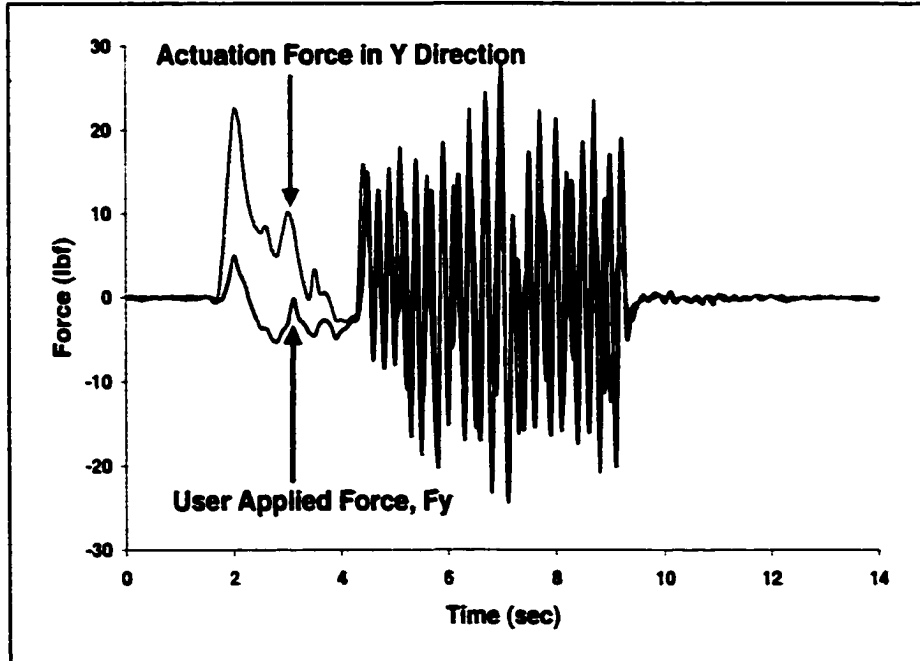


Figure 4.11: User-applied force & actuation force when the handle was at 90 degree.

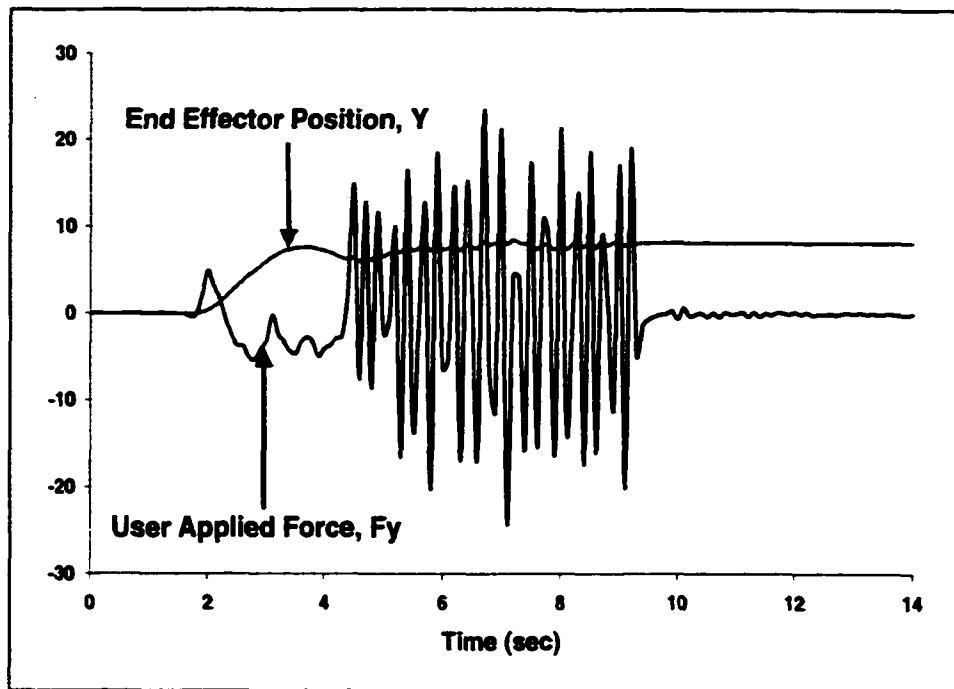


Figure 4.12: User-applied force & end effector position in Y direction.

Experimental Result III

In this section, stability of the modified repulsive algorithm is tested. The machine started up from its home configuration. A modified repulsive wall was constructed at $\theta_0 = 90^\circ$ as shown in Figure 4.13. By placing the wall at 90° , we could simply examine the magnitude of the user-applied force in the global X direction. In addition, the wall could be constructed by using only the base joint servomotor.

Figure 4.14 compares the actuation and command force when the machine was close to the repulsive wall. In the first 7 second, the user applied forces to move the machine toward the repulsive wall. As one could see, the actuation force and the command force were having the same direction. From 7.0 to approximately 18.0 second, the user was trying to

move the end effector into the wall. As soon as the end effector was in the neighborhood of the wall, the repulsive force algorithm took effect and generated an opposite force. Notice that the repulsive force was not exactly the mirror image of the user-applied force. This is because the force transducer used in this work is only capable of measuring up to about 17 lb. of force. With two force transducers, the maximum force that the program can measure is about 35 lb. At certain instant of time, the user was actually applying forces greater than 35 lb. From Figure 4.14, the repulsive force was as high as 40 lb. at some instant. However, even with this amount of force challenging the repulsive wall, we see that the system remained stable. After 18.0 second, the user pulled the machine away from the wall. As soon as the end effector was leaving the wall, again, the general controller took effect and generated an actuation force in the direction of the command force. In Figure 4.14, there are two spots (Note 1) where the user-applied force was high, but the actuation force was low. In addition, the actuation force and the user-applied force had the same direction. If one looked closely, he would find that at those instances, the end effector was rather far from the repulsive wall. The repulsive algorithm was not active at these instances. Therefore, the actuation force was helping the operator instead of acting against him.

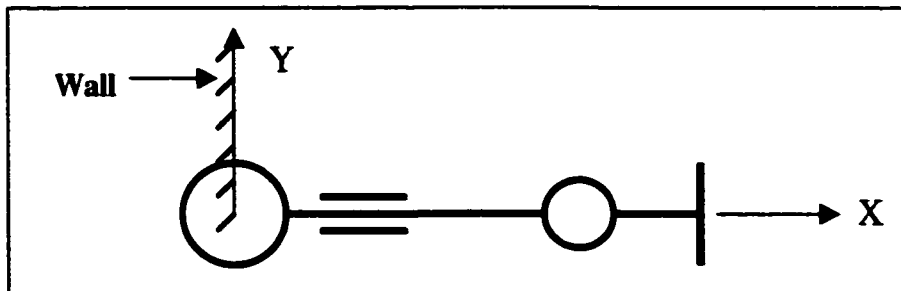


Figure 4.13: A simple repulsive wall.

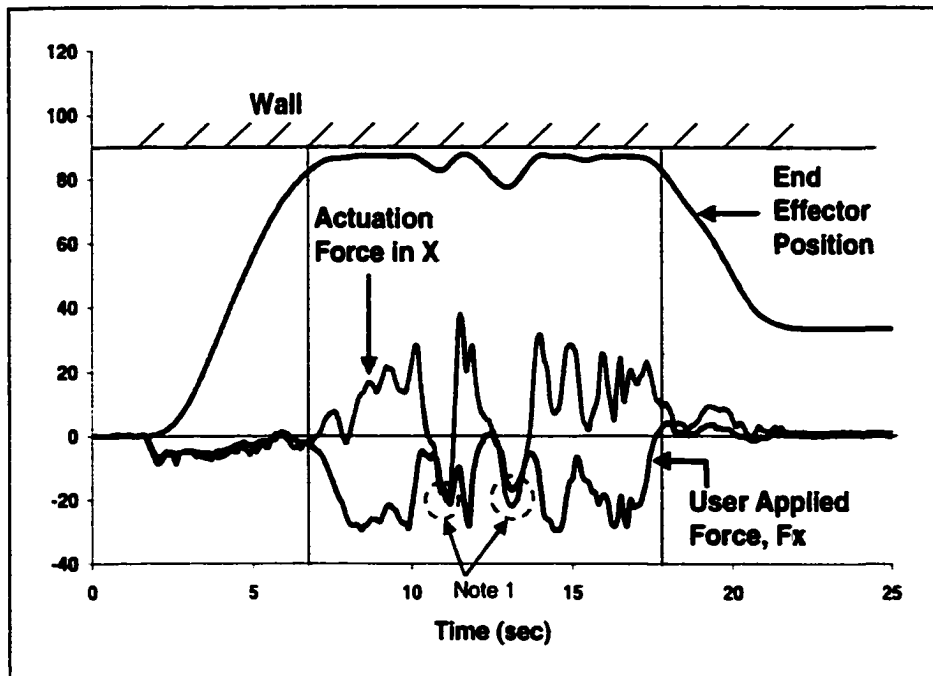


Figure 4.14: A simple repulsive wall at 90° .

Experimental Result IV

In this section, a composite repulsive wall as shown in Figure 4.15 is constructed. Implementation issues and limitations will be addressed. Finally, the experimental results will be presented.

Figure 4.15 shows the shape of the composite wall built for this research. The payload was modeled as a rectangular box with certain finite dimensions. The operator needs to move the payload to the specified target point without colliding with the environment. The objective of the wall was to prevent the payload from running into obstacles that might be behind the wall. In addition, the payload was modeled as a rectangular box to simulate a real world object. As one could see, the payload could only

arrive at the target point with one possible orientation. This model might represent a car-door assembly operation. The operator needed to move the payload toward a specific spot at a fixed orientation. During the process, the operator had to be careful enough not to run the car door assembly into the body of the vehicle. If the workspace was large enough, the payload could simply be modeled as a sphere to save computational cost. However, considering the space that might be taken to embody the payload if it had a rectangular shape, a spherical modeling might decrease the useable workspace for the operator significantly. Another feature one should pay attention to was the modeling of the wall's corners. Instead of using a sharp edge, we used a circular segment to provide a smooth transition from one wall to the next.

Figure 4.16 shows one of the fundamental problems in modeling a sharp corner. The circle in the figure represents the end effector that needs to avoid contacting with the wall. The thick arrow represents the repulsive force acting on the end effector. If the end effector is outside the wall as shown in region A and B of Figure 4.16, the direction of the repulsive force is well defined. However, once the end effector is inside the wall, as shown in region C of the figure, both the magnitude and direction of the repulsive wall will be uncertain. To overcome this uncertainty, in this research, a circular segment was used to model a corner to provide a smooth transition from one wall to the next and it is shown in Figure 4.17.

In Figure 4.17, the direction of the repulsive force was well defined in region A', B' and C'. If the end effector was able to penetrate the wall, according to the modified repulsive wall formulation discussed before, the direction of the repulsive force was still well defined as long as the end effector stayed in region A, B or C. However, as soon as the end effector entered region D, the direction of the repulsive force would then be uncertain.

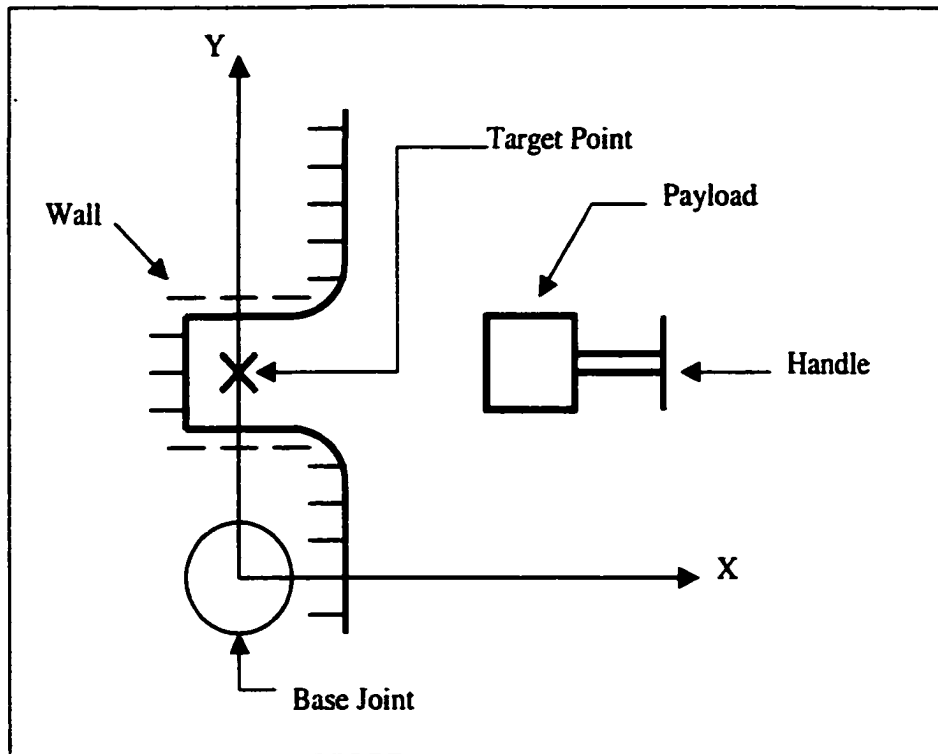


Figure 4.15: A composite repulsive wall.

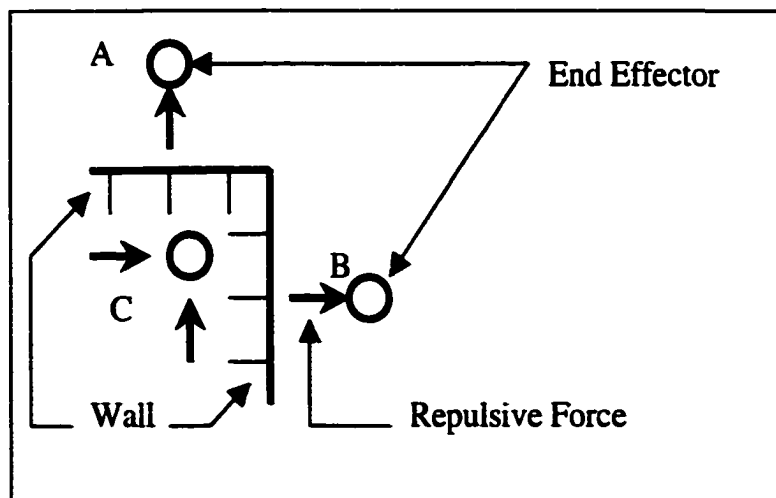


Figure 4.16: Modeling of a sharp corner.

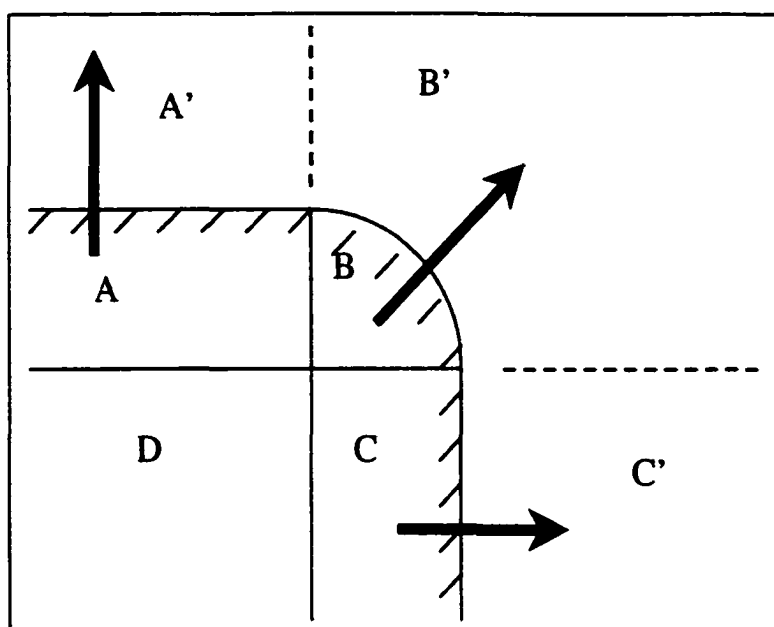


Figure 4.17: A circular segment corner.

One approach to the problem is to prevent the end effector from entering region D. This can be accomplished by creating a very thick wall and letting the actuator to output a maximum force before the entering of end effector into region D. Of course, we are making an important assumption that the operator is not strong enough to overpower the actuator.

In the first experiment of this section, the end effector was moved toward the repulsive wall as shown in Figure 4.18. The size of the payload and the locations of repulsive walls were drawn to scale in the figure. In this experiment, the wrist joint was kept at a relatively constant angle. The end effector was pushed toward the wall at the beginning of the motion. Once the repulsive wall had resisted the inward motion, the payload was pushed side way to slide along the repulsive wall until the payload moved into the tunnel entirely. Finally, the payload was pulled back from the tunnel and moved back to the home

configuration along the forward path in reverse direction. The whole motion lasted for about 20 seconds. From the motion trajectory in Figure 4.18, we found that the payload kept at a relatively constant distance from the repulsive wall although the user-applied forces were not at constant. Part of the trajectory even shows the circular nature of the corner.

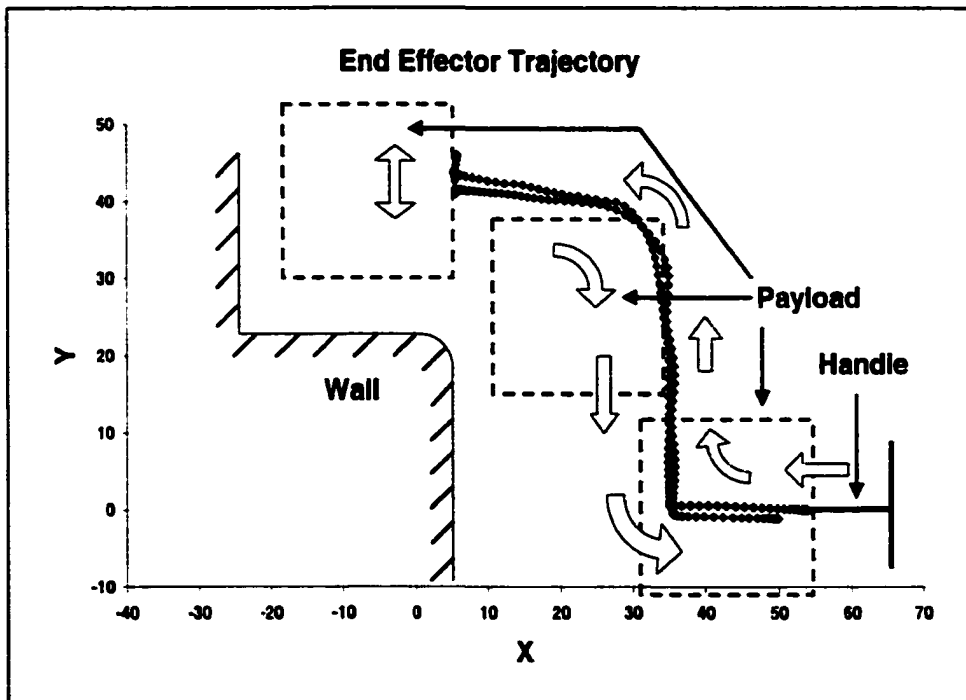


Figure 4.18: End effector trajectory.

Figure 4.19 compares the user-applied force, the repulsive force and the actuation force. In the first 4 seconds, the user pushed the payload toward the wall. Since it was far away from the wall, the repulsive force was zero and the actuation force was helping the operator to move the payload. At about 4.0 second, the repulsive force grew from zero to 30

lb. quickly. It was because the end effector was within the proximity of the wall and the repulsive algorithm started to have an effect. From 4.0 to 8.0 second, the actuation force resisted the motion by applying a force that was opposite to the user force. The actuation force was roughly the magnitude of the user-applied force. However, they were not exactly the mirror image of the other because the repulsive force was very sensitive to the distance of the payload to the wall. A slight variation in the distance made a large change in the magnitude of the repulsive force.

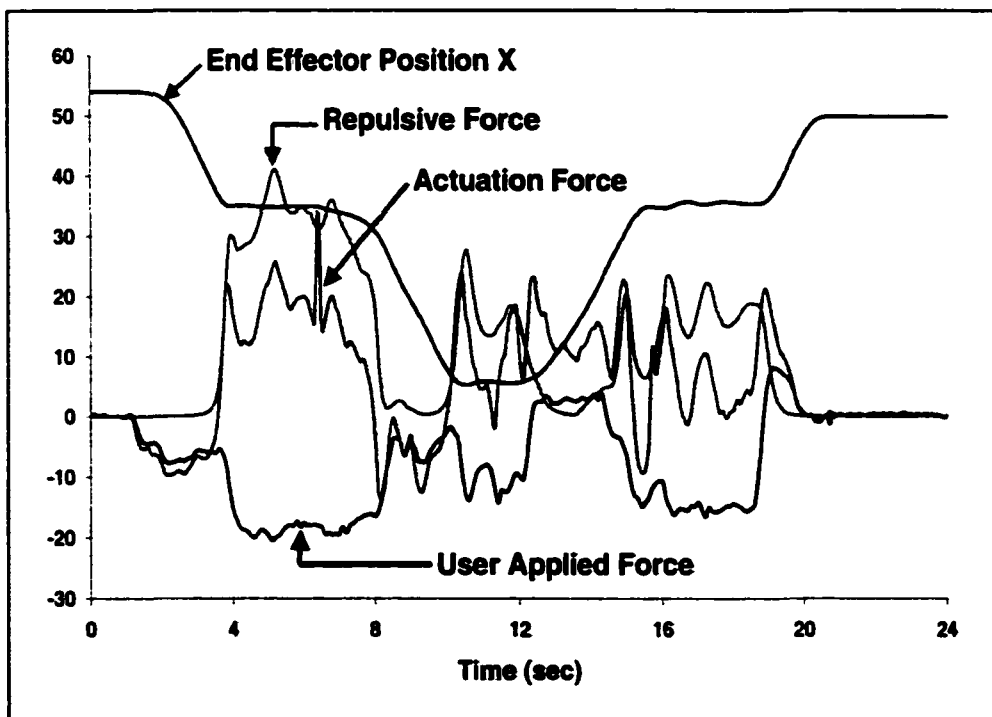


Figure 4.19: Actuation force & repulsive force on the payload

In the second part of this experiment, the payload was moved toward the target position with the wrist joint at an angle. The user applied a force against the repulsive wall for the entire motion of this experiment, except when the end effector was far away from the wall. The end effector trajectory was plotted in Figure 4.20. The location of the repulsive wall was also shown in the figure for comparison. One would notice that the trajectory did not follow the shape of the repulsive wall closely as it did before (Figure 4.18). It was because the user was moving the payload to approach the target point at an angle as shown in Figure 4.21. In Figure 4.21, the shape of the payload was superimposed on the end effector trajectory to show its motion in details. By plotting the shape of the payload, one would find that the shortest distance of the payload to the repulsive wall was approximately kept at a constant. Be aware that Figure 4.20 only shows the payload in the forward path of the entire motion trajectory to avoid drawing too many lines on the same figure.

Figure 4.22 compares the actuation force, repulsive force and user-applied force for the forward path shown in Figure 4.21. In the figure, the user applied force F_x was always in the negative direction so that the payload could be pushed against the wall. On the other hand, the repulsive force was always in the positive direction to resist the motion of the payload. It implied that the user-applied force and repulsive force worked against each other in the entire time span shown in Figure 4.22. Depending on the shortest distance from the payload to the repulsive wall, the actuation force, that was the actual force felt by the operator, could be in either positive or negative direction.

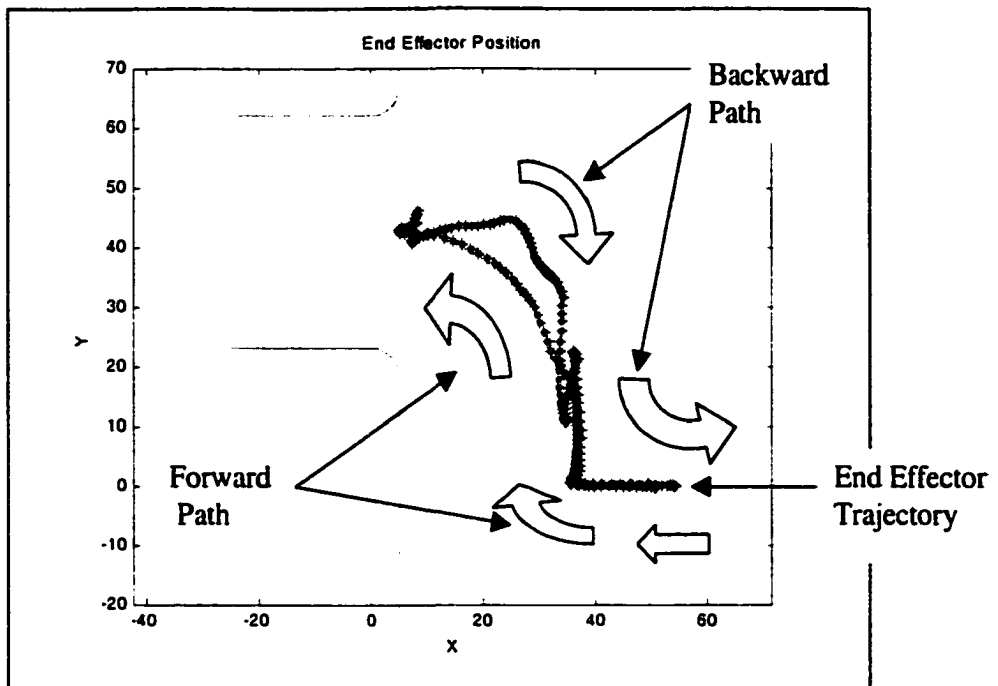


Figure 4.20: End effector trajectory of payload.

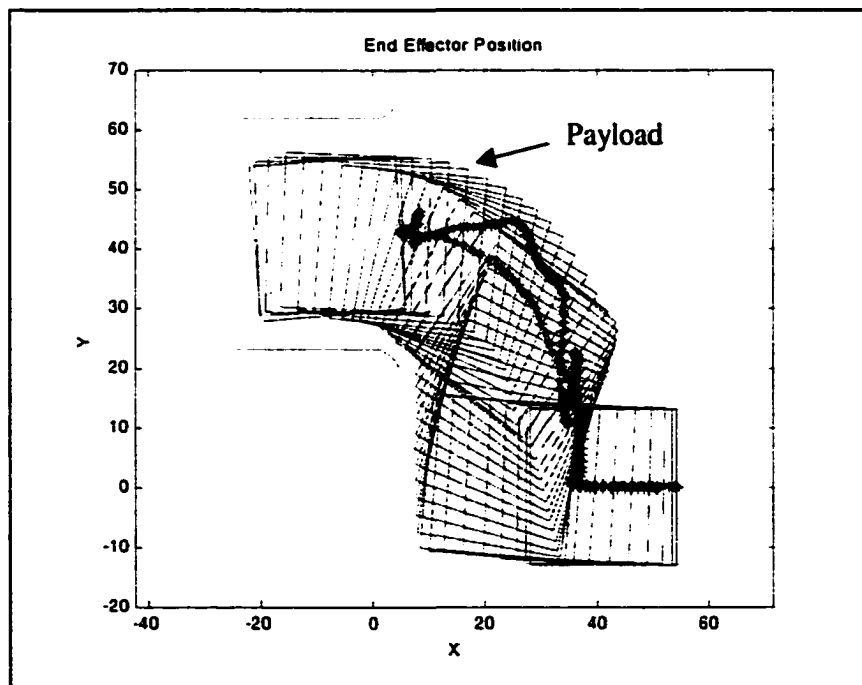


Figure 4.21: Forward path motion of payload.

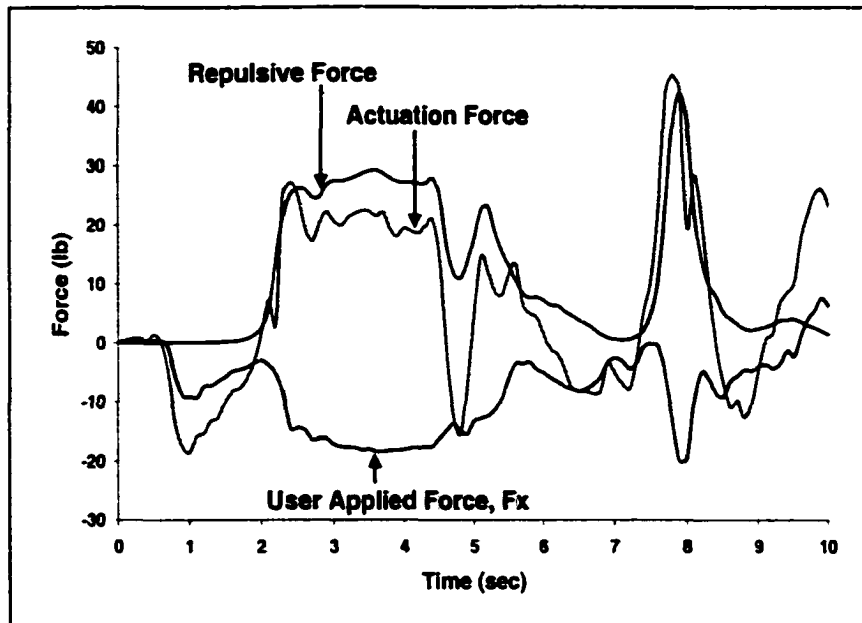


Figure 4.22: Actuation force, repulsive force and user-applied force.

Experimental Result V

Figure 4.23 shows another problem we faced in programming an IAD. When the payload was inside the tunnel, the user could always turn the payload so that the two opposite corners of the payload had the same distance to the repulsive wall. The repulsive force was calculated based on the absolute distance of the payload to the wall. As the result, the repulsive force resulted from the 'higher' wall canceled the one from the 'lower' wall. Consequently, the corners of the payload would penetrate the wall with zero overall repulsive force acting on the end effector.

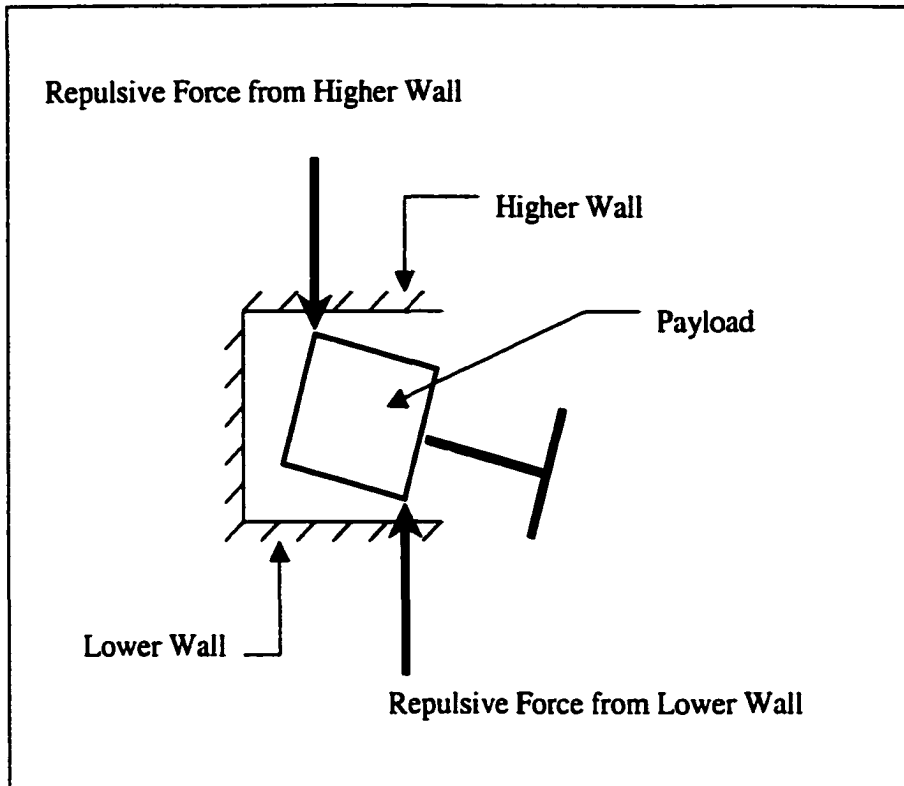


Figure 4.23: Cancellation of repulsive forces from different walls

There are two solutions to this problem. A natural approach will be to find out the moment resulting from the repulsive forces and use the moment to correct the overall motion of the machine. Another approach is to use the attractive well formulation as discussed in Chapter 3 to correct the payload orientation. In this research, we chose to explore the second approach.

The attractive force field constructed for this research is shown in Figure 4.24. The objective of constructing an attractive well is to resist the user from turning the handle when the payload is inside the tunnel. Therefore, an attractive force field formulation was implemented for the moment. The attractive moment was made localized by limiting its

effect to a small neighborhood inside the tunnel by multiplying a decaying function with the form $e^{-(Distance)}$. *Distance* is the absolute distance from the end effector $\langle X_{End\ Effector}, Y_{End\ Effector} \rangle$ to the designated target point $\langle X_{Target}, Y_{Target} \rangle$ where the attractive force field will have the maximum effect. *Distance* can be calculated as follows:

$$1) \text{Distance} = \sqrt{(X_{End_Effector} - X_{Target})^2 + (Y_{End_Effector} - Y_{Target})^2} - \text{Radius}_{(small\ neighborhood)}$$

2) If $Distance < 1.0$, then $Distance=1.0$.

Eq (3.24) was used to calculate the attractive moment with $D=0.0$, $N=20.0$ and $\eta=50.0$. The desired orientation of the payload inside the tunnel was that the sum of wrist joint and the base joint be equal to zero degree.

Figure 4.25 shows the experimental result of the user applied moment and attractive moment when the payload was both outside and inside the effective radius of the attractive well. The orientation of the payload was shown as the sum of base joint and wrist joint angle. From approximately 0.0 to 10.0 second, the payload was outside the radius of influence of the attractive well. In this time, the moment from the attractive formulation was equal to zero. From about 10.0 to 18.0 second, when the payload was inside the tunnel, the attractive well locked on the payload and took effect. From the figure, we saw that the user kept challenging the attractive well by applying moments to change the orientation. The attractive well generated a corrective moment based on the actual orientation of the payload trying to bring the actual orientation back to zero degree. Generally, from Figure 4.25, the magnitude of the attractive moment was larger than the user-applied moment. It was because the attractive moment had to work against the command moment, which was generated by the controller, and the real moment that was applied by the operator.

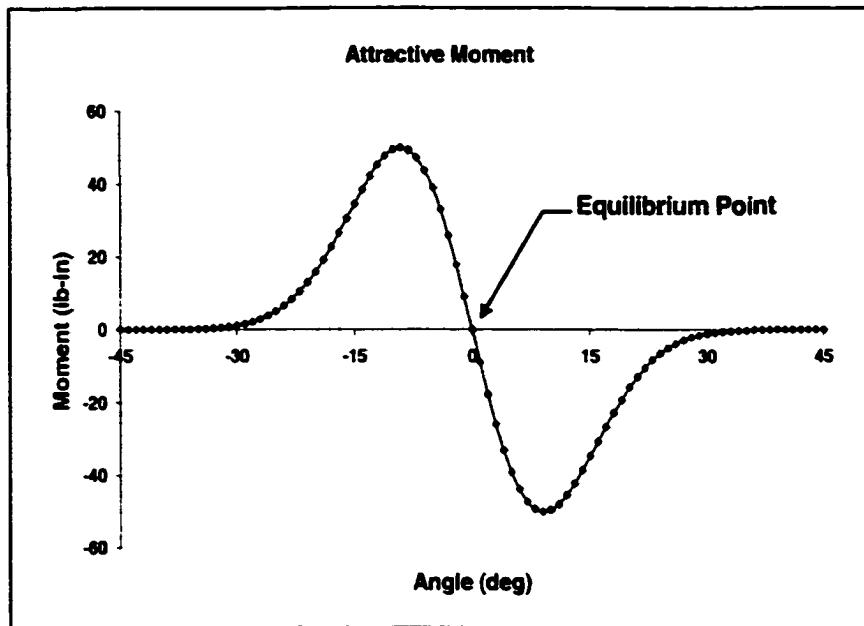


Figure 4.24: Attractive moment

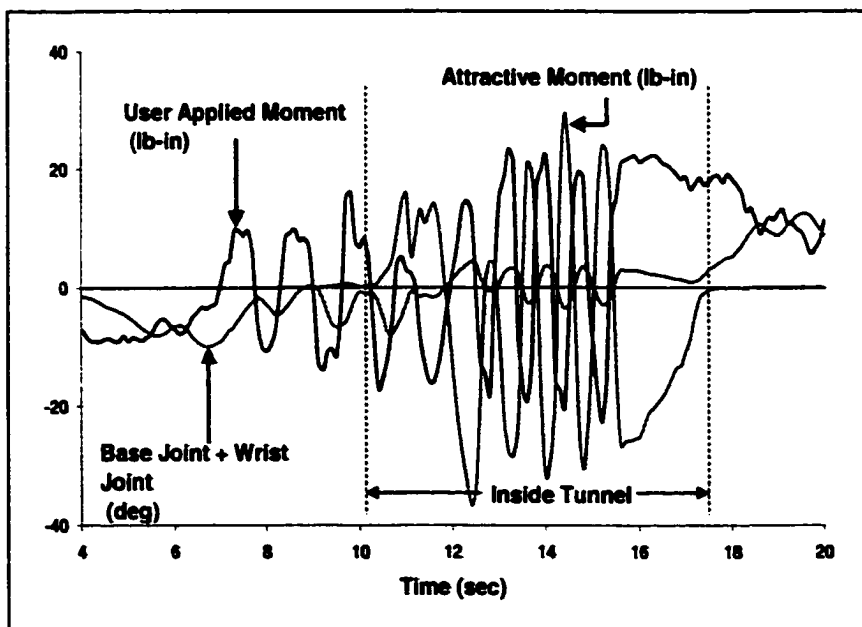


Figure 4.25: Attractive moment when the payload was inside the tunnel.

CHAPTER 5 CONCLUSIONS AND FUTURE WORK

The concept of IAD can be implemented in a wide variety of lift assisted mechanisms. Because of the power actuation, the ergonomic injury of the operator can be reduced, and the performance can be improved. A force transducer provides a convenient way for the operator to generate a control command by a simple “push to move” intuition. Therefore, there is a minimum training required for using an IAD. Collision of payload with obstacles has always been a major problem in using a lift assist device. Collision might cause damage to the work piece, lift device itself and sometimes result in operator injury. All these occurrences would significantly increase the total production cost. For a remote controlled master/slave robotic manipulator or an autonomous manipulator, collision avoidance schemes had been well developed for a long time. It was found that the most commonly used collision avoidance scheme, the repulsive field formulation, would be unstable if a human operator was integrated into the system. In this work, a modified collision-avoidance scheme had been proposed, and it had been proven stable both analytically and experimentally. In the original collision-avoidance scheme, the end effector of a manipulator could not penetrate the repulsive force field. On the other hand, in the modified collision avoidance formulation, the end effector was allowed to. One of the dilemmas of allowing the end effector to penetrate the wall was that the direction of the repulsive force was not well defined once the end effector was inside the wall. To solve the problem partially, in this work, a circular segment was used to replace a sharp corner to ensure the direction of the repulsive wall would be well defined when the end effector was

inside the wall. In addition, a round corner provided a smooth transition of the direction of the repulsive force from one wall to the next. In this work, a composite wall was used to model the obstacles in a car-door assembly operation. A composite wall could be used to model a large class of obstacles. However, it suffered the drawback of requiring a high computational cost. With the advance in the computer technology, this drawback would be less significant in a very near future. Attractive force field was briefly touched and discussed in this work. An attractive well was constructed to guide the operator in moving the payload to approach a specific target location in a specific orientation.

Several areas can be further explored on this research. First, a linear system-identification method can be built to estimate the parameters that are critical to the system performance and stability. For instance, estimating the mass of the payload in real time would allow the controller to adjust the overall gain and achieve a better, stable system behavior. A system identification method can also be utilized to estimate the system resonance frequency. The system resonance is a function of a several variables such as the mass of the payload, arm flexibility, looseness of the joint bearing, system friction, damping and so on. These parameters might change during operation. Next, in the controller design for this mechanism, the inertia effect was considered significant and it was compensated for in the overall gain design. For a low speed operation, this is a good approximation. As the speed of operation increases, other factors such as centripetal and Coriolis force will become prominent. A full inverse plant controller can be built to fully compensate these effects.

REFERENCES

- [1] Safety and Health Statistics, Workplace Injury and Illness Summary, Bureau of Labor Statistics, U.S. Department of Labor, Dec 12, 2000.
<http://stats.bls.gov/news.release/osh.nr0.htm>.
- [2] H. Kazerooni, and J. Guo, "Human Extenders," *Journal of Dynamic Systems, Measurement, and Control*, **115** (2B): pp.281-290, 1993.
- [3] J. E. Colgate, and W. Wannasuphoprasit, "Cobots: Robots for Collaboration with Human Operators," The ASME International Mechanical Engineering Congress and Exposition, Atlanta, pp.433-440, 1996.
- [4] Chai, Y. H., "Force Reflecting Haptic Interactions in a Synthetic Environment," Ph.D. dissertation, Iowa State University, 1997.
- [5] Edwards, J., "Interactive Synthetic Environments with Force Feedback," Ph.D. dissertation, Iowa State University, 1998.
- [6] N. Hogan, "Mechanical Impedance of Single- and Multi-Articular Systems," *Multiple Muscle Systems: Biomechanics and Movement Organization*, Chapter 9, J. M. Winters and S. L-Y. Woo (ed.), Springer-Verlag, New York, pp.145-164, 1990.
- [7] Lanman, J. M., "Movement and the Mechanical Properties of Intact Human Elbow Joint". Ph.D. Thesis, Department of Psychology, MIT, 1980.
- [8] Hayes, K. C. and Hatze, H., "Passive Visco-Elastic Properties of the Structures Spanning the Human Elbow Joint, *European J. Applied Physiology*, **37**: pp.265-274, 1977.
- [9] Cannon, S. C. and Zahalak, G. I., "The Mechanical Behavior of Active Human Skeletal Muscle in Small Oscillations", *J. Biomechanics*, **15**: pp. 111-121, 1982.

- [10] N. Hogan, "Controlling Impedance at the Man/Machine Interface", IEEE International Conference on Robotics and Automation, Scottsdale, AZ, USA, p 1626-1631, May 14-19, 1989.
- [11] Chen, J., Siegler, S., and Schneck, C. D., "The Three Dimensional Kinematics and Flexibility Characteristics of the Human Ankle and Subtalar Joints, II. Flexibility Characteristics," J. Biomech. Eng., **110**: pp.374, 1988.
- [12] Kearney, R. E., Hunter, I. W., "System Identification of Human Joint Dynamics," Critical Reviews in Biomedical Engineering, **18** (1): pp.55-87, 1990.
- [13] Houk, J. C., "Regulation of Muscle Stiffness by Skeletomotor Reflexes," Ann. Rev. Physiol., **41**: pp.99, 1979.
- [14] Cannon, S. C. and Zahalak, G. I., "The Mechanical Behavior of Active Human Skeletal Muscle in Small Oscillations," J. Biomech., **15**: pp.111, 1982.
- [15] Lakie, M., Walsh, E. G., and Wright, G. W., "Resonance at the Wrist Demonstrated by the Use of a Torque Motor: An Instrument Analysis of Muscle Tone in Man," J. Physiol., **353**: pp.265, 1984.
- [16] Lacquantti, F., Licata, F., and Soechting, J. F., "The Mechanical Behavior of the Human Forearm in Response to Transient Perturbations," Biol. Cybern., **44**: pp.35, 1982.
- [17] Cooker, H. S., Larson, C. R., and Luschei, E. S., "Evidence that the Human Jaw Stretch Reflex Increases the Resistance of the Mandible to Small Displacements," J. Physiol., **308**: pp.61, 1980.
- [18] W. Wannasuphprasit, R. B. Gillespie, J. E. Colgate, and M. A. Peshkin, "Cobot Control," IEEE International Conference on Robotics and Automation, pp.3570-3576, 1997.

- [19] R. B. Gillespie, J. E. Colgate and M. Peshkin, "A General Framework for Cobot Control," Proceedings of the IEEE International Conference on Robotics and Automation, Detroit, Michigan, pp.1824-1830, May, 1999.
- [20] Akella, P.; Peshkin, M.; Colgate, E.; Wannasuphoprasit, W.; Nagesh, N.; Wells, J.; Holland, S.; Pearson, T.; Peacock, B., "Cobots for the Automobile Assembly Line," 1999 IEEE International Conference on Robotics and Automation, 1:pp. 728 – 733, 10-15 May 1999.
- [21] S. D. Eppinger and W. P. Seering, "Modeling Robot Flexibility for Endpoint Force Control," Proceedings of the IEEE International Conference on Robotics and Automation, pp.165-170, 1988.
- [22] S. D. Eppinger and W. P. Seering, "On Dynamic Models of Robot Force Control," Proceedings of the IEEE International Conference on Robotics and Automation, pp.29-34, 1986.
- [23] S. D. Eppinger and W. P. Seering, "Understanding Bandwidth Limitations in Robot Force Control," Proceedings of the IEEE International Conference on Robotics and Automation, pp.904-909, 1987.
- [24] W. B. Cevarter, "Basic Relationships for Control of Flexible Vehicles," AIAA Journal, 8 (4): pp.666-672, April, 1970.
- [25] D. E. Whitney, "Force Feedback Control of Manipulator Fine Motions," Proceedings of the Joint Automatic Control Conference, 1976.
- [26] Craig, J. J., Introduction to Robotics: Mechanics and Control, Addison-Wesley, MA, 1989.

- [27] M. Raibert, J. Craig, "Hybrid Position/Force Control of Manipulators," *ASME Journal of Dynamic Systems, Measurement, and Control*, June, 1981.
- [28] E. Colgate, N. Hogan, "Robust Control of Manipulator Interactive Behavior," *International Journal of Control*, **48** (1): pp.65-88, July, 1988.
- [29] Wells, R. L., Schueller, J. K., Tlustý, J., "Feedforward and Feedback Control of a Flexible Robotic arm," *Control System Magazine, IEEE*, **10** (1):pp. 9-15, January, 1990.
- [30] Hasting, G. G., Book, W. J., "Verification of a Linear Dynamic Model for Flexible Robotic Manipulators," *International Conference on Robotics and Automation, IEEE*, pp.359-364, 1986.
- [31] A. De Luca, "Feedforward/Feedback Laws for the Control of Flexible Robots," *Proceedings of the 2000 IEEE International Conference on Robotics and Automation, San Francisco, CA*, pp.233-240, April, 2000.
- [32] A. Garcia, V. Feliu, "Force Control of a Single-Link Flexible Robot Based on a Collision Detection Mechanism," *Proceedings of the IEEE Conference on Control Theory Application*, **147** (6): pp.588-595, November, 2000.
- [33] H. Kazerooni, S. L. Mahoney, "Dynamics and Control of Robotic Systems Worn by Humans," *ASME Journal of Dynamic Systems, Measurement, and Control*, **133** (3): pp.379-387, 1991.
- [34] H. Kazerooni, "The Human Power Amplifier Technology at the University of California, Berkeley," *Robotics and Autonomous Systems*, **19** (2): pp179-187, December, 1996.
- [35] O. Khatib, "Real-Time Obstacle Avoidance for Manipulators and Mobile Robots," *The International Journal of Robotics Research*, **5**(1): pp.90-98, 1986.

- [36] P. Veelaert, and W. Bogaerts, "Ultrasonic Potential Field Sensor for Obstacle Avoidance," *IEEE Transactions on Robotics and Automation*, **15** (4): pp.774-779, August, 1999.
- [37] A. K. C. Wong, R. V. Mayorga, L. Rong, and X. Liang, "A Vision Based On-Line Motion Planning of Robot Manipulators," *Proceedings of the IEEE/RSJ International Conference on Intelligent Robots and System*, pp.940-948, November, 1996.
- [38] J. Borenstein, and Y. Koren, "Teleautonomous Guidance for Mobile Robots," *IEEE Transactions on Systems, Man, and Cybernetics*, **20** (6): pp.1437-1443, 1990.
- [39] J. Borenstein, and Y. Koren, "Real-Time Obstacle Avoidance for Fast Mobile Robots," *IEEE Transactions on System, Man, and Cybernetics*, **19** (5): pp.1179-1187, 1989.
- [40] J. Borenstein, and Y. Koren, "The Vector Field Histogram-Fast Obstacle Avoidance for Mobile Robots," *IEEE Transactions on Robotics and Automation*, **7** (3): pp.278-288, June, 1991.
- [41] R. Volpe, and R. Khosla, "Manipulator Control with Superquadric Artificial Potential Functions: Theory and Experiments," *IEEE Transactions on Systems, Man, and Cybernetics*, **20** (6): pp.1423-1436, 1990.
- [42] S. Strenn, T. C. Hsia, and K. Wilhelmsen, "A Collision Avoidance Algorithm for Telerobotics Applications," *Proceedings of the IEEE International Conference on Robotics and Automation*, pp.359-365, May 8-13, 1994.
- [43] M. I. Osak, *Motion Control Made Simple*, Electromate Industrial Sales Limited, May, 1996.
- [44] Advanced Motion Controls, Camarillo, CA. <http://www.a-m-c.com>, July 15,2001.